Alma Mater Studiorum – Università di Bologna
Universidad de Castilla-La Mancha

DOTTORATO DI RICERCA IN

FISICA

Ciclo XXIV

Settore Concorsuale di afferenza: 02/B3

DYNAMIC STABILIZATION OF RAYLEIGH-TAYLOR INSTABILITY OF ABLATION FRONTS IN INERTIAL CONFINEMENT FUSION

Tesi in cotutela tra l'Università di Bologna e la Universidad de Castilla-La Mancha

Presentata da: Laura Di Lucchio

Coordinatore dottorato

Chiar.mo. Prof. F.Ortolani

Relatori

Chiar.mo Prof. G.Turchetti

Chiar.mo Prof. A.R.Piriz

Esame finale anno 2012

Abstract

In this thesis it is studied in detail the possibility to use the mechanism of dynamic stabilization for mitigating the deleterious effects of the Rayleigh-Taylor instability which arises in ablation fronts in inertial confinement fusion. This approach has been originally proposed by Boris in 1977 and later considered by Betti in 1993.

From an historical point of view, such a method has been proposed probably for the first time to stabilize the inverted pendulum, and has also been appplied to the control of Rayleigh-Taylor instability in Newtonian fluids. In practically all those studies dynamic stabilization was obtained by applying a sinusoidal modulation to the background gravity leading to the instability of the system, probably on the basis of believing that sinusoidal modulation was the simplest waveform that could be both produced and analyzed. However, from a mathematical point of view this approach leads to a Mathieu equation which is very difficult to analyze, and makes very difficult to find the regions of stability. In this thesis, it is shown that there is no reason for choosing such a driving modulation, but instead the simplest possible waveforms, that is Dirac deltas and square waves, can be used for dynamic stabilization without loosing sight of the physical picture of the whole system.

In addition to that, in this thesis two situations will be considered, namely an ablation front driven by ion beams and by thermal conduction. It is demonstrated that even for an ion beam driven ablation front some fraction of the energy must be transported by thermal conduction, to make the dynamic stabilization of the front possible. Besides, it is shown that some damping effect introduced by the ablation process itself is also essential. The use of simple modulation waveforms allows to find complete analytical solutions to the equations, and to do a comparison between them

in order to find optimization of the process. Consequently, the important similarity parameters that govern the problem can be found and this sets the basis for the design of an experiment. For this purpose, integrated 2D simulations should be performed starting from the values of the parameters suggested by the theoretical analysis. In any case, the order of magnitude of the latters already demonstrates that dynamic stabilization is well within the present experimental capabilities.In particular, this work could help in the present ignition campaign that is taking place at the National ignition facility (NIF) at Livermore (USA).

To my parents

Contents

List of Figures

LIST OF FIGURES

1

Introduction

1.1 Review on controlled thermonuclear fusion

In 1929 Atkinson and Houtemans discovered the possibility of obtaining energy starting from nuclear fusion reactions,with much more gain than in the case of nuclear fission. Nuclear fusion is a process in which two very light nuclei combine forming a nucleus with a higher binding energy (or lower mass), thus releasing energy according to Einstein's formula. In 1939 Hans Bethe was the first to propose that nuclear fusion could be the way the sun produces its energy, and soon it became clear he was right. Approximately in the 1950s civil reasearch about the possibility of reproducing nuclear fusion started; nowadays many countries support studies in this field, hoping that we can find a new resource for the production of electricity. If it were possible to develop a controlled way of achieving fusion, we could have a very efficient and practically infinite source of energy. In fact, the energy gain of fusion reactions is 4-8 times larger than in fission ones, and the fuels (light elements like deuterium) are so abundant in nature as to provide energy for the conceivable future. In addition to that, such processes do not produce radioactive waste, although in the case of a reactor neutron production should be taken into account as a likely problem.

In spite of the considerable effort that has been made so far to dominate the nuclear fusion mechanism, the goal has not yet been reached due to the difficulties that have arisen each time it seemed quite near. In principle many energy-releasing fusion processes between different low mass elements are possible. However, the problem in igniting such a fusion reaction is that the light nuclei are positively charged and strongly repel each

other, so that under normal conditions the distance between them is so large that a nuclear reaction is quite unlikely: most of the collisions simply produce a change in the particles' trajectories (diffusion)[1]. In the center of the sun, the high temperature ($\approx 10^6 K$) and pressure, together with the large number of particles and the relatively long time span available, make the cross section for such reactions large enough to maintain the large energy releases characteristic of the sun. Here on Earth there is not enough space or time in comparison to the sun, nor its great mass which in turn creates the necessary gravitational attraction and it would be impossible to produce energy on a large scale. In a laboratory the only way to overcome the problem of coulombic repulsion that hinders the nuclei from fusing is to give the nuclei themselves a very high initial kinetic energy. This can only be achieved by heating the materials to very high temperatures , so that we deal with a thermalized gas whose particles follow a random distribution in velocity, namely the Maxwell-Boltzmann distribution; indeed, it has been statistically proven that most of the observed thermonuclear reactions will be due to a relatively small fraction of the nuclear collisions in which the relative energies are greatly in excess of the average (for a more detailed treatment, see (1)). This mechanism of achieving fusion reactions is called *thermonuclear fusion*. When it is done in an uncontrolled way, it gives birth to the hydrogen bomb, and the proof of its feasibility was obtained in 1952; in this case the detonator is X radiation generated by a nuclear fission bomb explosion. Experiments to determine the energy required to ignite fusion fuel in such a way were done between 1978 and 1988 in the series of Halite-Centurion studies in the USA, and the few data publicly available suggest that an implosion energy of 20 MJ would be needed. These results gave an idea of what should be the energy of the driving mechanism, but left scientists with the problem of how to achieve fusion in a controlled fashion with a fusion reactor.

Because of the high temperatures and densities required for fusion, the fuel has to be in the plasma state. As we said before, the temperatures and consequently the thermal velocities of the nuclei have to be sufficiently high so that they have a chance to

[1]It can be demonstrated that if we simply accelerate a nucleon beam towards a target there is no gain of energy, since the particles have all the same kinetic energy and move in the same direction, so that it is very unlikely that at least some can overcome the Coulombic repulsive barrier. Only when energy is adquired as a result of a growth in temperature particles exhibit a random motion, so that at least a little fraction of the particle population will have a high kinetic energy.

approach each other close enough to overcome Coulombic repulsion and be subjected to the short-range attractive nuclear forces. At this point the nuclei can fuse and free the enormous power incapsulated inside them. However, under these conditions matter tends to fly apart very quickly unless constrained in some way, and the higher the temperature and density, the more difficult it becomes to confine the plasma for a sufficient amount of time. Therefore, we first have to look for a situation in which the requirement for confinement is as low as possible, and consequently for the fusion reaction which is most readily achieved under these conditions.

Even if the energy of the particles is slightly less than that required to overcome the Coulomb barrier, the fusion process can still occur via tunnelling, but at the same time the probability of tunnelling increases as much as the particle energy gets closer to overcoming the barrier. In general, in order to have a sufficient number of fusion reactions, the thermal energy of the nuclei should not be too much smaller than their repulsive Coulomb barrier B, which is given by

$$B \approx 1.44 \frac{q_1 q_2}{r_1 + r_2} MeV \tag{1.1}$$

Here $q_{1,2}$ and $r_{1,2}$ are the charges and radii of the particles in units of the elementary charge and in fm, respectively. To have an idea of the temperatures needed to overcome the "height" of the barrier, let's consider the simple case of two hydrogen nuclei. In this situation, the barrier is about 700 KeV, which means that we should heat the gas (fuel) until it reaches a temperature equal to $2B/3k_B \simeq 3.6 \times 10^9 K$; this is not a realistic prospect at the moment. Therefore, we have to choose light elements that have a smaller Coulomb barrier: this is the case of the heavier hydrogen isotopes, deuterium and tritium. After a calculation of the cross section and the mass defect of all the possible reactions between these elements, it turns out that the best reaction is deuterium-tritium fusion because its cross section is two orders of magnitude larger than the one of the next largest reaction in the relevant temperature range (typically 20-40 keV, as shown in fig.(1.1)). The intermediate product of this reaction is a nucleus consisting of two protons and three neutrons, which splits immediately into a neutron of 14.1 MeV energy and an α-particle of 3.5 MeV: ${}^2_1\mathrm{D} + {}^3_1\mathrm{T} \longrightarrow {}^4_2\mathrm{He} + {}^1_0\mathrm{n} + 17.6$ Mev.

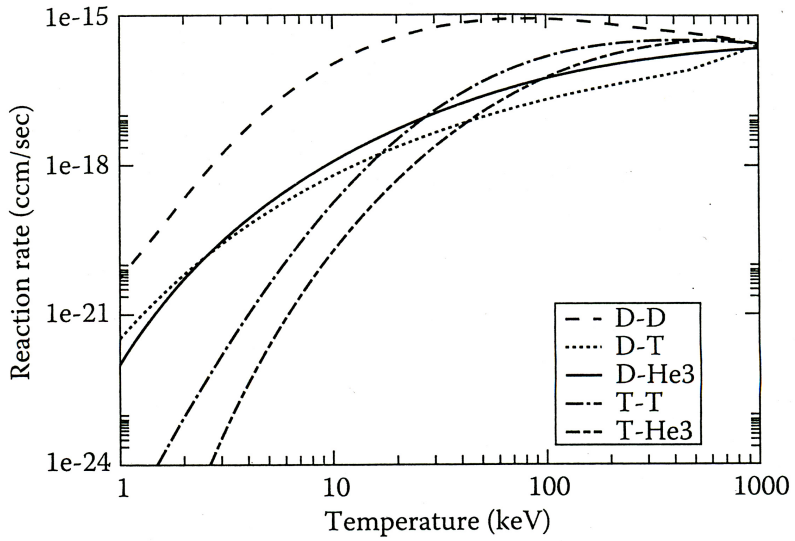

Figure 1.1: Nuclear reaction rates - Nuclear reaction rate as a function of temperature for the most common fusion reactions. DT is by far the easiest fuel to ignite (source: Pfalzner, 2006 (2)).

In addition to energetic considerations, this fusion reaction has more advantages in the abundance and availability of the fuel components. Deuterium can be produced from sea water, whereas tritium can be generated by lithium reactions with neutrons directly in the reactor. However, there is still one problem. Lithium resources are likely to be sufficient for several 10^4 years , but making it react to produce tritium has two disadvantages: tritium is a radioactive gas and litium a highly poisonous substance, so that this task includes safety as an essential goal. Nevertheless it has to be stressed that such problems are not huge if compared with the ones we have to deal with in fission reactors: the half life of tritium is 12.5 years, much shorter than the 2.4×10^7 years of uranium 236, or 7.13×10^{18} of uranium 235, and still negligible if compared to the 24000 and 6600 years of plutonium 238 and 240, respectively. In the end, deuterium-tritium fusion is still the more advantageous one for producing energy.

1.2 Lawson criterion

Once we have chosen the type of reaction we have to achieve a good way of confining the fuel and obtaining a huge number of fusion reactions per second. First of all, we need a criterion that allows us to decide if a particular nuclear fusion process is able to produce a net amount of energy. The Lawson criterion defines the condition needed to reach a situation in which the heating of the plasma by the products of the fusion reactions is sufficient to maintain the temperature of the plasma against all losses without external power input. Here we will assume, in an optimistic view, that the energy losses due to Bremsstrahlung (that is, electromagnetic radiation emitted by the deceleration of the plasma charged particles) are negligible, and we will consider only the fusion energy and the thermal energy of the plasma. Besides, we will derive the formula for the case of a deuterium-tritium (DT) fuel, but the results can be easily generalized to any other fusion fuel.

Assuming that the plasma consists of deuterons and tritons of density $\frac{n}{2}$ each (equimolar mixture), the *volume rate* W (numbers of reactions per volume per time) is given by

$$W = \frac{n^2}{4}\langle v\sigma\rangle, \tag{1.2}$$

where v is the relative velocity of the two nuclei, σ is the fusion cross-section and $\langle\rangle$ denotes an average over the Maxwellian velocity distribution of the particles in the plasma.The energy produced per time τ depends on the kinetic energy Q of the reaction products and the rate of fusion processes W in the following way:

$$E = W\tau Q = \frac{n^2}{4}\langle v\sigma\rangle\tau Q. \tag{1.3}$$

Now we need to impose that the energy obtained from the fusion processes has to be greater than the energy to heat the plasma to such high temperatures; only this way energy will be gained from an ignited DT-plasma. As the kinetic energy of the nuclei and electrons is $E_{kin} = 3nk_BT$, it follows that only if

$$3nk_bT < \frac{n^2}{4}\langle v\sigma\rangle\tau Q \tag{1.4}$$

the fusion reactions actually release more energy than is required to produce the plasma of such temperature and density. We can re-express the condition (1.4) as

$$n\tau > \frac{12k_BT}{\langle v\sigma\rangle Q}, \tag{1.5}$$

that is a relation for the product of the number of particles per cm^{-3} and τ the confinement time. The relation (1.5) is called *Lawson criterion*, and is one of the fundamental relations of confinement fusion.
To fix a value for the kinetic energy k_bT we have to take into account that it must be high enough to assure a sufficient number of fusion reactions. For DT fuel this value is approximately 5keV , but the operative temperature of the reactor can be set to 5-10 keV. Knowing that Q=17.6MeV , the Lawson criterion for DT fusion becomes

$$n\tau \backsimeq 10^{14} - 10^{15}\mathrm{s\ cm}^{-3}. \tag{1.6}$$

Now that we have the fundamental condition for confinement fusion, we have to find a confinement mechanism that can satisfy it. We have already seen that the physical situation we have in stars cannot be reproduced in a laboratory, so we have to look for other solutions. Actually two ways of doing confinement have been found and developed: *magnetic confinement* and *inertial confinement* .

1.3 Magnetic vs inertial fusion

1.3.1 Magnetic confinement fusion approach

In *magnetic confinement fusion* (FCM), the plasma is being confined by using very intense magnetic fields, due to their properties of deviating the trajectories of charged particles. The basic idea is that exists a suitable magnetic configuration which can force the nuclei and electrons in the plasma to stay on closed orbits and never escape. This mechanism is object of investigation since the 1950s, when I. Tamm and A. Sakharov invented the TOKAMAK (Russian acronym for toroidal magnetic chamber). The Tokamak is a device containing vacuum into which a mixture of deuterium and tritium is injected; the magnetic field is produced by passing an electric current through coils wound around a torus (see fig.(1.2)). Experimental research on Tokamaks was conducted for the first time by a scientific group led by L. Artsimovich in Moscow since 1956, and in 1968 it was announced by Russians that the first ever quasistationary thermonuclear reaction had been achieved. The tokamak has since gone on to become the most studied approach to controlled fusion until recent times. However, in spite

of the improvements obtained during the following years in terms of plasma temperature, confining time and amount of produced energy, no one was able to construct a full theory of a plasma which undergoes very strong magnetic fields, so that every new device was undermined by new and unknown problems, most of which are still unresolved. Mainly, the problems come from the fact that MCF tries to confine the plasma at low densities ($\sim 10^{14}$ to 10^{15}cm^{-3}) for several seconds, during which a lot of disturbing effects are observed to appear. For example, the same collisions between plasma particles which are necessary for fusion process have the tendency to destroy confinement in the long run, because when two particles hit they are temporarily disconnected from their magnetic field line and so they can move towards the walls of the reactor. Besides, a plasma instability can occur if an initially small perturbation in the configuration induces a further disturbance, which in turn increases the perturbation and so on. In MCF a large variety of these instabilities occur, thus reducing the quality of the confinement. Due to all these difficulties, in recent years a lack of confidence in this way of achieving confinement started to spread among the scientific community. The last and most ambitious international experimental project relating to this field, ITER (International Thermonuclear Experimental Reactor), is still under preparation although first designed in 1986, and reasonably the proof of an engineering feasibility of an MCF reactor is not in sight yet.

1.3.2 Inertial confinement fusion approach: central direct ignition concept

Later than MCF has been developed a new kind of investigation in thermonuclear fusion, the so called *inertial confinement fusion*. The aim is to confine the plasma using inertia as the mechanism that avoids plasma dispersion; in this scheme, a small amount of fusionable material is compressed to very high densities and temperatures by ablating the outer shell using very strong mechanisms of energy deposition (laser, particle beams, x-ray radiation). As a natural reaction to the vaporization of the outer material, the inner fuel implodes and heats. Therefore, the plasma reaches very high densities (typically greater than $10^{25}\,\text{cm}^{-3}$), while the confinement times are extremely short, typically of the same order of magnitude of the time it takes to a sound wave to travel through the capsule ($\leq 10^{-10}$ s). This is an alternative way to fulfill the Lawson's

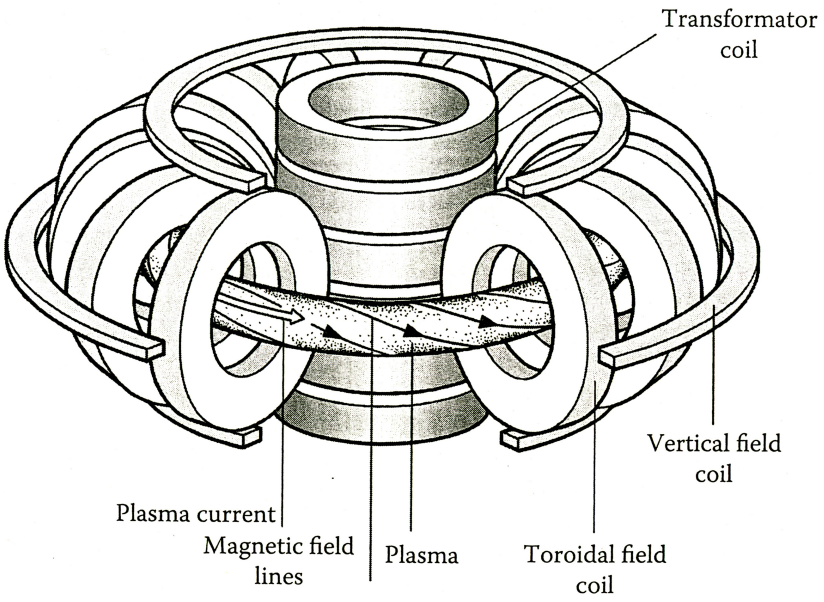

Figure 1.2: Scheme of a tokamak - Schematic picture of magnetic configuration in a tokamak (source: Pfalzner, 2006 (2)).

criterion with respect to MCF, and is expected to yield very good results even if the physical phenomena behind it are still under study.

In the early days of fusion research, it was thought that the whole of the fuel should be compressed to thermonuclear fusion conditions: this process was called *volume ignition*. It was discovered quite soon that this would require an unrealistically high driver energy, due to the unefficiency of the system: in numbers, with the usual parameters for the target, we are speaking of an input energy of ≈ 60 MJ .

At the present time, the proposed way of achieving inertial confinement fusion is the *hot-spot* scheme. In this approach the energy is deposited by the driver on the shell in such a way that ignition is produced in the center of the capsule. In this way only a fraction of the fuel is ignited and the central region is compressed, thus becoming considerably hotter and less dense than the outer part. This central area which is compressed and heated is the so-called hot-spot; thermonuclear burn starts here, when the initial conditions of temperature and density are finally achieved, and then the burn front propagates rapidly outward into the main fuel region, producing a fusion energy that is significantly greater that the total energy put into the driver beams. The hot spot scheme is much more efficient that volume ignition, because it requires heating less

material, and the heating is what costs more in terms of energy demanding. Furthermore, compression is more energy-consuming for hot material than for cold material, so there is a further advantage in reducing the quantity of hot material to the central region. In addition to that, external dense fuel layer provides better confinement. However, there is an important issue to deal with, namely that any premature heating of the material has to be avoided as long as possible, because this would completely jeopardize the compression.
In the following, we will briefly summarize the procedure of hot-spot ignition: unless we specificy otherwise, the following considerations will be valid independently of the mechanism of energy deposition on the shell.

In the initial phase (*interaction phase*) the energy is delivered by laser or particle beams onto the capsule containing the DT fuel, which consists of a spherical shell filled with deuterium-tritium gas at low density (≤ 1.0 mg/cm^{-3}). The shell itself consists of a high-Z material at the outside and an inner region for DT, which forms the bulk of the fuel. To reach the conditions of high temperature and density required for fusion, the capsule needs to be exposed to an enormous burst of energy applied as symmetrically as possible. For example, to heat a 5-mm diameter capsule of fuel to 10keV temperatures requires an energy input of $E_d = 2MJ$, which has to be delivered in ten nanoseconds to the outer part of the target shell. Because of such a burst of energy in a small time, the shell heats up, ionizes and vaporizes immediately; this process is called *ablation*.
The interaction phase differs significantly depending on the energy driver mechanism. First of all, both direct and indirect drive can be used to deposit the energy; in this section we will mainly focus on the direct drive, namely direct illumination of the target by means of laser or ion beams. Here we will describe the scheme known as *central ignition*, in which the compression of the fuel and the heating of the hot-spot are generated by the same pulse hitting the fuel target. Lately, we will examine other possible approaches that have been proposed in the last years for the hot-spot ignition.

In the case of a direct drive with lasers, a plasma is created immediately as soon as the laser beam comes into contact with the outer surface of the capsule and expands outward from this surface. This plasma cloud is called *corona*; it has high temperature

and low density, and its thermal pressure, together with the reaction of the inner material, causes the implosion. In principle the laser beam should penetrate through this plasma to reach the capsule, but in practice it only penetrates until a point in which the *critical density* is reached, that is where the plasma frequency is equal to the laser frequency : $\omega_p = 2\pi\nu$. Consequently, the laser energy is not directly deposited onto the capsule surface. The critical density is the density at which the plasma becomes opaque to the laser light (just like it happens for any kind of radiation passing through a material), and it exhibits a strong dependence on the wavelength, intensity, and pulse length of the laser beam. The choice of these parameters is thus essential for an efficient coupling of the laser energy to the target. These parameters determine not only the gap between the critical surface and the target surface, but also the amount of ablation and the efficiency of the subsequent compression phase.
In the case of a direct drive with ion beams, the ions penetrate into the corona until a distance which is defined by Bragg peak, with relatively little loss in energy, if compared with the case of electromagnetic radiation. Also, their focusing onto the target can be done by magnets.

As the outer part of the shell blasts off, the inner part -essentially the fuel- is strongly accelerated towards the centre of the sphere as a consequence of momentum conservation, thus being compressed to high densities (several hundreds of g cm^{-3}) and thermonuclear temperatures. The *ablation surface*, namely the interface between the inner, cooler and denser plasma and the outer ablated material is at first located at the deeper point of penetration of the driver, and then moves rapidly inwards. As the outer shell is accelerated by the ablation pressure until half the initial radius of the capsule (current target designs use a capsule radius of about 500 μm), the implosion time can be estimated as the ratio of this distance and the implosion velocity, tipically around $3 - 4 \times 10^7$ cm /s for laser intensities of $\sim$ 1MJ and it results to be $\sim$ 1 ns . Finally, ignition occurs at the centre of the capsule and the consequent fusion energy produces an outward shock wave and soon the pressure overcomes that of the imploding wave, so the capsule blows back out in a very short time (for a schematic representation of the process in the case of a laser driver, see fig.1.3). On the other hand, the confinement time of the plasma is mainly determined by the radius $R_{(HS)}$ of the hot-spot, namely by the ratio of $R_{(HS)}$ over the speed of the rarefaction waves that disassemble the fuel.

Since the rarefaction waves travel with a velocity $c_{s(HS)}$ approximately equal to the one of sound in the material at a temperature of $10 - 15$ KeV, if the radius of the hot spot is realistically estimated as $50 - 100\mu m$ (corresponding to about 2% of the total mass of the fuel), the confinement time is given by $t_c \backsimeq R_{(HS)}/c_{s(HS)} \approx 10$ ps (3) (4).

When the inner part of the fuel reaches the center of the capsule the third step of fusion begins: it is the *deceleration* or *stagnation* phase, which is so called because now the kinetic energy of the inner part is converted into internal energy. This way we achieve the desired temperature and density increase in the center of the capsule, where ignition is reached leaving the rest of the fuel relatively undisturbed. In the hot spot concept, the fuel must reach the center with an in-flight velocity of at least 2×10^7 cm/s, which means generating a pressure of ~ 100 Mbar.

After the deceleration phase, we have finally the ignition and burn phase, as soon as temperature and density in the center of the capsule are high enough (typically, we should have ~ 30 times the density of lead and a temperature of $\sim 10^8$ K). As we have already said, ignition produces α-particles which deposite their energy primarily in the central area and heat it up vey quickly. Then the energy is trasported by radiation, fusion neutrons and thermal conduction (driven by electrons) from the hotspot region to the outer fuel area. As the temperature of this outer region increases, other fusion reactions take place also there and the burn propagates further outward. The time scale of the whole process is approximately 10 ps, enough to let a very high pressure to build up and eventually blow apart the remaining fuel and thermalized α-particles. These α-particles have to be taken into account for safety problems, as they can interact with the walls of the reactor. Then the ICF cycle ends ; the next target is injected in the reactor and the ICF process starts again.

1.3.3 Estimate of the efficiency of ICF using the Lawson criterion

In the context of ICF, we can re-express the Lawson criterion using first the estimate for a freely expanding sphere with the same density ρ and radius R as the final radius of the capsule itself. We already know from the previous paragraph that the confinement time can be roughly estimated by $\tau \backsimeq R_{(HS)}/c_{s(HS)}$, being $R_{(HS)}$ and $c_{s(HS)}$ the

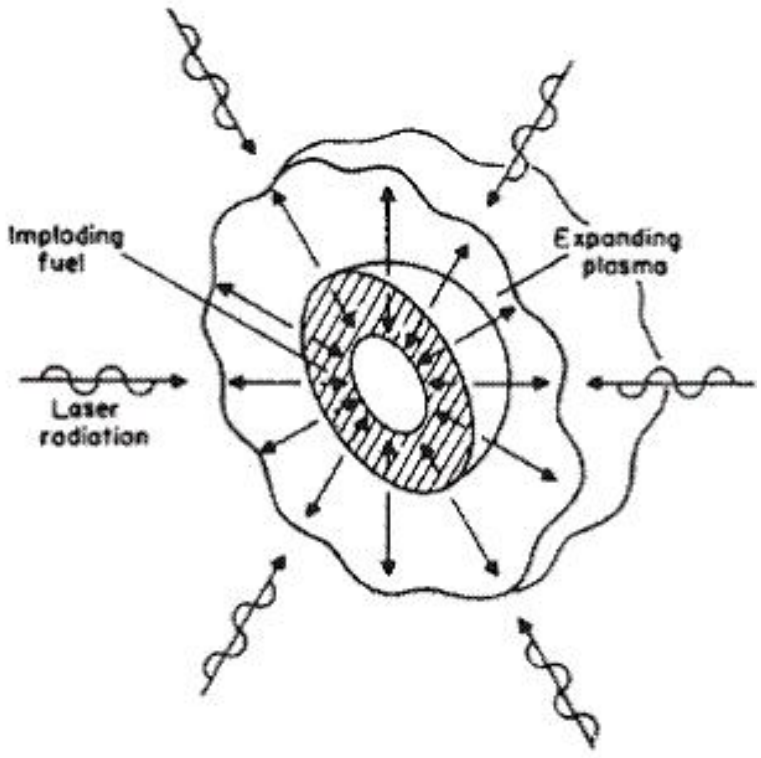

Figure 1.3: Laser driven implosion - The concept of a laser driven implosion (source: Nakai and Mima, 2004 (5)).

hot spot radius and the velocity of the rarefaction waves which disassemble the fuel, respectively. Introducing the number density n, which is related to the fuel density by $n = \rho/m$, we can substite (1.5) with the approximation

$$n\tau \backsimeq \frac{nR}{c_s} = \frac{\rho R}{c_s m}. \tag{1.7}$$

A realistic estimate is $n\tau \backsimeq 2\times 10^{15}$ s cm^{-3}, which leads to a first approximate condition $\rho R \backsimeq 3g/cm^2$.

We also have to take into account that the energy gain in ICF fusion depends on the amount of fuel which is burned in the process. Whatever is the target configuration, it will always be impossible to burn all the fuel in the capsule, but we can estimate the fuel conditions that must be achieved for efficient burn and a high yield relative to the driver energy. The number of thermonuclear reactions n per second is given by

$$\frac{dn}{dt} = n_D n_T \langle \sigma v \rangle, \tag{1.8}$$

where n_D e n_T are the reactant number densities, namely, for an equimolar DT-mixture

$$n_D = n_T = \frac{n_0}{2} - n, \tag{1.9}$$

where n_0 is the initial total number density. The *fractional burn* is the ratio of the number density of the reaction products to the initial number densities of the deuterium (or tritium), that is $f_b = n/n_D T = n/(n_0/2) = 2n/n_0$. Consequently, the number density can be expressed as $n = n_0 f_b/2$ and the (1.8) becomes

$$\frac{n_0}{2}\frac{d\, f_b}{dt} = \left(\frac{n_0}{2} - \frac{n_0 f_b}{2}\right)^2 \langle \sigma v \rangle, \tag{1.10}$$

or

$$\frac{df_b}{dt} = \frac{n_0}{2}(1 - f_b)^2 \langle \sigma v \rangle. \tag{1.11}$$

Assuming that $\langle \sigma v \rangle$ is constant during burning time τ_b, it follows that

$$\frac{f_b}{1 - f_b} = \frac{n_0 \tau_b}{2} \langle \sigma v \rangle. \tag{1.12}$$

This can be rewritten as

$$f_b = \frac{n_0 \tau_b \langle \sigma v \rangle / 2}{1 + n_0 \tau_b \langle \sigma v \rangle / 2}. \tag{1.13}$$

Knowing that the burn time and the sound speed are approximately related by $\tau_B = r/3c_s$, it follows that

$$f_b = \frac{n_0 r\langle\sigma v\rangle/(6c_s)}{1 + (n_0 r\langle\sigma v\rangle)/(6c_s)}. \tag{1.14}$$

Using the mass density , which is related to the number density by $n_0 = 6.02 \times 10^{23} \frac{Z}{A}\rho$, we finally have

$$f_b = \frac{\rho R}{\rho R + \psi(T_i)}, \tag{1.15}$$

where $\psi(T_i) \approx c_s/\langle\sigma v\rangle$. The reaction rate depends strongly on the temperature, and approximate formulas have been found for it, but here we directly consider the case of the equimolar DT mixture at 20-40 keV, which gives us the following expression for the (1.15):

$$f_b = \frac{\rho R}{\rho R + 6(g/cm^2)}. \tag{1.16}$$

The (1.16) is in very good agreement with more detailed numerical simulations of the burn process of most ICF targets. For example,we need $\rho R = 3\text{g/cm}^2$ for a 33% burnup. According to this criterion, igniting 1 mg of DT requires a radius of 90 μm and an average density for the material of 330 g/cm^3, which is about 1300 times the density of cryogenic DT. The corresponding pressure for DT, at a temperature of the order of 10 keV more, is of hundreds of Gbar. This means that we need laser or ion beam pulses with a duration of a few nanosecond, which are able to generate pressures of hundreds of Mbar on the ablation surface. To reach such high densities in the compressed fuel requires keeping the entropy low enough so to minimize the amount of work required for compression. This can be achieved by modulating the shape of the laser or ion beam pulses so to generate a sequence of waves capable of accelerating the fuel towards the center if the capsule causing the minimum possible rise of the entropy (nearly isentropic compression).

The ablated material acts like a piston pressing onto the inner fuel, which is denser and therefore tends to expand, thus generating a rarefaction wave traveling outward. This results in an increase of the pressure and in the formation of a positive density gradient in the fuel. The same mechanism occurs twice for each beam, as both the pre-pulse and the pulse generate rarefaction waves. As the second pulse starts to penetrate the target, it finds the rarefaction wave generated by the previous pulse which travels in the opposite sense. The final result is that the entropy assumes a well-defined spatial distribution, decreasing with the radius. Such an entropy profile is maintained during

the entire stagnation phase, provided that we always use the same pulse scheme in the succession of the beams. The deceleration phase takes place in a suitable manner provided that the last of the shocks acts at the same time as the first shock on the compressed fuel in the center. Consequently, the challenge is to achieve a good timing for the sequence of shocks.

1.4 The indirect drive scheme

If we simply deal with the previous treatment, it may seem that it is not such a difficult task to achieve a good energy gain whith ICF, because the energy requirements for heating the fuel do not seem too demanding. This was the first impression scientists had in the early 1960s and 1970s, starting from the same considerations above. Actually the situation is not the one we have just depicted: after the initial enthusiasm, further investigation showed that in practice not all the energy contained in the driver can be used for ignition, because there are a lot of energy losses during the energy conversion processes from the laser to the final burn of the fusion material. In addition to that, in central ignition, both the ablated shell and the hot central region are subjected to hydrodynamic instabilities, mainly Rayleigh-Taylor instability.
Most of the undesired effects in compression phase are determined by microscopic or macroscopic illumination nonuniformity in the interaction phase. Macroscopic nonuniformities can be caused by an insufficient number of beams or the existence of a power imbalance between the individual beams, while microscopic nonuniformities can derive from the presence of spatial fluctuations within a single beam itself. For each case, there are a number of possibilities, but further analysis is beyond the purposes of this work. Here, the important fact we have to take into account is that both microscopic and macroscopic nonuniformities can lead to instabilities in the compression phase. In the case of macroscopic instabilities, one solution can be to take a sufficient number of beams and to improve their syncronization. An alternative approach that has been proposed is the *x-ray* or *indirect drive* scheme, which is mainly motivated by military applications and for the possibility to simulate inertial fusion indirectly driven by ion beams, if acceleratos are considered as feasible drivers.
The dynamics of indirect drive can be summarized as follows. Laser beams deposit

their energy on the internal surface of a radiation cavity called *hohlraum*, typically a hollow cylinder 1-2 cm long, with a diameter of 6 o 7 mm respectively The walls of the cavity are made of high-Z material, typically gold, and are 20-40 μm thick, and they have holes at the extremities to let the laser beams enter. The inside of the cavity is filled with a low density inert gas to avoid expansion of the walls and fluidodinamic motions. The capsule is installed in the center of the *hohlraum*. When lasers hit the cavity's wall, the latters emit isotropic thermal radiation costituted by soft X-ray radiation, which in turn is absorbed and re-emitted 8-10 times before depositing its energy on the capsule. Typically, the efficiency of the laser energy conversion is about 70-80%. A numerical estimate for the driver energy which takes into account the mechanisms of energy loss and gives a comparison with the energy E_d required in direct drive is $E_ind = \eta_h\eta_L E_d,\ \eta_h, \eta_L \approx 0.1$, where η_h and η_L are the hydrodynamic efficiency and the laser efficiency. The cavity is gradually filled by a nearly isotropic radiation field which is responsible for the ablation of the outer shell of the capsule.

Indirect drive is less sensitive to hydrodynamic instabilities (but not completely free of them), since it produces relatively high ablation velocities, and the requirements for laser uniformity and simmetry are lower. However, this scheme needs a higher energy input if compared with direct drive, due to the fact that the efficiency in converting the energy of the lasers into X-ray radiation is not of 100%. Again, we have to deal with technological problems, this time related to the use of laser driving, which make the current rates of repetition of the igniting process (now in units of days) still far from the frequency for the fusion required for producing energy for practical use (about ten per seconds). Hence, the possibility of using ion beam drivers instead of lasers could be examined. Anyway, one advantage with indirect drive is that we can study the generation of thermal radiation and the capsule implosion separately, as the latter is independent of the features of the cavity and of the laser beams. As both methods present advantages and disadvantages, it is not clear yet which one could be the most suitable for producing inertial fusion energy. The indirect-drive scheme is very much favoured by United States and France, where laser systems for ICF , NIF and Laser megajoule respectively, play a major role in military application programs (NIF has already been built, whereas LMJ is under construction),but other countries are more interested in civil uses and would prefer developing direct-drive approach.

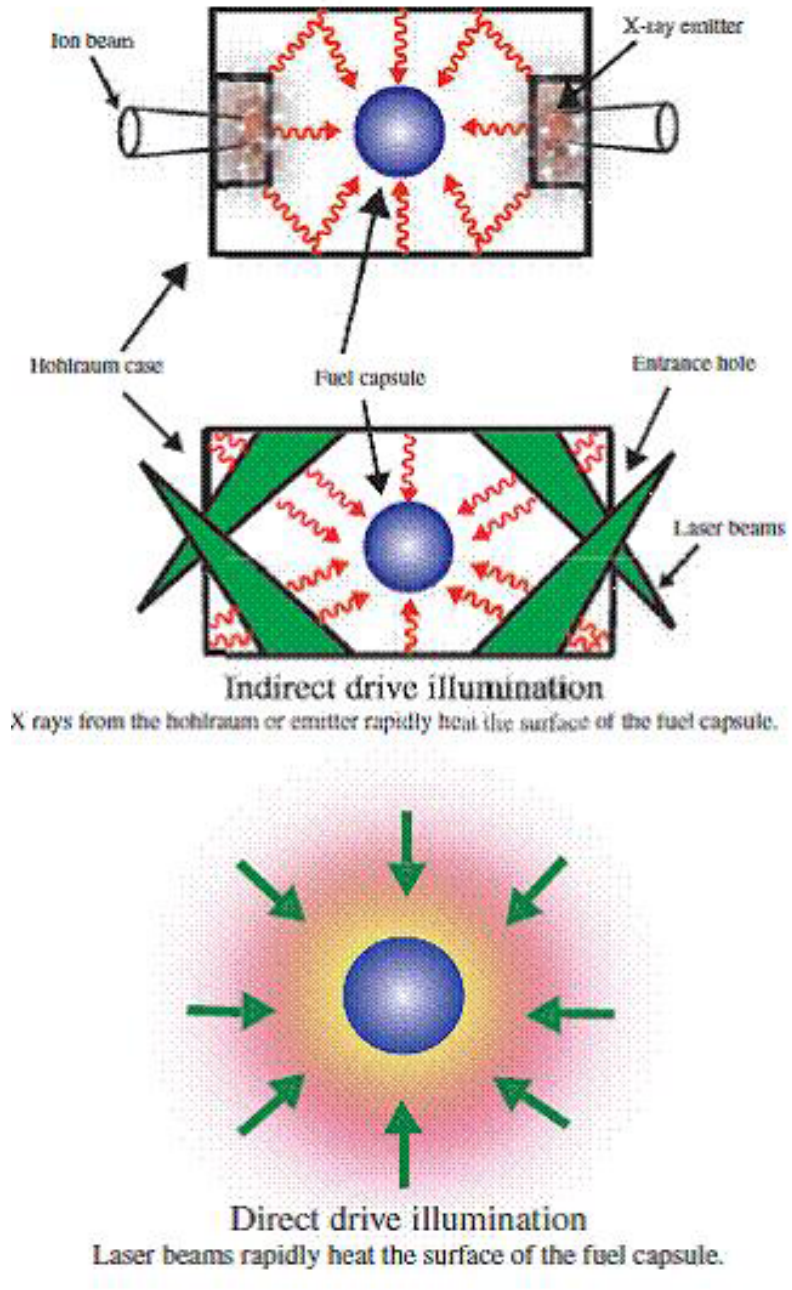

Figure 1.4: Direct versus indirect drive - Basic implosion schemes *direct drive* and *indirect drive*(source: Nakai and Mima, 2004 (5)).

1.5 Fast ignition approach

In the last years other methods for ignition of the target have been proposed, in order to look for solutions resulting less sensitive to the effects of RTI showed both by direct and indirect drive approaches. The most important is the *fast ignition* scheme, first proposed in 1994 by Tabak, Munro, and Lindl. They suggested an approach known as *hole boring* consisting of three phases (fig. 1.5):

1. the capsule is imploded by a conventional laser to produce a high-density core;
2. a hole is drilled through the coronal plasma using a high-intensity 100 ps pulse, whose focal position is near the critical surface so that it penetrates the overdense region;
3. the core is ignited using a third laser pulse with high $I\lambda^2$ (product of intensity times the square of the wavelength).

The advantage of such a concept is that it allows separating the two phases of compression and ignition, thus achieving a higher gain for a lower driver energy input; theoretical investigations suggest that a $Q \sim 200$ could be reached, much greater than the corresponding values for indirect-drive scheme ($Q \sim 30$) and for direct-drive ($Q \sim 100$). Because of such advantages in gain, in fast ignition the driver efficiency (if it works well) could be 5%, less than in the other approaches. Therefore, the tolerances in target fabrication can be higher.

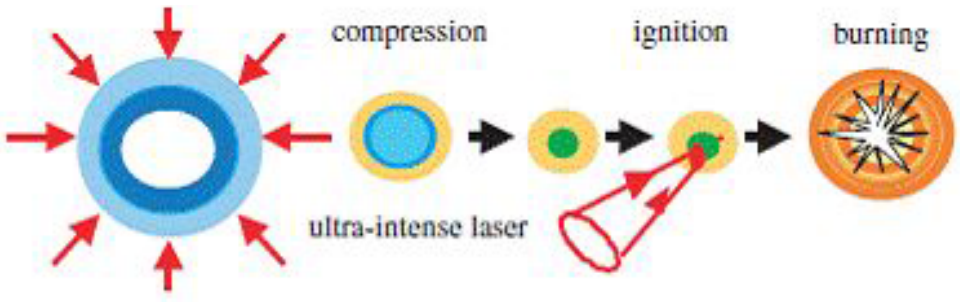

Figure 1.5: - Fast ignition concept: at the maximum compression of laser implosion, the ultra-intense short-pulse laser is injected to heat the dense core plasma (source: Nakai and Mima, 2004 (5)).

Apart from these considerations, it is worth to make a direct comparison between the fast-ignitor and the central-ignitor concept. In the last one an isobaric configuration (first studied by Meyer-ter-Vehn, 1982 (6)) is maintained during the compression: the central hot spot can equilibrate its pressure with the one of the high-density region in contact with it, because during the stagnation process the sound speed in the gas is much greater than the shell closure velocity. In this phase the shell moves to its convergence radius from twice that radius and it turns out that the main fuel is about 1 sound-crossing time thick. On the other side, in the fast-ignitor scheme the whole fuel is compressed by a conventional laser to a very high density and then the core (sometimes called hot spark) is ignited very quickly with a ultra-intense pulse after drilling a hole in the corona, so that pressure equilibrium is not kept at all. Therefore there is no need for a low-density hot central region, and the confinement parameter ρr for the ignited core can be significantly higher than in the central ignition case. Rather than isobaric, this is an isochoric compression, namely at uniform density, as in the model firstly proposed by Kidder in 1976(7) for central ignition (it is worth to notice that this work was later substituted by the one of Meyer-ter-Vehn and finally was drawn up by scientists to study fast ignition) , so that more mass can be compressed to much lower peak density, resulting in a larger amount of burnt fuel. In addition to that, the stagnation pressure in the isochoric model is about two orders of magnitude lower than the one in the isobaric model, and this great reduction in concentration of energy eases the required implosion quality. For a direct comparison between the models used for different ignition schemes, see fig. (1.6).

The main challenge in fast-ignition scheme is how to deliver the energy to the pre-imploded capsule. The laser should penetrate into the extended corona which surrounds the ablated plasma, and then reach the overdense central region without losses of energy. As always happens when we use a laser as a driver, we have to deal with the fact that it only travels until the critical density is reached, and in this case it happens at a distance of several hot-spot diameters from the central core, in a region populated by hot electrons. Coupling of the laser with such electrons would result in a poor efficiency,therefore a way to bring the intense light closer to the compressed core has been studied. In addition to that, the original idea of Tabak et al. (8) of drilling the hole using a 100 ps pulse presents more shortcomings. Experiments have shown

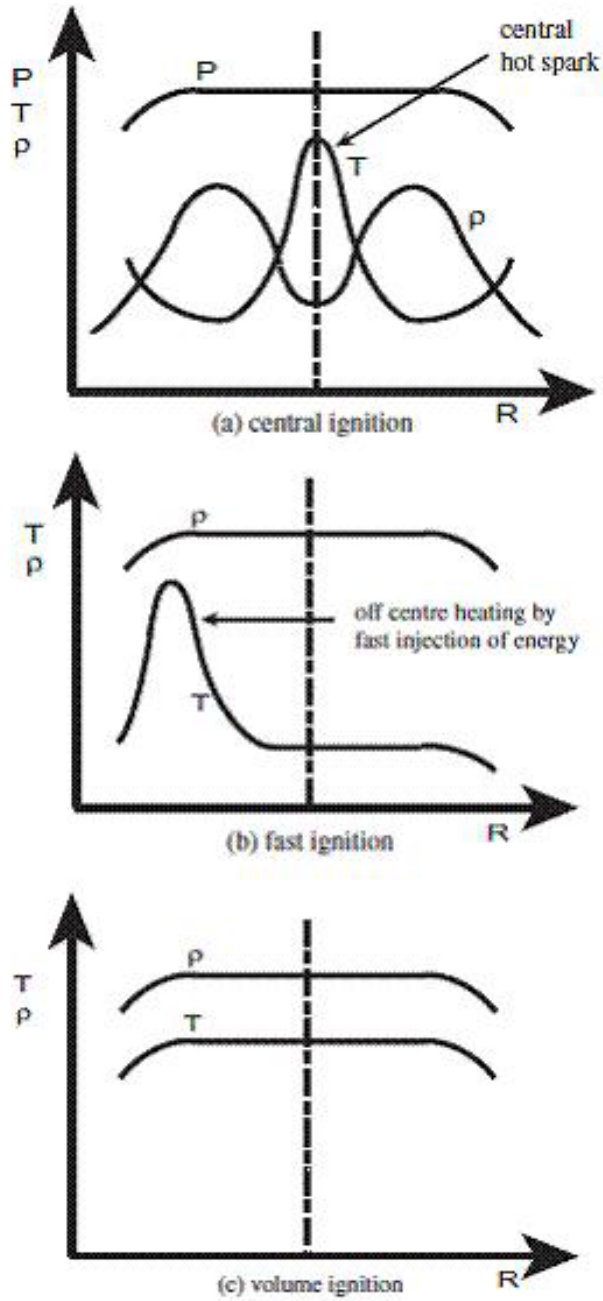

Figure 1.6: Ignition schemes - Ignition schemes of compressed fuel. The central ignition scheme (a) is analysed with an isobaric model, and the fast ignition (b) is analysed with an isochoric model. Uniform distribution of density and tempearture is assumed for volume ignition (c) (source: Nakai and Mima, 2004 (5)).

that the result is an enhanced neutron yield, and that unfortunately this process is dominated by the high-energy ions instead of the thermal ones (the most suitable for fusion); besides, it is not still understood if such a neutron yield comes from fusion reactions near the critical surface or from the core.

Alternative options for solving the problems with hole-boring have been proposed. Deutsch at al. (9) suggested to take advantage from relativistic effects that appear when an ultraintense laser ($10^{19} - 10^{21}$ W/cm^2 for a duration of a few femtoseconds) strikes a plasma and in particular from the ponderomotive force, which depends on pressure radiation and therefore is related to the energy density of the laser pulse. The idea is that the suprathermal electrons generated by laser-plasma interaction could travel from the critic surface in the corona to the core of ultra-dense fuel, where they could deposit their energy so to create the temperature conditions for ignition. However, the energy spreading of the electrons generated by laser-plasma interaction prevents from obtaining an efficient coupling between relativistic electrons and a pre-compressed fuel, as hypothesized in (9). It has also been suggested to use heavy ion beams instead of ultra-intense lasers, but the extreme requirements for pulse duration make this approach not feasible at the present time. Finally, the option of designing a target as a capsule with a guiding cone made of high-Z material (so that its walls remain intact when the plasma develops) has become increasingly popular in recent years. In this scheme, the fuel shell is imploded to produce a compressed core plasma near the tip of the cone and when the required density is reached (typically 1000 times solid density for a reactor-size cone target, with confinement parameter $\rho r > 2$g/cm^3) the heating pulse is injected at the moment of maximum compression. However, experiments suggest that only about 25% of the laser energy can be transported to the core of the plasma using guiding cone targets. Therefore, it can be concluded that at the moment there is not any satisfactory approach for fast ignition which could assure the success of thermonuclear burn.

1.6 The main problems that are still unsolved in ICF

All the presented schemes show shortcomings that cannot be avoided at the present time. The most important ones are the hydrodynamic instabilities, that are present in every approach, especially Rayleigh-Taylor class of instabilities. These instabilities

always occur when a denser material is lying onto a less dense one; when the target is compressed , hot plasma pushes onto cold plasma, and this situation is equivalent to the one of a heavier fluid lying onto a lighter one (see fig. (1.7)). The important parameters for the growth rate of Rayleigh-Taylor instabilities during ablation are the wavenumber of the perturbations, the acceleration of the interface and the density gradient within the plasma. It turns out that the shortwavelenght harmonics of the perturbations are fortunately damped by thermal conductivity to a large extent, so the most destructive nonuniformities are the ones of intermediate wavelength. As a result of this perturbation, a mixing of the hot and cold plasma occurs, which leads to an undesired cooling of the hot region and consequently to a higher input of energy required for achieving ignition. Consequently, targets have to be designed in such a way that Rayleigh-Taylor (RT) instabilities are minimized as far as possible. Basically, we have two parameters which are crucial for target designing, the so-called *in-flight aspect ratio* (IFAR) and the *convergence radius*.
The *in-flight aspect ratio* (IFAR) is defined as the ratio of the shell radius R as it implodes to its thickness ΔR, that is smaller than the initial thickness because of the compression. RT instability sets an upper limit on this ratio, which results in a minimum pressure or absorbed driver irradiance. To give some numerical values, for $25 < \text{IFAR} < 35$, we have a peak of respectively ~ 100 Mbars for the pressure and $\sim 10^{15}$ W/cm^2 for the irradiance, in the case of megajoule-scale drivers. These minimum values depend on the required implosion velocity (typically in the range of $3 - 4 \times 10^7$ cm/s for ignition), which in turn is determined by the capsule size.

Another parameter that can be used to state if compression is sufficiently symmetric is the *convergence ratio* C_r, namely the ratio of the initial outer radius of the ablator to the final compressed radius of the hot spot. If a target with an initial radius R_A and average acceleration g has an acceleration perturbation of size δg on its surface, then its deviation from sphericity is given by:

$$\delta R = \frac{1}{2}\delta g t^2 = \frac{\delta g}{g} r(C_r - 1). \tag{1.17}$$

There is a limit for the asymmetry in the compression above which the conversion of the available kinetic energy into heating of the fuel is seriously compromised. Typically

it is required that the deviation δR be less than $r/4$, where r is the final compressed radius, which means that

$$\frac{\delta g}{g} \approx \frac{\delta v}{v} < \frac{1}{4(C_r - 1)}, \tag{1.18}$$

where v is the implosion velocity. Typical convergence ratios to the hot spot for an ignition or high-gain target design are 30-40. According to (1.18), this means that we require accelerations and velocities that are uniform to about 1%.

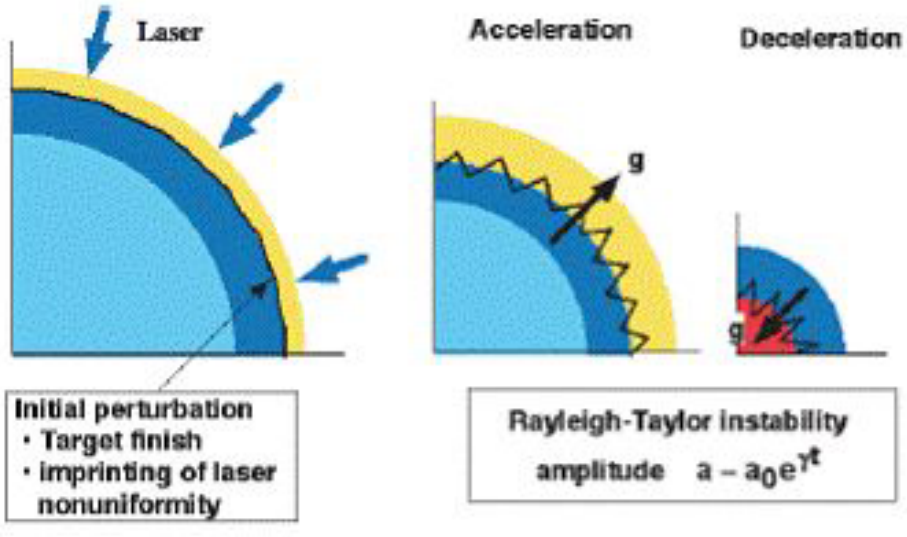

Figure 1.7: Hydrodynamic instability in direct-drive implosion - The biggest obstacle in direct-drive implosion is shell breakup and quenching of the hot spot by hydrodynamic instabtility

It is important to stress that, hydrodynamic instabilities are not only a drawabck themselves , but they also indirectly cause other problematic phenomena In fact, due to the presence of instabilities, it is not possible to use large and thin targets that would be ignited at low laser intensities, therefore we have to work with ultraintense lasers for which $I\lambda^2 \geq 10^{13} - 10^{14}$ W/cm^2 (I and λ are the laser intensity and wavelength, respectively). In such a regime, a current of hot electrons appears coming from the corona that can preheat the fuel, thus making the compression much more difficult.

Due to these problems, conventional laser-driven fusion facilities have to deal with the problems of low efficiency and the necessity for a high repetition rate for the beams. At the present time, facilities such as NIF (National Ignition Facility, at Lawrence

Livermore National Laboratory in California) use Nd-glass lasers, whose maximum efficiency can be about 15%; besides, one can expect at best one shot every 8h for NIF, while several shots per second would be needed . Apart from looking for alternative laser technologies with higher efficiencies, it is planned to study the possibility of using heavy-ion beams as a driver, because both their repetition rate and efficiency are much higher than the laser ones. Typicallly an ion beam induction accelerator can achieve an efficiency of 30%, twice the available one for laser facilities. A further advantage of ion beams is that the focusing onto the targets can be done by magnets. The high-velocity ions penetrate into a capsule made of a high-Z material (typically lead) until a certain distance, defined by Bragg peak, with relatively little loss in energy, if compared with the case of electromagnetic radiation, so the final focus magnet can much more easily shield fusion by products by appropriate design of the target chamber. Also this option presents some disadvantages: as the ions in the beam are all positively charged, they repel each other, the more so the denser the beam. The result is an unwanted spread of the beam, which at some point becomes dominated by space-charge effects. A way of overcoming this problem is to start with a relatively long pulse with a low density, and then compress it later by electrical fields and magnets; another way is to use a large number of beams, thus reducing the current in each single beam and consequently the spreading.

1.7 Present status of ICF projects

In spite of the development of more and more exhaustive analytical models and of recent technologic progresses, fusion conditions have not been achieved to date. However, two major milestones have been reached independently. In 1989 Yamanaka (10), from the Insititute for Laser technology at Osaka, performed an experiment with 600 times liquid density of compressed fuel, in practice the first true high-density target, but the reached temperature was of only 300 eV, far too low to produce an appreciable number of fusion reactions. In 1995 Soures *et al.*(11) have measured bursts of 2×10^{14} neutrons in the OMEGA direct-drive experimental program at Rochester laboratory, but they only obtained a density of $2 g/cm^3$ with a 15 keV temperature. The reason for which these records in density and neutron production have not yet been overcome is that the energy provided by the laser sets very important limits in this sense. Therefore new

progresses need first an improvement in laser design.
In the next years a proof of the scientific feasibility of inertial confinement fusion is in sight, to be obtained at two facilities: the National ignition Facility (NIF) settled at Lawrence Livermore National Laboratory in Berkeley, USA, and the Laser MegaJoule (LMJ) which is being built in Bordeaux, France. NIF is operative since May 2009, and its equipment is consituted by an Nd laser with 129 ion beams which can deliver 1.8 MJ of energy in the third harmonics ($\lambda_L = 0.35\mu$m) and a maximum power of 500TW. It will experiment mainly indirect illumination of targets, even if there is the possibility of doing some trials with direct-driven capsules. The probability of obtaininig controlled nuclear fusion in the context of the experiments conducted at these two facilities is considerable, because in previous experiments the following results for indirect drive have been demonstrated:

1. it is possible to achieve high efficiency in conversion of laser energy to X-ray radiation with a pulse intensity of $10^{14} - 10^{15}$ W/cm^2;
2. control of the simmetry of illumination can be obtained varying the focus point of the laser beams and the geometry of the *hohlraum*;
3. hydrodynamic instabilities can be limited for the case of indirect illumination;
4. suprathermal electrons produced by laser-plasma interaction can be controlled;
5. uncertainty in the state equations for DT and other materials eventually present in the capsule have been reduced;
6. uncertainties in the opacity of the materials in the *hohlraum* and in the capsule have been minimized.

Furthermore, the designs for the capsule and the *hohlraum* have been optimized with respect with the initial plans, so to enlarge the tolerance for the available energy. This means that little deviations between the original project and the real experiments can be balanced by the energy in excess. In fig. (1.8) the working point of targets at NIF is compared with targets for fast ignition characterized by different values of ρR. The threshold energy of the NIF target is 500 kJ and a gain of 15 to 20 times is expected, provided that the energies of the lasers are of about 200 kJ. On the other hand, the threshold energy of the targets for fast ignition has an order of magnitude of a MJ and

gains of 50 to 70 times are foreseen with the actual laser energies.
The experiments that will be conducted at NIF and LMJ will be scientific proofs rather

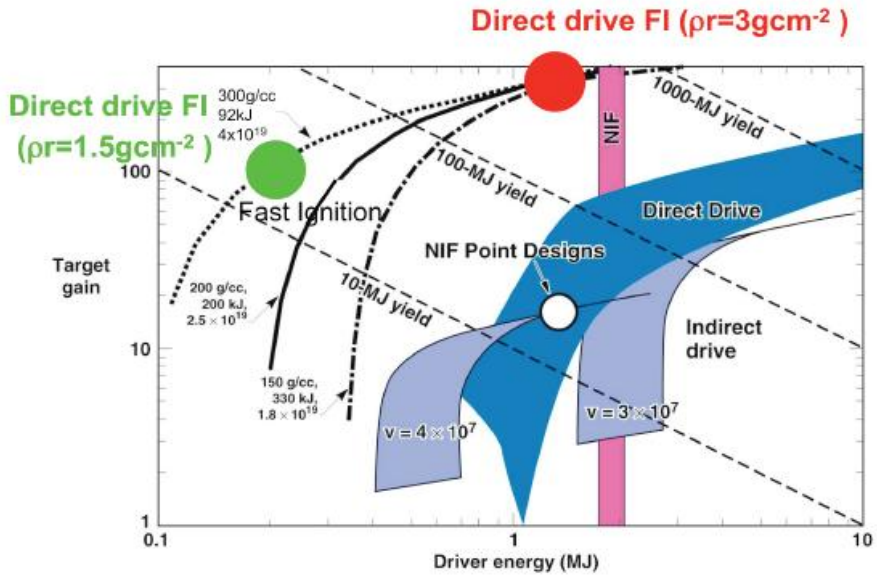

Figure 1.8: Comparison for NIF targets - Gain as a function of the energy for direct and indirect-driven targets at NIF and for fast ignition targets.

than first trials for a thermonuclear reactor. The latter requires the development of :

1. high efficiency $(10 - 15\%)$ lasers, capable of operating at frequencies of 10 Hz or higher;

2. methods of compression for the capsule that allow to reduce hydrodynamic instabilities, like the one that will be proposed in this thesis;

3. wrapping of the walls with new materials that are able to save the fusion energy and allow the production of other tritium.

At the present time, a new prototype of reactor for demonstration, denominated LIFE (*Laser Inertial Fusion Energy*, is being designed at LLNL, and it is expected to be operative in 2025. These prototype will use the technology already available at NIF (apart from the laser, that will be a diode pumped laser) and the materials currently existing. In its first phase, annual maintaning will be needed and the power will be an intermediate one; in a second moment the power will be elevated and the maintenance

will be required less frequently.
In addition to all that, a european project dedicated to demonstrate the feasibilty of laser driven fusion is being designed, named HiPER (*High Power Laser Energy Research*). At first it was thought that it could study the possibility of study fast ignition, but due to the lack of proof of the feasibility of this scheme the current idea is to study the approach of shock ignition (12). However, the scientific proof of principle for this second approach is not in sight yet either. In this thesis an alternative method for reducing hydodynamic instabilities will be shown, which could else serve as a basis for the design of new experiments to be done in the context of HiPER.

2

Dynamics of an ablation front

2.1 Introduction

The dynamics of an ablation front is a very complex phenomenon and, in the suitable conditions for ICF, a large variety of different situations can occur, depending on both the nature of the driver and the material with which it interacts. Basically, what makes the difference is the mechanism of energy transportation, which can be diffusive (*heat conduction* or *radiation*) or non-diffusive (*collisional transport* of particles or photons). In the first case the energy transport process is described by a Fourier law:

$$\mathbf{Q} = -\chi(\rho, T)\nabla T. \tag{2.1}$$

In the non-diffusive case, the Fourier law is not valid any more and energy transport follows Kirchoff's law:

$$\frac{d\mathbf{Q}_b}{dy} = \frac{\mathbf{Q}_b}{\lambda(\rho, T)}. \tag{2.2}$$

Then other effects can be present, due to suprathermal electrons or impurities in the ablated material which make the energy spectrum more complicated. In any case, the situations in which a laser or an ion beam act as a driver have to be distinguished,because of the fundamental differences in the energy deposition and penetration into matter.

2.2 General description of an ablation front

2.2.1 Laser energy deposition and transport

When an intense electromagnetic pulse ($> 10^{12} - 10^{14}$) hits a solid (for example, the fusion target), a heat wave arises, which can travel with either subsonic or supersonic velocity, depending on the characteristic time of pulse duration and the properties of the material itself (density and atomic number). In the first case, a shock wave is launched into the solid shell while a rarefaction wave travels in the opposite direction. This is what is called an *ablation front*. Typically the whole system, formed by the front and the material behind it, reaches a quasistationary configuration before the end of the radiation pulse. The end of the propagation of the shock marks the beginning of the acceleration process of the whole capsule. If we choose a well-defined coordinate system fixed to the ablation front, this acceleration now appears as a gravitational field recreating the situation of a heavier fluid lying above a lighter one, thus generating the conditions for the rise of Rayleigh-Taylor instability.

If the solid target is dense enough, in the evaporated material there will be some region in which the density is higher than the critical electron density (here simply indicated by n_{cr}) , given by:

$$n_{cr} = \frac{\epsilon_0 m \omega_L^2}{e^2} = 1.1 \times 10^{21} \left(\frac{\lambda_L}{1\mu\text{m}} \right)^{-2} \qquad [\text{cm}^{-3}]. \tag{2.3}$$

In equation (2.3) ω_L and λ_L are the laser frequency and wavelength, respectively. The laser radiation cannot propagate where $n > n_{cr}$, that is where the plasma frequency [1] is greater than the laser frequency $\omega_L = \frac{2\pi c}{\lambda_L}$; therefore, the laser will deposit its energy mostly at or near the critical surface, where $n = n_{cr}$ and, correspondingly, the mass density will be given by $\rho_{cr} = \frac{Am_p}{Z} n_{cr}$.

Typically, the critical surface is far enough from the ablation front and the two divide the target in three distinct regions: the *absorption domain*, the *transport domain* and the *compression domain* (fig.2.1). The absorption domain is the region of laser-plasma interaction (the so-called *corona*), namely the outer material that extends up to the

[1] typically a plasma has two characteristic frequencies, for electrons and ions respectively:

$$\omega_{pe} = \left(\frac{4\pi e^2 n_e}{m_e} \right)^{\frac{1}{2}}, \; \omega_{pi} = \left(\frac{4\pi Z^2 e^2 n_i}{m_i} \right)^{\frac{1}{2}}. \tag{2.4}$$

critical surface, and is characterized by a very high temperature (~ 100 eV) and a low density (< 0.01 g/cm^3). In the corona the electrons absorb the laser energy through a large variety of processes, mainly inverse bremsstrahlung absorption, resonance absorption, Brillouin and Raman scattering (see fig.2.2). Actually, the mechanisms with which the laser deposits its energy in the critical and supercritical region are only partially known. Then this energy is transported from the critical surface to the ablation surface, where the plasma is created and blows off in the direction of the laser at approximately the speed of sound c_s. In the transport domain the density is between 0.01 g/cm^3 and solid density, namely $\rho_0 = 1 - 3$ g/cm^3 for ablated DT mixture, with temperatures ranging between $\sim$ 30 eV and 1000 eV. Finally, behind the transport domain there is the compression domain, where densities range between ρ_0 and $10\rho_0$ at temperatures of $1 - 30$ eV.

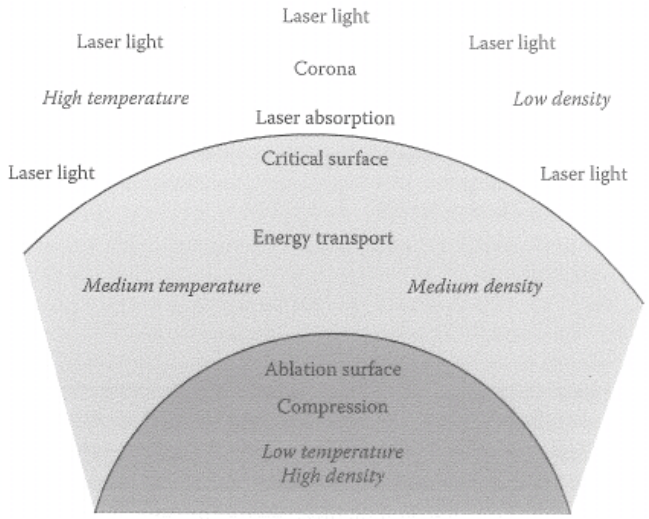

Figure 2.1: Laser plasma interactions - Schematic picture of laser-plasma interactions in an ICF target (source: Pfalzner, 2006 (2)).

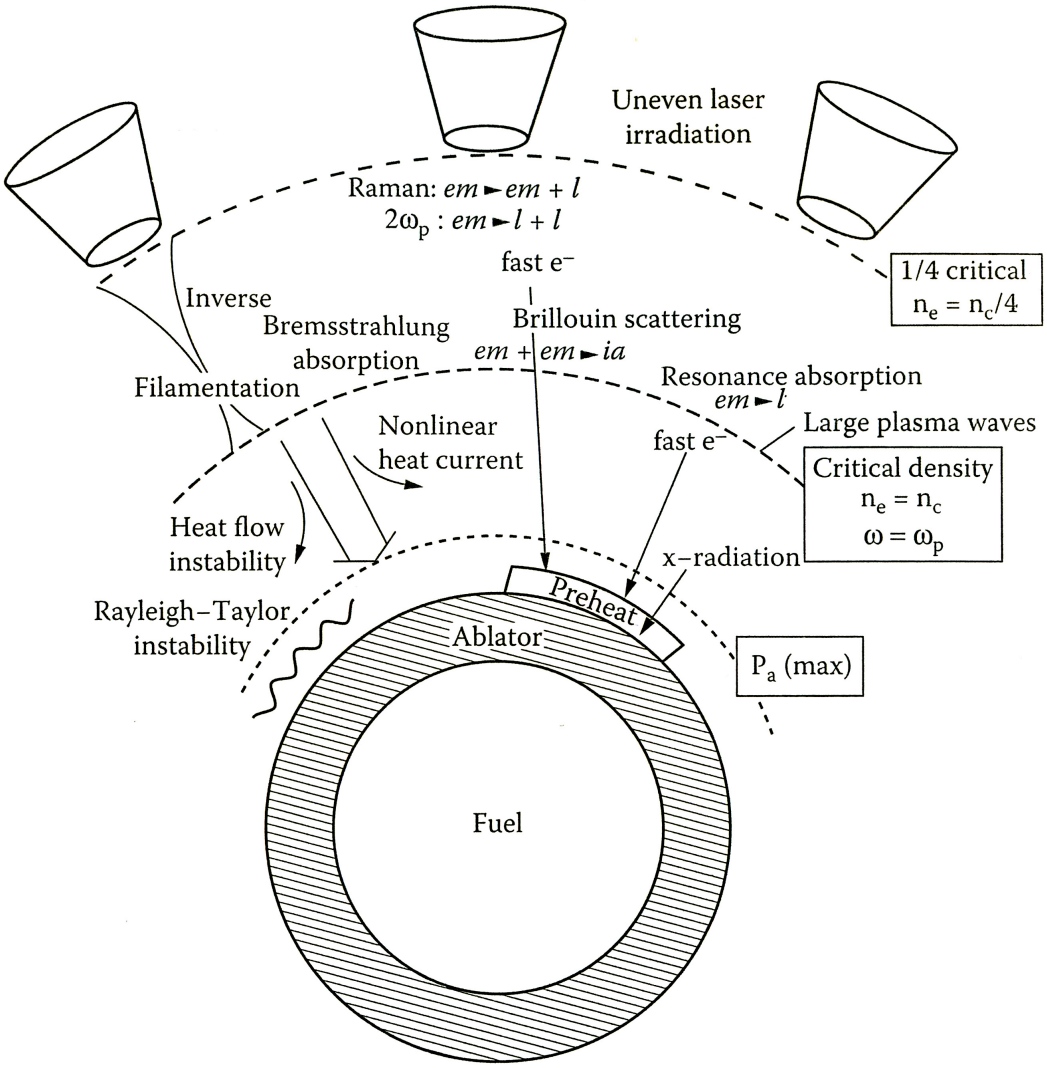

Figure 2.2: Physical processes in the corona - The different physical processes going on in the corona of a spherical target irradiated by laser beams. Here, em denotes electromagnetic waves, l Langmuir waves, and ia ion acoustic waves. (source: Pfalzner, 2006 (2)).

2.2.2 Ion beam energy deposition

The main difference in energy deposition between ion beams and lasers is that the ions penetrate and deposit their energy through a collisional process. In the case of ion beams, there is not a critical plasma density, but nevertheless the ions are stopped at a well-defined distance defined by the *Bragg peak* (see fig.2.3).

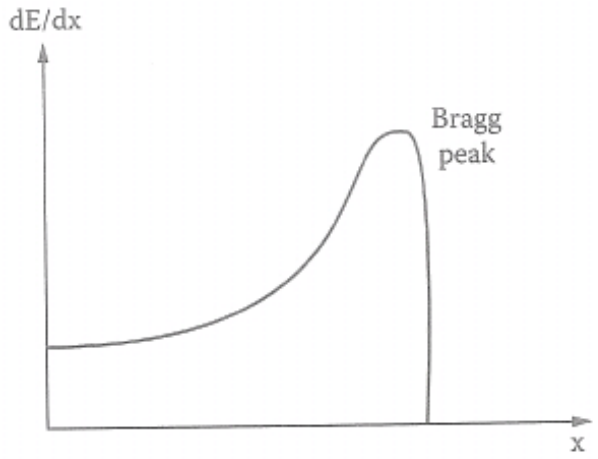

Figure 2.3: Bragg peak - The energy deposition by an ion beam as it penetrates into matter. (source: Pfalzner, 2006 (2)).

From an historical point of view the analytical treatment for the stopping of ions in a material has been developed first for low-intensity beams in cold matter: the first contribute was the one by Bethe in the 1930s and then several corrections have been introduced. The Bethe formula describes the energy loss per distance (dE/dx) of swift charged particles (not for electrons) travelling through matter, and states that it depends on the initial velocity and energy of the particles themselves, and on the atomic and mass number of both the ions and the stopping material. The general concept of particles penetrating into matter is similar in both the cases of a cold material and of a plasma, that is the ions are slowed down by excitation and ionization processes of the atomic electrons through Coulomb interactions . However, there is a fundamental difference: electrons in cold matter are assumed to be in a bounded state, while the plasma is fully ionized. It turns out that the plasma has a higher stopping power, and presents less electron recombination; this has a very important effect on the effective

charge of the projectiles. When ions enter in cold matter, their effective charge Z_{eff} runs through a series of equilibrium states essentially determined by their instantaneous velocities, and $dE/dx \propto Z_{eff}^2$; when the stopping material is a plasma, high nonequilibrium charge states of the ions are found due to the higher stopping power and the reduced recombinations. For high-intensity beams in highly ionized targets the Coulomb logarithm is increased, the ion range is shortened and the Bragg peak is more pronounced. It also turns out that, somewhat counter-intuitively, heavier ions can deposit more energy in a given depth than light ions. Although the ion beams are only singly or doubly charged, as soon as they hit the target, many of the remaining electrons are stripped away. The heavier ions loose more electrons and therefore end up with higher positive charges. This means that they are stopped faster and deposit more energy over a given distance than light ions. Typically the energy deposited by ions with $A = 36 - 82$ is $\sim 1 - 10$ GeV, while the one deposited by light elements such as lithium is around 50 MeV. There are two pratical consequences: the first one is that the beam intensity can be smaller for heavy-ion beams than for light-ion beams; the second one is that heavier ions allow us to obtain a volumetric heating, instead of the superficial one produced by light ion beams.

2.3 Basic model of the ablation front

For the ablation phenomenon in ICF a multitude of different situations can occur, as the transport mechanism can be driven by diffusion or radiation heat conduction, depending on the temperature gradients, and can also be affected by the eventual presence of suprathermal electrons or by the thermal radiation emitted by impurities of high Z number in the material. Due to this large variety of possibilities, all the models which have been developed so far for the dynamics of the ablation front are necessarily approximated. In the present work we will concentrate on the elements which are useful for our following understanding of the mechanism driving the Rayleigh-Taylor instabilities.

2.3.1 The sharp boundary model

The simplest treatments are founded on the *sharp boundary model* (SBM), first introduced by Bodner in 1974, then studied and modified by various scientists and finally

revisited by Piriz in 1997. According to such a model, the ablation front can be taken as a moving surface of zero thickness , which is initially at $y = 0$ and separates two homogeneous fluids of densities ρ_1, for $y > 0$, and $\rho_2 > \rho_1$, for $y < 0$, respectively (see fig.2.4). The heavy fluid is supported against an acceleration g by the lighter one ;it is important to notice that such acceleration is opposite to the density gradient and is taken in the direction of the positive y axis in the picture. Actually, in the ICF context

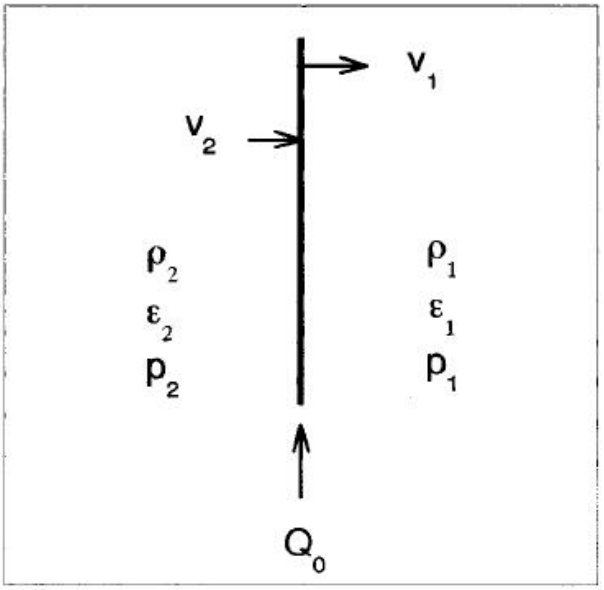

Figure 2.4: Sharp boundary model - Diagram of a steady ablation front described by means of the sharp boundary model (source: Piriz, 1997 (13)).

there is only one fluid instead of two, but there is an analogous situation as we have a lower density (hot plasma) on a higher density (cold plasma), and the acceleration g is generated by the ablation pressure. The main shortcoming of this model is that it requires additional information associated with the flow structure behind the ablation front, and such conditions cannot be introduced self-consistently with the SBM model. This is a problem that always arises when we try to study the ablation process by means of a discontinuity approximation and it is usually considered to be the reason for the disagreement between such models and the numerical calculations. However, as noticed by Piriz, this additional information comes from the boundary conditions on the ablation front and is given in a natural manner when the structure of the ablation is

resolved. For this we need to start directly from the fluid equations for the conservation of mass, momentum and energy:

$$\frac{\partial \rho}{\partial t} + \nabla \cdot (\rho \mathbf{v}) = 0 \tag{2.5}$$

$$\rho \frac{\partial \mathbf{v}}{\partial t} + \rho(\mathbf{v} \cdot \nabla \mathbf{v})\mathbf{v} = -\nabla p + \rho \mathbf{g} \tag{2.6}$$

$$\frac{\partial}{\partial t}\left[\rho\left(\frac{v^2}{2} + \epsilon\right)\right] + \nabla \cdot \left[\rho \mathbf{v}\left(\frac{v^2}{2} + \gamma\epsilon\right) + \mathbf{Q}\right] = \rho \mathbf{v} \cdot \mathbf{g} + W \tag{2.7}$$

$$\mathbf{Q} = -\kappa_D \nabla \epsilon, \tag{2.8}$$

where we have assumed that the fluid is an ideal gas with enthalpy coefficient γ. The quantities ρ, v, ϵ and $p = (\gamma - 1)\rho\epsilon$ are, respectively, the density, the velocity, the specific internal energy and the pressure of the fluid. Here $\mathbf{Q}$ is the energy flux driving the ablation, expressed in a very general way as a function of the specific internal energy; $\kappa_D = \chi\epsilon^\nu$ is the thermal conductivity, and it has been considered as an arbitrary power of the specific internal energy ϵ in order to let us define it later for the different cases of electronic thermal conduction ($\nu = 5/2$) or thermal radiation. The additional term W allows us to take eventually into account more complex energy transport mechanisms that could affect the physical description, like, for example, radiative processes and energy deposition by suprathermal electrons or ion beams. To study Rayleigh-Taylor instability, we can consider the stationary regime for the fluid equations above, which means that the time derivatives are zero. For the treatment of the steady energy flux in the supercritical region of the corona ($0 \leq y \leq y_{cr}$) we can neglect the effects of the acceleration g in the homogeneus regions on both sides of the front. This is a good approximation if the Mach number M_0 of the ablated flow is relatively small in the front: $M_0^2 = \frac{v_0^2}{c_0^2} << 1$ (c_0 is the adiabatic sound speed). This is really the case, so this approximation will be used throughout this treatment. The steady mass conservation equation states that the mass ablation rate is constant through the ablation region (eq.(2.5)):

$$\dot{m} = \rho_2 v_2 = \rho v = \text{const} \tag{2.9}$$

The momentum conservation law implies that the net momentum flux through the interface is constant (equation (2.6)):

$$p + \rho v^2 = p_2 + \rho_2 v_2^2, \tag{2.10}$$

where the quadratic velocity term can be neglected in the regime $M_0^2 << 1$ and the index 2 denotes the value on the ablation front at $y = 0$. In such a case, the role of the external forces is played by the ablation pressure p_2 , which is approximately the same at each side of the front, so that the momentum conservation is expressed by:

$$p = (\gamma - 1)\rho\epsilon = p_2. \tag{2.11}$$

Finally, we have to deal with energy conservation (eq. (2.7)) which in the regime $M_0^2 << 1$ reads :

$$\vec{\nabla} \cdot \left[\rho\vec{v}\gamma\epsilon - \kappa_D\vec{\nabla}\epsilon\right] = W. \tag{2.12}$$

Due to the fact that motion and flux take place in the y direction , the (2.12) becomes:

$$\frac{d}{dy} \cdot \left[\rho v\gamma\epsilon - \kappa_D\frac{d\epsilon}{dy}\right] = W. \tag{2.13}$$

Now, further specification about the nature of the term W is needed to solve this equation.

2.3.2 Ablation front driven by thermal diffusion

If the energy transport mechanism is heat conduction, the term W in the equation (2.7) is zero. This allows us to integrate the equation for the energy flux, taking into account equation (2.9), so that we can rewrite the (2.13) as

$$\dot{m}\gamma\epsilon = \kappa_D\frac{d\epsilon}{dy} + \text{const}, \tag{2.14}$$

and then we find the energy equation:

$$\kappa_D\frac{d\epsilon}{dy} = \gamma\dot{m}(\epsilon - \epsilon_2). \tag{2.15}$$

Therefore, recalling equations (2.7) and (2.11), we can summarize the physical description of an ablation front driven by thermal diffusion as

$$\kappa_D\frac{d\epsilon}{dy} = \gamma\dot{m}(\epsilon - \epsilon_2), \tag{2.16}$$

$$p \approx p_2 = \text{const}, \tag{2.17}$$

$$\frac{\epsilon}{\epsilon_2} \approx \frac{v}{v_2} \approx \frac{\rho_2}{\rho}. \tag{2.18}$$

$$\tag{2.19}$$

In addition to that, if the energy transport mechanism is electronic thermal conduction, we have: $\kappa_D = \chi\epsilon^{5/2}$ where χ is the coefficient of thermal conduction (14), and therefore equation (2.16) becomes:

$$\begin{aligned} y &= \frac{\chi}{\gamma\dot{m}} \int_0^\theta \frac{\epsilon^{5/2}}{\epsilon - \epsilon_2} d\epsilon \\ \rightarrow \frac{y}{L_2} &= \frac{2}{5}\left(\theta^{5/2} - 1\right) + \frac{2}{3}\left(\theta^{3/2} - 1\right) + 2\left(\theta^{1/2} - 1\right) + \ln\frac{\sqrt{\theta} - 1}{\sqrt{\theta} + 1}. \end{aligned} \tag{2.20}$$

where $\theta = \epsilon/\epsilon_2 = \rho_2/\rho$ (see eq.(2.18)).
The logarithmic term represents the behavior of the temperature in the cold, unablated region, and is important only when θ approaches 1. As we have assumed a strong density jump at the surface of discontinuity, it turns out that $\theta >> 1$ and the logarithm is negligible. Calculations made following this development are in very good agreement with numerical results (Kull,(15)) in almost all the cases of interest.

The evolution of the density profile for an ablation front driven by thermal conduction is shown in fig 2.5. From the density profile it is straightforward to obtain the corresponding velocity and energy profiles, according to equation (2.18).

2.3.3 Ion beam driven ablation front

The physical picture of an ion beam driven ablation front can be obtained on the basis of the theory of particle-particle interactions in a fully ionized plasma (Fokker-Planck theory). We know from the study of transport phenomena in a plasma that two types of interactions can be separated in a functional way: the weak, long-range, simultaneous interactions of many plasma particles, which is incorporated into average electric and magnetic fields, and the strong, short-range, binary interaction between two charged particles, mathematically described by a specific collision binary operator in the theory equations. In a fully ionized plasma, the scattering by a large-angle in a single encounter is much less likely than a net large-angle deflection due to the cumulative effect of the many small-angle scatterings that the electron experiences as it moves along its path. The exact particle dynamics is well described by classical multiple Coulomb scattering, which considers a test particle moving through a plasma volume with n scattering centers: as any individual deflection is assumed to be random, the average deflection will be zero, but the mean-square deflection will not be zero, producing a random walk

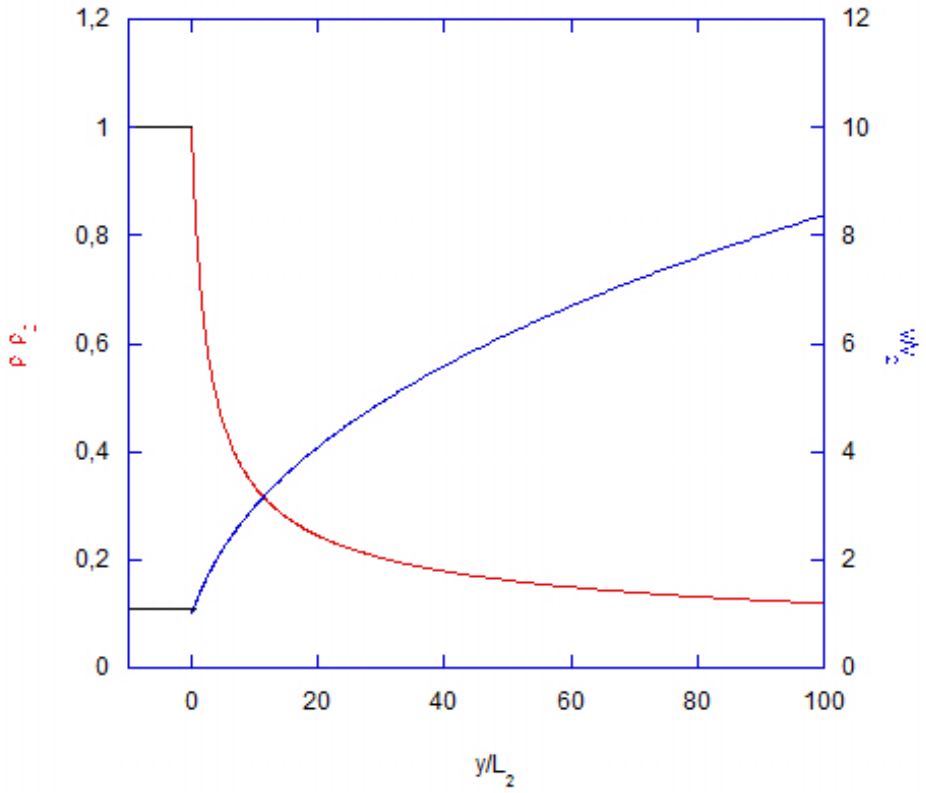

Figure 2.5: Profiles in an ablation font driven by thermal diffusion - Density and velocity profiles in the corona region close to an ablation front driven by thermal diffusion.

in a small angle away from the original direction of motion of the test particle. Actually, the rigorous treatment of collisions can be very well approximated by Fokker-Planck theory, according to which diffusion in plasma is controlled, not by the random walk of one particle through a fixed background, but by the change of the distribution of particles $f(\mathbf{v}, t)$ as a result of many small-angle scatterings with a variety of speeds distributed as specified in f.

We consider an intense beam of ions with mass m_b, charge number Z_b, and energy $E = (m_b/2)v_b^2$, which interacts with the corona plasma by classical Coulombian collisions. The equation for the energy flux (2.13) assumes the form

$$\frac{d}{dy}(\rho v \gamma \epsilon) = W, \quad W = \frac{dQ_b}{dy} = \frac{Q_b}{\lambda}, \tag{2.21}$$

where Q_b is the energy flux transported by the ions (neglecting backscattering) and $Q_b = \gamma \dot{m} \epsilon \propto E$:

$$\frac{1}{Q_b}\frac{dQ_b}{dy} = \frac{1}{E}\frac{dE}{dy} = \frac{1}{L},\ L = \frac{\alpha E^2}{\rho \psi(v_b/v_{the})}, \tag{2.22}$$

$$\alpha = \frac{Am_p}{Z} m_e m_b \frac{1}{2\pi Z_b^2 e^4 \ln\Lambda_b} \tag{2.23}$$

$$\psi(w) = \frac{2}{\sqrt{\pi}}\left[\int_0^w e^{-x^2} dx - we^{-w^2}\right]. \tag{2.24}$$

where m_e is the electron mass, $v_{the} = (2k_B T/m_e)^{1/2}$ the electron thermal velocity, Z the charge number of the ablation plasma and $\ln\Lambda_b$ is the Coulombian logarithm, which will be taken as a constant whose value is specified by the particular plasma conditions of interest: $\ln\Lambda_b \approx 8$. Here, L is the mean free path, that is the inverse of the relaxation time, and it can be expressed in different ways depending on $\psi(w)$, the well-known error function from the classical theory of multiple scattering (see Krall and Trievelpiece,(16)). Fundamentally, there are two limits in which it assumes a particular value:

1. if the velocity of the ions can be regarded as much greater than the thermal velocity of the electrons, that is $v_b >> \sqrt{\frac{2kT_e}{m_e}}$, we can take $\psi(w) \approx 1$, and then we have

$$L = \frac{Am_p m_e m_b}{\rho Z} \frac{E^2}{2\pi Z_b^2 e^4 \ln\Lambda_b}, \tag{2.25}$$

2. in the opposite limit of $v_b << \sqrt{\frac{2kT_e}{m_e}}$ we have that $\psi(w) \approx (4/3\sqrt{\pi})w^3$ and consequently

$$L = \frac{Am_p m_e m_b}{\rho Z} \frac{E^2}{2\pi Z_b^2 e^4 (4/3\sqrt{\pi}) w^3 \ln\Lambda_b}. \tag{2.26}$$

In the region close to the ablation front, the Mach number of the corona plasma is $M_1 << 1$ and the corona profiles can be approximately described by the following equations of continuity and momentum:

$$\mu_b E \approx \gamma_e \dot{m}(\epsilon - \epsilon_2), \quad \mu_b = n_b v_b; \tag{2.27}$$

$$p \approx p_2 = \text{const} \rightarrow \rho\epsilon = \text{const} \tag{2.28}$$

$$\dot{m} = \rho v = \text{const} \rightarrow \frac{\epsilon}{\epsilon_2} \approx \frac{v}{v_2} \approx \frac{\rho_2}{\rho}. \tag{2.29}$$

Here, n_b is the particle density of the ion beam and ϵ_2 is the specific internal energy of the medium ahead the front ($y < 0$). From the previous equation, knowing that $v_{the} \sim \sqrt{\epsilon} = \epsilon_2 \theta^{1/2}, v_b \sim \sqrt{\epsilon - \epsilon_2} = \epsilon_2(\theta - 1)^{1/2}$, we can get

$$\frac{v_b}{v_{the}} \approx \left[\frac{m_e}{(\gamma_e - 1)Am_p m_b} \frac{\gamma_e \dot{m}}{\mu_b}\right] \left(\frac{\theta - 1}{\theta}\right)^{1/2} = w_0 \left(\frac{\theta - 1}{\theta}\right)^{1/2}, \tag{2.30}$$

where $\theta = \frac{\epsilon}{\epsilon_2}$. As the temperature (and thus the internal energy) of the corona plasma ($y > 0$) is much greater than the one of the region ahead the front, we can assume that $\theta >> 1$. Consequently, we can take $\psi(w) \approx \psi(w_0)$ and the integral (2.24) becomes independent of θ.

Solving equations (2.22) to (2.30) we get:

$$\frac{y}{L_2} \approx \frac{1}{6} + \frac{1}{3}\left(\frac{\rho_2}{\rho}\right)^3 - \frac{1}{2}\left(\frac{\rho_2}{\rho}\right)^2, L_2 = \frac{\alpha E^2}{\rho\psi(w_0)};\ E_2 = \frac{\gamma \dot{m} \epsilon_2}{\mu_b}. \tag{2.31}$$

The behavior of the density profile for an ion beam driven ablation front is represented in fig.2.6 According to equation (2.28), once we have the density profile we can immediately obtain the corresponding velocity and energy profiles.

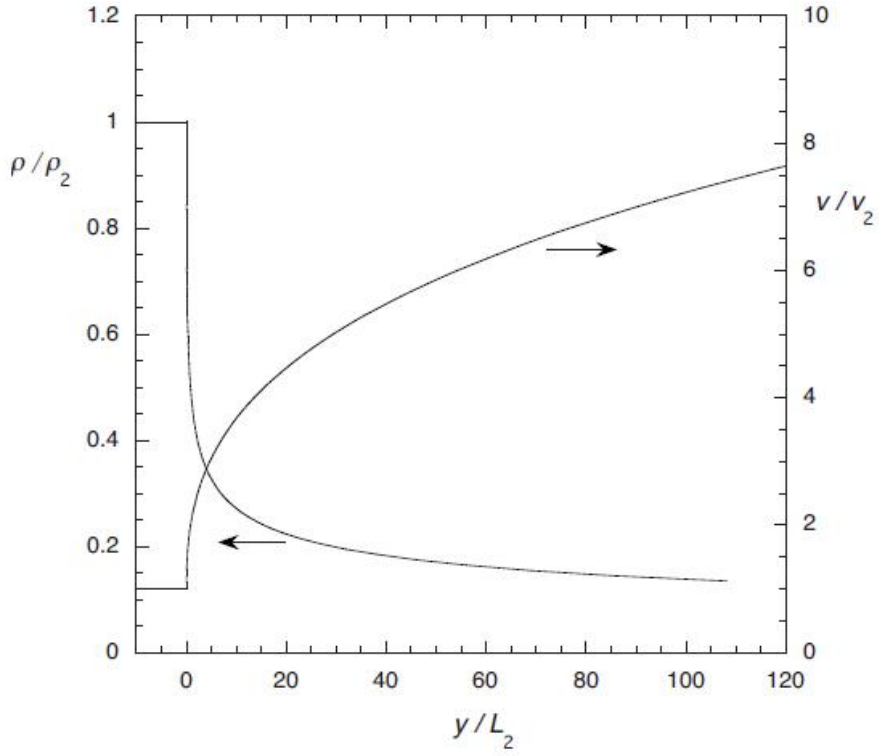

Figure 2.6: Profiles in an ablation front driven by ion beams - Density and velocity profiles in the corona region close to an ion beam driven ablation front (source: Piriz, 2009 (17)).

3

The Rayleigh-Taylor instability

3.1 Introduction

In the first chapter it has been stressed that a key point in achieving fusion is a homogeneous compression (except for the formation of the hot spot), which means aiming for a perfectly spherical implosion. In reality this ideal is never reached, mainly because of hydrodynamic instabilities of the shell which arise during both the acceleration and the deceleration phases of the implosion. During the acceleration phase, the mass ablation of the capsule's outer surface creates a local density gradient pointing from the denser, unablated shell material toward the hot, ablated plasma compressing the shell's corona, such as we have discussed in chapter 2 . In the shell's frame of reference, the acceleration of the bulk material is directed outward toward the corona, thereby making the shell's outer surface unstable due to the Rayleigh-Taylor instability. Similarly, the shell's inner surface becomes RT unstable during the deceleration phase, as the local density gradient points outward to the dense shell material from the less dense gas fill, and in the shell's frame of reference the acceleration points inward. In this thesis, we are dealing with the hydrodynamic instabilities which arise during the acceleration phase, but it is important to notice that it is not the only moment in which RT instability appears.

In ICF implosions, the RT instability is seeded both by inherent imperfections in the shell's surface finish, which cause deviation from sphericity, and by non-uniformities in the driver (x-ray, laser or ion beam), which imprint perturbations on the shell's outer surface. In indirect-drive ICF, the high uniformity of the black-body x-ray ra-

diation results in a negligible level of imprinted perturbations on the outer shell surface.Therefore the seeds of RT instability are mostly introduced by capsule surface roughness. In direct-drive ICF, however, the laser beam intensity is not highly uniform spatially, such that the direct illumination of the shell leads to high levels of laser imprinting that cause the rise of RT instability at the outer surface. Advances in beam-smoothing techniques have reduced laser imprint in direct-drive implosions, but not enough to avoid significant lowering of the performance of the direct-drive implosion due to nonuniform irradiation. For all these reasons, RT instability has been widely studied since the early times of research on inertial confinement fusion, but due to the difficulty in understanding the basic mechanism of the phenomenon, the history of its analysis is full of misunderstandings. Let's examine first the historical treatment of the so-called "classical" Rayleigh-Taylor instability, namely the one concerning the case of an interface between two ideal, incompressible fluids without flux of mass across the interface. In the simplest analysis, the perturbation is decomposed in a Fourier development . If its mode amplitudes are much smaller than their corresponding wavelengths, it is said to be in the so-called "linear" regime, in which each mode evolves independently, growing exponentially in time with its own characteristic growth rate. If the fluids are separated by a sharp boundary, the mode amplitude evolution in the linear regime can be derived explicitly to first order, yielding the following expression for each time-dependent amplitude $\xi(t)$ corresponding to a single mode:

$$\xi(t) = \xi_0 e^{\Gamma t}. \tag{3.1}$$

Here ξ_0 is the initial amplitude of the perturbation, t is the time and Γ is the RT linear growth rate, which, according to the theory (to be addressed in the next paragraph) is given by

$$\Gamma = \sqrt{A_T k g}, \tag{3.2}$$

where A_T is the well-known Atwood number, and in this case it will be expressed in terms of the density of the heavy (ρ_h) and light (ρ_l) fluids, respectively:

$$A_T = \frac{\rho_h - \rho_l}{\rho_h + \rho_l}. \tag{3.3}$$

Equation (3.2) shows that the Rayleigh-Taylor growth rates increase as the perturbation wavelength $\lambda = 2\pi/k$ decreases, and corresponds to the case of a sharp variation in the

density at the interface between the two fluids. If the density profile smoothly changes over a length similar to or greater than the perturbation wavelength, the Rayleigh-Taylor instability is mitigated by the finite density gradient at the unstable interface, and the growth rate of short wavelength modes tends asymptotically to the constant value

$$\Gamma = \sqrt{g/L_m} \tag{3.4}$$

where L_m is the minimum density-gradient scalelength defined as

$$L_m = \min\left(\frac{1}{\rho}\frac{\partial \rho}{\partial z}\right)^{-1}, \tag{3.5}$$

with z as the coordinate in the direction of density variation. In the long wavelength limit ($\lambda >> L_m$), however, the finite density gradient scale lengths have no effect and we recover the expression (3.2)

It is important to notice that the linear regime in the case of two classical fluids is maintained while the mode amplitudes are of the order of $k\xi << 1$; beyond this limit we enter the "nonlinear" regime, where the individual modes interact, higher order terms become important, and mode growth rates saturate. Since the amplitude regime where the transition from linear to nonlinear occurs scales with the wavelength, it turns out that shorter wavelenghts saturate at lower amplitudes.

The development of Rayleigh-Taylor instability during the acceleration phase of compression is quite different from the classical case. In the context of the first studies of RT instability in ICF in the '70s , it was noticed that mass ablation can reduce the local growth rate of the RT instability, in a manner that was not completely understood until the 90's. However, at that time it was already noticed that the level of growth rate mitigation was largely determined by the ablation velocity, which represents the speed of propagation of the heat front inside the shell material. According with equation (2.9), the ablation velocity is given by:

$$v_2 = \frac{\dot{m}}{\rho_2}, \tag{3.6}$$

where we remember that $\dot{m}$ is the mass ablation rate and ρ_2 is the shell's outer surface density. In a paper written in 1972 (18),and based on laser directly driven implosion of bare drops or shells of DT, Nuckolls used a dispersion relation based on a model of

"fire polishing" during the ablation process and proposed the following expression for the growth rate:

$$\gamma^2 = ka - k^2\frac{p_2}{\rho} = ka(1 - k\Delta R), \tag{3.7}$$

where p_2 is the ablation pressure [see equation (2.11], k is the wave number, and ΔR is the shell thickness. Equation (3.7) predicts that all wavelengths shorter than $2\pi\Delta R$ are stabilized, but the model by Nuckolls was soon proven to be too optimistic, as it assumed that implosions with absorbed laser intensities approaching 10^{17} W/cm^2 would be feasible and thus concluded that ignition at laser energies of $\sim 1kJ$ might be achievable. Early experiments indicated that, because of reduced absorption and hot electron production by plasma collective processes, laser intensities would be limited to 10^{14} to a few times 10^{15} W/cm^2, depending on the laser wavelength. By 1972, numerical calculations indicated that direct-drive capsules designed for ignition and gain would have much higher instability growth rates than indicated by equation (3.7). In 1985, Takabe et al. (19) proposed a dispersion relation for Rayleigh-Taylor instability in the case of direct-drive illumination of spherical targets, namely

$$\gamma = \alpha\sqrt{kg} - \beta k v_2. \tag{3.8}$$

Takabe's formula is obtained by fitting a series of numerical calculations with very small density gradients at the ablation front and can be modified to account for density gradients which can result in significant stabilization for certain types of direct drive implosions:

$$\gamma = \alpha\sqrt{\frac{kg}{1 + kL_m}} - \beta k v_2. \tag{3.9}$$

Now, the term kL_m takes into account the finite density scale lengths effects.
In both the (3.8) and the (3.9) g is the acceleration of the outer material.

The linearized conservation equations for mass, momentum and energy are solved by Takabe using sophisticated numerical methods which can be fitted by the expressions above. The values of the parameters α and β derive from analytical fitting of numerical calculations; in particular, β oscillates between 1 (for radiation driven implosion) and 3 (for direct drive implosion). This fact could lead to the wrong conclusion that in the case of indirect drive compression the instability growth rate is higher; actually, in this case the ablation velocity at a typical intensity of 10^{15} W/cm^2 is about 10 times larger than the one for direct drive. The higher ablation rates also result in the possibility

to have thicker shells and larger density scale lengths L_m for radiation-driven capsules. In optimized capsules, the ablation and density scale-length effects are about equally important stabilizing effects.

Takabe's generalized formula has been widely used until the end of the 90's, when the introduction of the work by Betti and Goncharov based on asymptotic matching for solving the linearized equations allowed to find a more accurate analytical expression for the growth rate. Soon after this work, Piriz was able to derivate the same expressions by means of a much simpler model based on the sharp boundary model.At present times, all efforts are concentrated on improving the sharp boundary model to get more effective analytical treatments based on solid physical argumentation. More recently it has been shown that it is possible to obtain the same formulas from an even simpler physical model of the ablation front instability (Piriz 2009,(17)). Such a model will be discussed in this chapter and it will be used in this thesis for the study of the dynamic stabilization of RTI in the ablation front.

3.1.1 The classical Rayleigh-Taylor instability

Before addressing the case of RTI in an ablation front, we go into the analytical model of the RT instability for the case of two ideal fluids introduced by Piriz et al. in 2006 (20), then discussed again in 2010 (21) . This treatment starts from the classical RTI and then includes the surface tension and viscosity effects. This study will serve as a basis to understand analogous work done for the case of the instability at the ablation front, where we found equivalent effects to the ones of viscosity and surface tension.

The simplest case in which the Rayleigh-Taylor instability arises is for two semi-infinite incompressible and inviscid fluids with a surface of contact initially at $y = 0$ (see fig.3.1 a)). The denser fluid of density ρ_2 lies above the lighter fluid of density $\rho_1 < \rho_2$ in a uniform gravitational field g. We will hypothesize that initially the two fluids are at equilibrium and the interface between them is perfectly planar, so that the fluid elements on each side of the interface immediately above and below will have the same pressure $p_1 = p_2 = p_0$. Now, let us introduce a small perturbation $\xi(x)$ at the interface such that the elements originally at $y = 0$ are quasistatically translated to the new position $y = \xi(x)$ (see fig.3.1 b)). As the pressure in an incompressible fluid decreases linearly with depth, the elements at a deeper position ($\xi > 0$) will feel a

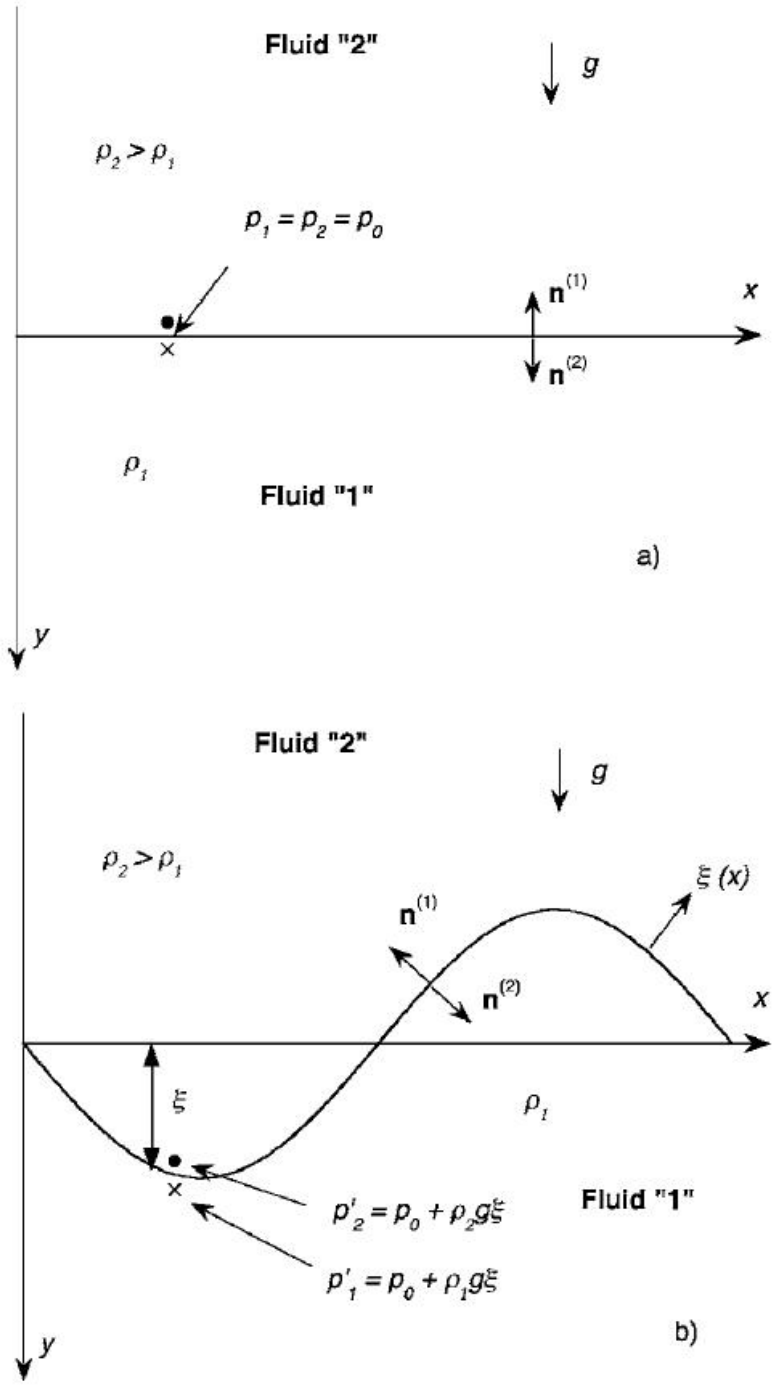

Figure 3.1: RTI at the interface between two fluids - Diagram of the interface between two fluids : a) planar interface in equilibrium, b) perturbed interface (source: Piriz et al. , 2006 (20)).

pressure greater than p_0, whereas the elements at $y < 0$ will feel a pressure less than p_0. The pressure also increases proportionally to the fluid density, so for $\xi > 0$ it increases more on the side of the fluid with higher density. The pressure of the fluids on each side of the translated interface is:

$$p_1' = p_0 + \rho_1 g\xi, \tag{3.10}$$

$$p_2' = p_0 + \rho_2 g\xi. \tag{3.11}$$

This means that the perturbation introduces a pressure difference $\Delta p = (\rho_2 - \rho_1)g\xi$ across the interface, which tends to deform it further. This pressure difference drives the motion of the interface according to Newton's second law of motion:

$$m\ddot{\xi} = \Delta p A, \tag{3.12}$$

where A is the area of the interface and m is the mass of the fluids contained within the characteristic distance of the motion. It can be demonstrated that, starting from the assumptions that the velocity field of an inviscid fluid is irrotational and incompressible , it is possible to find that the Rayleigh-Taylor instability induces surface modes that decay from the interface as exp(-ky), where $k = 2\pi/\lambda$ is the wave number and λ is the wavelength of the perturbation. Such an explanation for Rayleigh-Taylor instability is less physical than the one exposed in the previous paragraph, but it will be useful for what follows. The consequence is that in the linear regime the intensity of the motion decays with the distance from the interface with a characteristic length k^{-1}, and so does the effective mass participating in the motion itself:

$$m = m_1 + m_2 = \rho_1 \frac{A}{k} + \rho_2 \frac{A}{k}. \tag{3.13}$$

Here, m_1 and m_2 are the fractions of mass moving with the interface for the light and heavy fluids, respectively. As in the linear regime we have that $k\xi << 1$, k^{-1} is the only relevant scale length that is involved in the determination of the density profile. Now, using equations (3.12) and (3.13), the equation of motion of the interface can be written as:

$$\frac{(\rho_1 + \rho_2)}{k}\ddot{\xi} = (\rho_2 - \rho_1)g\xi, \tag{3.14}$$

or

$$\ddot{\xi} = A_T k g \xi,\ A_T = \frac{\rho_2 - \rho_1}{\rho_2 + \rho_1}, \tag{3.15}$$

where A_T is the Atwood number. The expression for the growth of the amplitude is easily found integrating the (3.15) , and it turns out to have an exponential behavior:

$$\xi = \xi_0 \cosh(\gamma t) + \frac{\dot{\xi_0}}{\gamma} \sinh(\gamma t), \tag{3.16}$$

with initial conditions of perturbation and velocity given, respectively, by $\xi_0 = \xi(t=0)$ and $\dot{\xi_0} = \dot{\xi}(t=0)$. The growth rate is $\gamma = \sqrt{A_T k g}$.

Equation (3.15) summarizes the results obtained originally by Lord Rayleigh by using the normal modes method; its derivation can be extended to more complex situations such as those involving nonideal fluids. In the latter case additional forces F_i on the interface must be included into the equation of motion. The most general form for the equation of motion is

$$\frac{d}{dt}[(m_1 + m_2)\dot{\xi}] = (\rho_2 - \rho_1) g \dot{\xi} A + \Sigma F_i, \tag{3.17}$$

where the time derivative on the left hand side allows for the possibility of a flux of mass across the interface as occurs for example, in an ablation front. In the next subsection it is shown how to obtain the forces F_i for the cases in which surface tension and viscosity are present.

3.1.2 Surface tension and viscosity effects

3.1.2.1 Surface tension

We first consider the case of two inviscid fluids with a surface tension coefficient σ between them, which in general has an exact solution that can be expressed in simple terms. In this framework, the force F_{ST} on the interface between the fluids due to the surface tension is given by the Laplace formula:

$$F_{ST} = A \delta p_{ST} = A \frac{\sigma}{R_C}, \tag{3.18}$$

where R_C is the radius of curvature of the interface surface $\xi(x)$:

$$R_C = \frac{[1 + (d\xi/dx)^2]^{3/2}}{d^2\xi/dx^2}. \tag{3.19}$$

Taking into account that in the linear regime $k\xi << 1$, now we apply a sinusoidal perturbation $\xi(x) \propto \exp(ikx)$. This means that the radius of curvature becomes

$$R_C = \frac{[1 + (ik\xi)^2]^{3/2}}{-k^2\xi} \approx -\frac{1}{k^2\xi}. \tag{3.20}$$

Now, substituing the expressions (3.20) into equation (3.18)and using equation (3.13), we get the following equation of motion of the interface:

$$\ddot{\xi} = \left(A_T k g - \frac{\sigma k^3}{\rho_1 + \rho_2} \right) \xi. \tag{3.21}$$

The last equation coincides with the exact result given by normal modes theory. It describes the asymptotic exponential growth of the perturbation amplitude with a growth rate $\gamma_{ST}[\xi \propto \exp(\gamma_{ST} t)]$,

$$\gamma_{ST} = \sqrt{A_T k g - \frac{\sigma k^3}{\rho_1 + \rho_2}} \tag{3.22}$$

Setting the growth rate equal to zero, we find the cutoff wave number k_c, which has the following meaning: the restoring force stabilizes the interface for all perturbation wave numbers larger than k_c. Its expression is given by

$$k_c = \sqrt{\frac{(\rho_1 - \rho_2) g}{\sigma}}. \tag{3.23}$$

3.1.2.2 Viscous fluids

The calculation with the normal modes method for Rayleigh-Taylor instability in the interface between viscous fluids with dynamical viscosities μ_1 and μ_2 leads to the numerical solution of a fourth degree polynomial. Here this procedure will not be followed, but the approach contained in (20) will be exposed; such a treatment provides approximate but very accurate results that yield insight into the physical effects of the viscosity on the instability growth.

We know from continuum mechanics that the force per unit of area f_i due to an arbitrary fluid on an interface is (Landau, (22)) :

$$f_i^{(\nu)} = p'_\nu n_i^\nu - S_{ij}^\nu n_j^\nu, \tag{3.24}$$

$p'_\nu = p_0 + \rho_\nu g \xi$ is the in pressure on the perturbed interface due to the incompressible fluid $\nu (\nu = 1, 2)$. The notation has been chosen so that $i, j = x, y, z$ denote the coordinate directions, $n_j^{(\nu)}$ is the jth component of the unit vector $\mathbf{n}^{(\nu)}$ directed outward along the normal of the interface, and $S_{ij}^{(\nu)}$ is the deviation of the stress tensor $\sigma_{ij}^{(\nu)} = -p_\nu \delta_{ij} + S_{ij}^{(\nu)}$. Clearly, $S_{ij}^{(\nu)}$ accounts for the nonisotropic part of the surface forces.

For a Newtonian incompressible fluid the deviatoric part of the stress tensor is given by the following constitutive relation

$$S_{ij}^{\nu} = 2\mu D_{ij}^{\nu},\ D_{ij}^{\nu} = \frac{1}{2}\left(\frac{\partial v_j^{\nu}}{\partial x_j} + \frac{\partial v_j^{\nu}}{\partial x}\right), \tag{3.25}$$

where D_{ij}^{ν} is the strain rate tensor, v_j^{ν} are the corresponding components of the fluid velocities, and μ_2 is the dynamical viscosity coefficient. If we consider two-dimensional perturbations ($i = x, j = y$) and ignore surface tension, the vertical force per unit area due to each fluid is

$$f_y^{\nu} = p'_{\nu} n_y^{\nu} - S_{yy}^{\nu} n_y^{\nu} - S_{yx}^{\nu} n_x^{\nu}. \tag{3.26}$$

In the linear regime $n_x^{\nu} \sim k\xi << 1$ and $|n_y^{(\nu)}| \approx 1$ so that the last term in above equation is negligible and we can express the force per unit of area on the interface due to the two fluids as

$$f_y^{\nu} = p'_{\nu} n_y^{\nu} - S_{yy}^{\nu} n_y^{\nu}. \tag{3.27}$$

The total force $F_{y\nu}$ on the interface due only to the effects of the viscosity of both fluids is

$$F_{y\nu} = (f_y^{(1)} + f_y^{(2)})A - \delta pA = 2\mu_1 \frac{\partial v_y^{(1)}}{\partial y} A - 2\mu_2 \frac{\partial v_y^{(2)}}{\partial y} A, \tag{3.28}$$

where $\delta p = (\rho_2 - \rho_1) g\xi$ is the term due to gravity effects, which has been subtracted in order to calculate only the force due to the viscous effects. From normal modes theory we know that any linear perturbation can be written as a combination of simple perturbations in exponential form (Fourier components) with different wave numbers k. Therefore, we can assume a perturbed velocity field of the form:

$$v_y^{(1)} \propto e^{ikx - qy}, v_y^{(2)} \propto e^{ikx + qy}, \tag{3.29}$$

where q is the longitudinal wave number, which in principle can be calculated in a consistent way from the equations of mass, momentum, and energy conservation. However, considerable simplification can be achieved by supposing that the velocity field can be taken as the one corresponding to an inviscid fluid.This means that we can take $q \approx k$ and after performing the velocity derivatives in equation (3.28) we get:

$$F_{y\nu} \approx -2(\mu_1 + \mu_2) k \dot{\xi} A, \tag{3.30}$$

where

$$v_y^{(1)}(y = 0), v_y^{(2)}(y = 0) = \dot{(\xi)}. \tag{3.31}$$

If we substitute (3.30) into the equation of motion (3.17), we obtain

$$\ddot{\xi} = A_T k g \xi - \frac{\mu_1 + \mu_2}{\rho_2}(1 + A_T)k^2\dot{\xi}. \tag{3.32}$$

As in the previous cases, by setting $\xi \propto \exp(\gamma_v t)$ we obtain a quadratic equation whose solution yields the asymptotic growth rate:

$$\gamma_v^2 + \frac{(\mu_1 + \mu_2)}{\rho_2}(1 + A_T)k^2\gamma_v - A_T k g = 0. \tag{3.33}$$

The above equation is not exact, but it is a well-known analytical approximation accurate to within 11 % which, furthermore, has been derived using physical arguments that show the effect of the viscosity on damping the instability growth rate. This procedure avoids dealing with the exact dispersion relation, which would lead to a fourth-order polynomial that must be solved numerically.
Fianlly, we can resume all the previous treatment and write an equation of motion which takes into account the effects of both viscosity and surface tension:

$$\ddot{\xi} = A_T k g \xi - \frac{(\mu_1 + \mu_2)}{\rho_2}(1 + A_T)k^2\dot{\xi} - \sigma k^3 \frac{(1 + A_T)}{2\rho_2}\xi. \tag{3.34}$$

The corresponding asymptotic growth rate is

$$\gamma^2 + \frac{(\mu_1 + \mu_2)}{\rho_2}(1 + A_T)k^2\gamma - \left[A_T - \sigma k^3 \frac{1 + A_T}{2\rho_2}\right] = 0. \tag{3.35}$$

3.2 RTI in an ablation front

The first treatments based on the sharp boundary model to study RTI in an ablation fronts used simply the fluid equations (2.5) -(2.8) presented in the previous chapter for a stability analysis of the front by applying to them the normal modes procedure as in (13). Here a more physical approach to the same problem will be shown, introduced in 2009 in the article by Piriz et al. (17). The scheme of the sharp boundary model is still taken into account , but a suitable expression for Newton's second law is found in terms of the parameters given before, and physical boundary conditions are stated to close the problem.

As it is already well known (Landau, (22)), if we consider some volume of a Newtonian fluid, the ith component of the flux of the momentum across the unit boundary

surface area is given by the the projection of the *perturbed momentum flux density tensor* on the unit vector n_k along the outward normal to the surface:

$$\Pi_{ik} n_k = p\delta_{ik} n_k + \rho v_i v_k n_k - S_{ij} n_k. \tag{3.36}$$

Since we are considering ideal fluids, the deviatoric part S_{ij} is zero.
In the vertical direction, Newton's second law for the interface is:

$$\frac{d}{dt}[(m_1 + m_2)\dot{\xi}] = \delta\Pi^{(1)}_{yy} n^{(1)}_y + \delta\Pi^{(2)}_{yy} n^{(2)}_y, \tag{3.37}$$

where $n^{(\nu)}_y$ is the vertical component of the unit vector $\mathbf{n}^{(\nu)}$ directed outward along the normal to the interface ($n^{(2)}_y = -n^{(1)}_y$), and $\delta\Pi^{(\nu)}_{yy}$ is the vertical component of the perturbed momentum flux density tensor $\Pi^{(\nu)}_{ik}$ in the medium $\nu(\nu = 1, 2)$. In the previous equation $p^{(\nu)}, \rho_\nu, v^{(\nu)}_i$ are the pressure, the density, and the fluid velocity. Furthermore, m_ν is the mass per unit area of the fluid involved in the motion due to the perturbation, and can be expressed in terms of the density ρ and the perturbation wave number k in the following way:

$$m_\nu = \frac{\rho_\nu}{k}, \tag{3.38}$$

because we are dealing with surface modes that decay exponentially from the interface with the characteristic length k^{-1}. If we denote with v_ν the unperturbed velocities of the fluids, then the perturbed ones are given by

$$v^{(1)}_y = v_1 + \dot{\xi}, \qquad v^{(2)}_y = v_2 - \dot{\xi}, \tag{3.39}$$

where $\dot{\xi}$ is the velocity of the front moving because of the perturbation . In the (3.39) $v^{(2)}_y$ is the ablation velocity, or, in the reference frame fixed to the nonablated material, it is the front recession velocity due to ablation; in the same reference frame, $v^{(1)}_y$ is the velocity with which the material is ejected from the front. In the same manner the perturbed mass ablation rates (namely the mass variations per unit time, also called mass evaporation rate) are:

$$\dot{m}_1 = \dot{m} + \delta m; \qquad \dot{m}_2 = \dot{m} - \delta m, \tag{3.40}$$

where $\dot{m} = \rho_\nu v_\nu$ denotes the mass ablation rate at equilibrium and the mass perturbations of the two fluids are given by $\delta\dot{m}_1 = -\delta\dot{m}_2 = \delta\dot{m}$.

According to the hydrostatic equation for an incompressible fluid, the perturbed pressures are

$$p^{(1)} = p_0 + \rho_1 g\xi; \qquad p^{(2)} = p_0 + \rho_2 g\xi, \tag{3.41}$$

where $p_0 = \rho_2 gh$ (h is the thickness of the nonablated phase and it is assumed that $kh >> 1$) is the pressure on the interface at equilibrium. Thus the pressure perturbations turn out to be $\delta p^{(1)} = \rho_1 g\xi$, $\delta p^{(2)} = \rho_2 g\xi$.

With the previous considerations, we can write the expression for the perturbed momentum flux density tensor as (actually the variations are only referred to the vertical components of the velocities):

$$\delta\Pi_{yy}^{(\nu)} = \delta p^{(\nu)} + \delta\dot{m}_\nu v_\nu + \dot{m}\delta v_y^{(\nu)}. \tag{3.42}$$

Using equations (3.39), (3.40), (3.41) and (3.42), the (3.37) becomes:

$$2\dot{m}\dot{\xi} + \frac{\rho_1 + \rho_2}{k}\ddot{\xi} = (\rho_2 - \rho_1)g\xi - 2\dot{m}\dot{\xi} - \delta\dot{m}(v_1 + v_2). \tag{3.43}$$

The last term on the right side of equation (3.43) is the "surface tensionlike" force, and it is the result of the reaction due to the perturbation $\delta\dot{m}$ in the mass ablation arising as the interface moves through the temperature gradient of the ablative corona. The perturbation $\delta\dot{m}$ is determined by the particular mechanism driving the ablation process.

Actually, equation (3.43) is valid for all kinds of interfaces, independently of the fact that they are or not ablation fronts. Some additional information is needed to specify that the modell deals effectively with an ablation front: this condition is, consistently with the previous thin front approximation, that the isotherms move with the front, or, that is the same, the front is an isotherm. This fact has been originally noted by Bodner (23) and Baker (24),(25) but the first correct physical picture was given in (17). Such a property of the front arises from the fact that the maximum deposition rate of the energy flux takes place on the ablation surface, independently of the displacement produced. As a consequence, neither the energy flux nor the temperature at the front are affected by the kind of perturbation, which means that for every fluid element on the front with unperturbed temperature $\epsilon_0(y = 0)$ that is displaced from $y = 0$ to $y = \xi$ the perturbed temperature is $\epsilon(\xi) = \epsilon_0(0)$ and the perturbation of the specific internal energy can be written as follows:

$$\delta\epsilon = -\xi\frac{d\epsilon_0}{dy}\Big)_{y\approx 0}. \tag{3.44}$$

Now the key point for directing this analysis towards a specific ablation front is finding the expression for the surface tensionlike force determined by the perturbation in the ablation rate, for each driving mechanism, namely in both cases of ablation driven by thermal diffusion and by ion beams.

3.2.1 RTI in ablation fronts driven by thermal conduction

For ablation fronts driven by thermal diffusion, thermal flux is given by the Fourier heat conduction equation (2.1) with $\kappa_D = \chi\epsilon^{5/2}$. Furthermore, we can use equation (3.44) to express δQ_y in terms of the unperturbed thermal flux Q_0, which relates to the global properties of the corona and, as we have already said before, is a known parameter in the SBM model:

$$\delta Q_{T0} \approx k\xi Q_{T0}; \qquad Q_{T0} = \kappa_D \frac{d\epsilon}{dy}\Big)_{y\approx 0}. \tag{3.45}$$

Additional progress comes from the zeroth order equation of the energy, which comes directly from the (2.15) if we take into account that in an ablation front the Mach number is $M_1^2 = v_1^2/\gamma(\gamma-1)\epsilon << 1$. This implies that $v_1^2/\epsilon << 1$ and that the (2.15) can be approximated as in equation (2.16):

$$Q_{T0} = \kappa_D \frac{d\epsilon}{dy} \approx \gamma\dot{m}(\epsilon - \epsilon_0).. \tag{3.46}$$

Now, we know from (3.45) that $\delta Q_T = k\xi Q_{T0}$, where we have taken into account that for $y > 0$ the medium is isothermal and then it is $\kappa_{D1}k/\dot{m} = kL_1 >> 1$, $L_1 = (1/\epsilon_1) \times (d\epsilon/dy)_{y=0^+}$. Using equation (3.46) we get

$$\frac{\delta\dot{m}}{\dot{m}} \approx \frac{\delta Q_T}{Q_{T0}} \approx k\xi, \tag{3.47}$$

and consequently, the surface tensionlike force is

$$\delta\dot{m}(v_1 + v_2) \approx k\xi\dot{m}(v_1 + v_2). \tag{3.48}$$

Introducing the new expression for the tensionlike force into equation (3.43) we get the following equation of motion for the evolution of the interface:

$$\ddot{\xi} = \frac{\rho_1 + \rho_2}{\rho_1 - \rho_2} kg\xi - \frac{4k\dot{m}}{\rho_1 + \rho_2}\dot{\xi} - \frac{k^2\dot{m}(v_1 + v_2)}{\rho_1 + \rho_2}\xi. \tag{3.49}$$

By substituting $\xi \sim e^{\sigma t}$, we get the equation for the instability growth rate

$$\sigma^2 + \frac{4kv_2}{1+r_D}\sigma + kg\left(\frac{kv_2^2}{gr_D} - A_T\right) = 0, \tag{3.50}$$

where $A_T = (1-r_D)/(1+r_D)$ is the Atwood number . This procedure shows that the surface tensionlike effect that leads to a cutoff wave number is caused by the thermal diffusion driving the ablation and that the damping term (the coefficient multiplying σ) is a consequence of the ablation process itself, independently of the means used to drive it. Solving the equation (3.50) , one can get the following expression for the dimensionless growth rate :

$$\frac{\sigma L_2}{v_2} = \sqrt{\left(\frac{2\kappa v_2}{1+r_D}\right)^2 - \frac{\kappa^2}{r_D} + \frac{\kappa A_T}{Fr_2}} - \frac{2\kappa}{1+r_D}, \quad \kappa = kL_2. \tag{3.51}$$

were kL_2 is the dimensionless wave number and we have introduced as a new parameter the Froude number $Fr^2 = v_2^2/gL_2$. By setting the condition that the characteristic length be of the order of k^{-1}:

$$y = \frac{1}{k}, \rho_1 = \rho(k^{-1}) \rightarrow \frac{\rho_2}{\rho_1} = \frac{1}{r_D}, \tag{3.52}$$

the development (2.20) provides us the expression for r_D:

$$\frac{1}{kL_2} \approx \frac{2}{5}\left(\frac{1}{r_D^{5/2}} - 1\right) + \frac{2}{3}\left(\frac{1}{r_D^{3/2}} - 1\right) + 2\left(\frac{1}{r_D^{1/2}} - 1\right) \tag{3.53}$$

$$\rightarrow r_D \approx \left(\frac{2kL_2}{5}\right)^{2/5} \text{for } r_D << 1\,(A_T \approx 1). \tag{3.54}$$

3.2.2 RTI in ablation fronts driven by ion beams

By setting $\delta E \sim ke^{-y}$ in equation (2.22) , we get the following equation for the energy flux perturbation Q_b:

$$\frac{\delta Q_b}{Q_b} = \frac{\delta E}{E} \approx -\frac{1}{kL_1}\frac{\delta\rho}{\rho}, \tag{3.55}$$

where $L_1 = \epsilon_1/(d\epsilon/dy)_{y=0^+} = \alpha E_1^2/\rho_1\psi(w_0)$, $E_1 = \gamma\dot{m}\epsilon_1/\mu_b$ (see equation (2.27). Then, taking into account that the front is an isotherm (3.44) and remembering (3.41), we have:

$$\frac{\delta\rho}{\rho} = \frac{\delta p}{p} - \frac{\delta\epsilon}{\epsilon} = \frac{\xi}{h} + \frac{\xi}{\epsilon}\frac{d\epsilon}{dy}. \tag{3.56}$$

Equations (2.27), (3.55) and (3.56) yield

$$\frac{\delta\dot{m}}{\dot{m}} \approx \frac{\delta Q_b}{Q_b} \approx \frac{k\xi}{kL_1}\left(\frac{1}{kh}+\frac{1}{kL_1}\right). \tag{3.57}$$

Since $kh << 1$ and in the isothermal region ($y > 0$) it is also $kL_1 >> 1$, it turns out from equation (3.57) that $\delta m/\dot{m} << k\xi$ and the surface tensionlike force in equation (3.43) becomes negligible. Thus, the equation of motion at the interface reads

$$\ddot{\xi} = \frac{\rho_1+\rho_2}{\rho_2-\rho_1}kg\xi - \frac{4k\dot{m}}{\rho_1+\rho_2}\dot{\xi}. \tag{3.58}$$

By taking $\xi \sim e^{\sigma t}$ we get the following equation for the instability growth rate σ:

$$\sigma^2 + \frac{4kv_2}{1+r_D}\sigma - A_T kg = 0, \tag{3.59}$$

where r_D is obtained from equation (2.31) by using the condition (3.52) :

$$\frac{1}{kL_2} \approx \frac{1}{6}+\frac{1}{3}\left(\frac{\rho_2}{\rho}\right)^3 - \frac{1}{2}\left(\frac{\rho_2}{\rho}\right)^2, \rightarrow r_D \approx \left(\frac{kL_2}{3}\right)^{1/3} \text{for}\, r_D << 1 (A_T \approx 1). \tag{3.60}$$

Once the expression for r_D is specified , we can get the dimensionless growth rate $\frac{\sigma L_2}{v_2}$ as a function of the dimensionless wave number with the Froude number as a parameter:

$$\frac{\sigma L_2}{v_2} = \sqrt{\frac{A_T\kappa}{\mathrm{Fr}_2} + \left(\frac{2\kappa}{1+r_D}\right)^2} - \frac{2\kappa}{1+r_D};\ \kappa = kL_2. \tag{3.61}$$

The dimensionless growth rate is presented in fig.3.2 as a function of the dimensionless wave number κ in a logarithmic scale for Fr_2=1,10,100. In fig.**??** we show the growth rate in a linear scale for Fr_2=1,2,3.

From these graphs we can see that the growth rate achieves a maximum value σ_m for a wave number k_m that depends on the Froude number and then it decreases asymptotically for large values of k. The absence of a diffusive process of energy transport prevents the existence of a surface tensionlike force and no cutoff wave number is observed. However, a stabilizing viscouslike effect is generated by the ablation process itself, so that there is a growth rate reduction in comparison with the classical case. In fig.3.4 we represent the maximum dimensionless growth rate and the corresponding dimensionless wave number as a function of the Froude number. It is evident that the maximum growth rate decreases almost linearly with the ablation velocity v_2.
In general, it can be assumed that in an ion beam driven ablation front the total

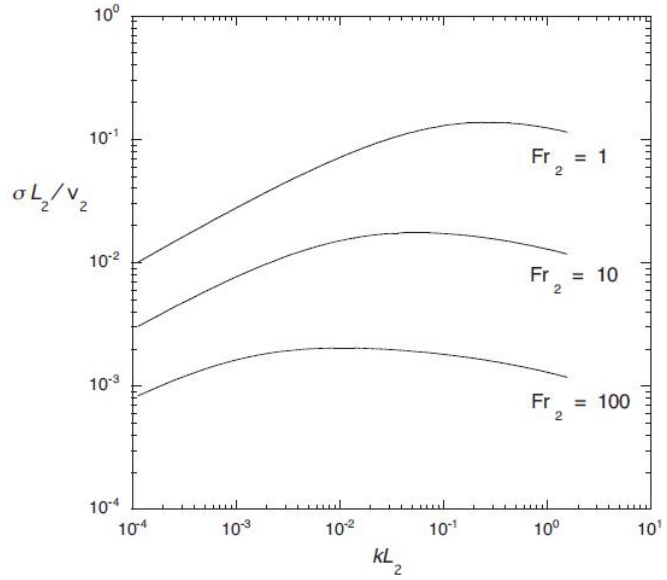

Figure 3.2: Dimensionless growth rate for an ion beam driven ablation front (1) - Dimensionless growth rate number $\frac{\sigma L_2}{v_2}$ as a function of the dimensionless wave number kL_2 for different Froude numbers Fr_2=1,10,100. (source: Piriz, 2009 (17)).

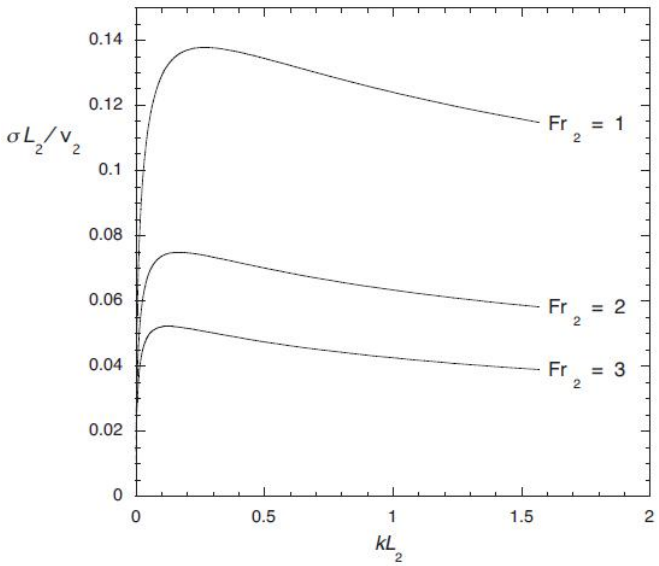

Figure 3.3: Dimensionless growth rate for an ion beam driven ablation front (2) - Dimensionless growth rate number $\frac{\sigma L_2}{v_2}$ as a function of the dimensionless wave number kL_2 for different Froude numbers Fr_2=1,2,3. (source: Piriz, 2009 (17)).

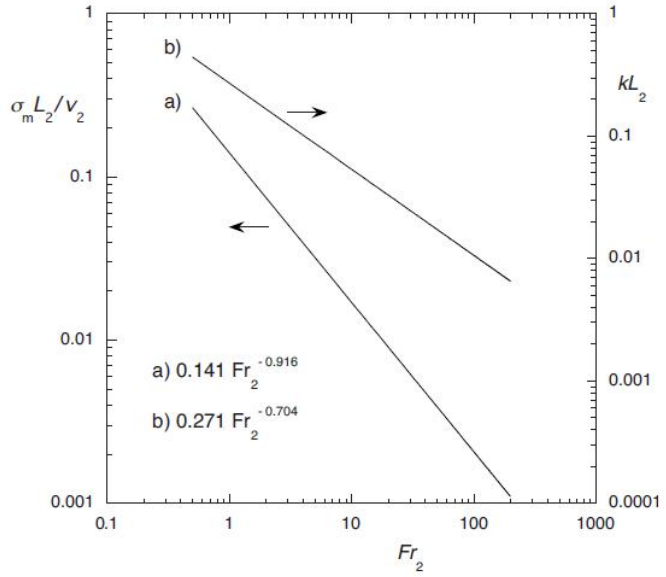

Figure 3.4: Maximum dimensionless growth rate for an ion beam driven ablation front - Maximum dimensionless growth rate $\frac{\sigma L_2}{v_2}$ and wave number $k_m L_2$ as a function of the Froude numbers Fr_2=1,2,3. (source: Piriz, 2009 (17)).

energy flux deposited into the ablative corona can be transported by means of collisional deposition and thermal conduction. By allowing that some part Q_T of the beam energy flux be transported by thermal conduction so that $\phi_0 = Q_T/(Q_T + Q_b)$, we can write for the perturbation in the mass ablation rate a more general expression,

$$\frac{\delta\dot{m}}{\dot{m}} \approx \frac{\delta Q_T}{Q_{T0}} \approx \phi_0 k\xi. \tag{3.62}$$

and consequently we get

$$\delta\dot{m}(v_1 + v_2) \approx \Phi_0 k\xi\dot{m}(v_1 + v_2). \tag{3.63}$$

Of course, if some fraction ϕ_0 of the energy flux is transported by thermal conduction,in principle the density profile expressed by equation (3.60) is not valid any more. However, it can be easily noticed that the result in (3.60) is only slightly different with respect to the case of a corona driven purely by thermal conduction ablation, for which in the same limit of $r_D << 1$, we would get $r_D \approx (5kL_2/2)^{2/5}$. Therefore, we can expect that in a general case for which both mechanisms, thermal conduction and collisional beam deposition, are present, the equation (3.60) will still represent a good

approximation to the density jump r_D.

Introducing the expression (3.62) into equation (3.43), we obtain the following equation of motion for the interface:

$$\ddot{\xi} + \frac{4kv_2}{1+r_D}\dot{\xi} + \left[\phi_0 \frac{k^2 v_2^2}{r_D} A_T kg\right]\xi = 0, \tag{3.64}$$

In this case we also recover the presence of a cutoff wave number k_c, whose expression can be found solving equation (3.64) for $\sigma = 0$:

$$k_c = \frac{g r_D (1-r_D)}{\Phi_0 v_2^2 (1+r_D)}. \tag{3.65}$$

We notice that k_c can become very large if the fraction Φ_0 of the energy flux transported by thermal diffusion gets small. Also, it is important to stress that this last result is quite general, due to the fact that setting $\psi(w) \approx \psi(w_0)$ in equation (3.55) we take into account both the cases in which $v_b > v_{the}$ and $v_b \leq v_{the}$. Actually, the treatment above is not altered moving from one situation to another, provided that we substitute the right expression for $\psi(w)$. The only difference between the two cases is that when $v_b \leq v_{the}$, the quantity L_2 becomes even larger and the density gradient may become somewhat smoother over a distance of the order k^{-1} from the ablation front.

4

Dynamic stabilization of Rayleigh-Taylor instability in an ablation front

4.1 Introduction

In this section the problem of dynamic stabilization of Rayleigh-Taylor instability in the acceleration phase of the compression will be addressed. We have already seen in the introduction the role of RTI in determining the size of the target, by setting an upper limit to the in-flight aspect ratio; as ignition velocities are in the range of $3 - 4 \times 10^7$ cm/s for megajoule scale lasers, the minimum amount of energy which is necessary for achieving ignition is determined by the mass, therefore thinner shell targets allow reducing the imput energy. Thus, any method for stabilizing ablation fronts in ICF is of interest: the one that will be proposed here is based on the already known mechanism of dynamic stabilization, whose effectiveness has been already demostrated in various problems in mechanics and electrodynamics. In general, it consists in applying an external periodic driving force to a physical system which shows instability, and it has been proven that by choosing the suitable values of amplitude and frequency for the periodic modulation it is possible to mitigate the instability itself.

The first proposal for such a method for stabilizing the inverted pendulum dates back to 1908, when Stephenson (26) pointed out how from the study of the equation of motion (which in this case is a *Mathieu equation*) it was possible to demonstrate

that an inverted pendulum (namely, a pendulum whose mass is above the pivot point) can be maintained around its position, otherwise unstable, by a periodic variation in spring of sufficiently large frequency. This behaviour was later discussed and investigated experimentally by Kapitza in 1951 (27), and today we know that not only an inverted pendulum which undergoes vibrations of large enough amplitude and/or frequency shows no tendency to turn down, but also that at small and moderate deviations from the vertical the pendulum tends to return to it. After that, many papers dealing with the analysis of the properties of this system have been written, also due to its importance in various fields of the physics, among which the theory of solitons , quantum optics and weak superconductivity.

An analogue mechanism provides the stabilization of the motion of charged particles in the Paul's trap. The latter is a quadrupole radio-frequency trap in which the particles are suspended in dynamic equilibrium by setting electrode configurations which give sinusoidally time varying forces whose strenghts are proportional to the distance from a central origin. In such conditions, the ions experience a restoring force which drives them back to the center of the trap and their motion is described by the solution of the corresponding Mathieu equations. It was proven that, provided that the frequency and amplitude of the varying forces are large enough, it is possible to maintain the particles steady at the center (28).

In 1969 Wolf (29) demonstrated from an experimental point of view the possibility of dynamically stabilizing the Rayleigh-Taylor instability of the interface between two Newtonian fluids by submitting the latter to a vertical sinusoidal motion, under certain conditions for the angular frequency and amplitude of the oscillations. Later, Troyon and Gruber (30) gave a theoretical explanation for the results obtained by Wolf, and showed the importance of both viscosity and surface tension in determining the regions of the parameters space for which stabilization can be achieved. However, the analytical method they applied to the Mathieu equation of motion for finding the region of stability led to solutions from which it is very difficult to extract relationships which could serve as scaling laws for designing experiments. Thus it was found at the same time that a minimum value of the surface tension is also necessary for achieving stabilization and that for some values of the coefficients of the Mathieu equation the surface tension can reduce the stabilizing effect of the driving oscillation.

Dynamic stabilization by vertical vibration of an ablation front in ICF was first proposed by Boris in 1977 (31),in the context of laser driven pellet implosions. He showed by means of 2D numerical simulations that if the laser beams are modulated in intensity so that the ablation layer is subject to a sufficiently rapid and strong oscillating acceleration, then a substantial band of the Rayleigh-Taylor instability wave number spectrum can be stabilized by this oscillation. However, he was not able to give a complete physical picture of the basic mechanism of the phenomenon, since at that time the essential physics of the linear phase of ablative RTI was not yet well understood. Actually, he did not derive the equation for the evolution of the perturbation amplitude from a consistent theory, but instead he had to use a phenomenological version in which the damping effects of the ablation are not present. In this thesis it will be shown that in reality they are crucial for the stabilization of the ablation front.
In 1993 Betti *et al.* (32) studied again this problem by means of a simplified sharp boundary model with continuity of the mass flow and the pressure balance at the interface as boundary conditions. However, as it happened for Boris, a theoretical treatment of the linear stage of ablative RTI was not yet available and Betti et al. used a Takabe-like formula (see 3.8) for the instability growth rate. Such an approach, in opposition to the one of Boris, led to an overestimation of the magnitude of the damping effect, producing rather optimistic results.

In 2010 Piriz et al. (21) proposed a new analysis of the dynamic stabilization of an interface between two inmiscible and incompressible Newtonian fluids, based on Newton second law, that allowed for the consideration of a time-varying interface. In practice equation 3.34 is recovered and a periodic perturbation is added to the background acceleration g, then a new dispersion relation is found, whose solutions are analytic and give the upper and lower limits of the stability region. The periodic vertical excitations were chosen to consist in a periodic sequence of Dirac deltas, whereas all the previous works both related to fluids and plasmas used a sinusoidal vibration. It was found that for symmetric Dirac deltas the qualitative results do not differ significantly from the ones obtained by Troyon and Gruber in the case of a sequence of sine waves. However, this new analysis allowed to clarify the role of viscosity and surface tension by expressing the minimum frequency required for obtaining dynamical stabilization in terms of both these quantities. Also, it was possible to find dimensionless combinations of the

physical parameters governing the problem, namely the ratio between the amplitude of the perturbation acceleration and the background acceleration g, the dimensionless frequency of the perturbation and the dimensionless minimum wave number that it is possible to stabilize. In this way scaling laws which can be used for experiments were provided. Moreover, it was shown that in the case of a symmetrical driving surface tension effects are necessary in order to get dynamic stabilization of the interface.
The case of RTI in Newtonian fluids presents some analogies with the same one in ablation fronts, because RTI in ablation fronts shows analogous effects to viscosity and surface tension. However, the different dependence of the damping and surface tensionlike effects on the perturbation wavenumber preclude a direct extrapolation of the results obtained for Newtonian fluids. Furthermore, in an ablation front the compressibility effects (absent in Newtonian fluids) play a crucial role. In this chapter a specific study of dynamic stabilization of ablation fronts will be addressed, using the simplest possible modulation, that is, a sequence of Dirac deltas. It has been demonstrated (21) that such an approach allows us to capture the essential physics of the RTI dynamic stabilization, and besides allows for finding the general similarity parameters that are actually independent of the particular form of modulation used. Finally, it can serve as a basis for a general comparison between the performance of different drivings which will be shown in the next chapter.

4.2 Dynamic stabilization of Rayleigh-Taylor instability in ablation front by means of sequences of Dirac deltas

We consider an ablation front driven by ion beams as discussed in subsection (3.2.2). For our purpose of studying dynamic stabilization, we recover the equation of motion (3.64) and add to the constant background gravity acceleration g a periodic modulation $\Gamma(\omega t)$ that oscillates with a frequency ω and an amplitude A:

$$\ddot{\xi} + \frac{4kv_2}{1+r_D}\dot{\xi} + \left[\phi_0 \frac{k^2 v_2^2}{r_D} - A_T k G(t)\right]\xi = 0, G(t) = g + b\Gamma(\omega t); \qquad b = \omega^2 A. \tag{4.1}$$

Then, we consider an oscillatory acceleration modulation consisting in a sequence of positive and negative Dirac deltas $\delta(\tau)$ with amplitudes $A_1 = b_1/\omega^2$ and $A_2 = b_2/\omega^2$ respectively:

$$\Gamma(\omega t) = b_1 \delta(\omega t - 2m\pi) - b_2 \delta[\omega t - (2m+1)\pi], \tag{4.2}$$

where m is an integer. Now, we introduce the following dimensionless variables

$$\tau = \omega t;\ x = \xi/\xi_0, \tag{4.3}$$

where ξ_0 is the initial perturbation amplitude (at $t = 0$). Substituting the new variables in (4.1) and dividing by ξ_0, we find:

$$\omega^2\ddot{x} + \frac{4kv_2}{1+r_D}\omega\dot{x} + \left[\frac{\phi_0 k^2 v_2^2}{r_D} - A_T kg - A_T k\omega^2 A\Gamma(\tau)\right]x = 0. \tag{4.4}$$

Then we introduce the new quantities:

$$D = \frac{2kv_2}{(1+r_D)\omega}; \tag{4.5}$$

$$K^2 = \frac{\phi_0 k^2 v_2^2}{\omega^2 r_D} - \frac{A_T kg}{\omega^2}; \tag{4.6}$$

$$\beta_1 = A_T k A_1; \tag{4.7}$$

$$\beta_2 = A_T k A_2. \tag{4.8}$$

Now, we can use the assumptions made in chapter 3 for the discontinuity jump (see equation (3.60)), namely that $r_D << 1$ and $A_T \approx 1$ and so we get $D = \frac{2kv_2}{\omega}$, $\beta_1 = kA_1, \beta_2 = kA_2$. Using these new definitions, equation (4.1) becomes a Hill equation:

$$\ddot{x} + 2D\dot{x} + [K^2 - \beta\Gamma(\tau)]x = 0, \tag{4.9}$$

$$\beta\Gamma(\tau) = \beta_1\delta(\tau - 2m\pi) - \beta_2\delta[\tau - 2m\pi]. \tag{4.10}$$

By further introducing the dimensionless variables

$$\kappa = \frac{kv_2^2}{g},\ \varpi = \frac{\omega v_2}{g}, \tag{4.11}$$

the density jump expressed by equation (3.60) reads as

$$r_d \approx \frac{\kappa^{1/3}}{3\mathrm{Fr}_2^{1/3}},\ \mathrm{Fr}_2 = \frac{v_2^2}{gL_2}, \tag{4.12}$$

where Fr_2 is the Froude number and is the characteristic parameter of the steady ablation front. In the same manner, the coefficients of equation (4.9) can be expressed in terms of the new variables as follows:

$$D = \frac{2\kappa}{\varpi},\ K^2 = \frac{\kappa}{\varpi}\left[\left(\frac{\kappa}{\kappa_c}\right)^{2/3} - 1\right], \tag{4.13}$$

$$\kappa_c = \frac{r_D(k_c)}{\phi_0} \approx \frac{1}{\phi_0^{3/2}(3\mathrm{Fr}_2)^{1/2}}, \tag{4.14}$$

$$\beta_1 = \frac{k}{\varpi^2}\frac{b_1}{g}, \beta_2 = \frac{k}{\varpi^2}\frac{b_2}{g} \tag{4.15}$$

Equation (4.14) is the dimensionless expression for the natural cutoff wave number of the nonoscillating ablation front already found in (3.65).It is important to notice that in terms of the new variables, κ_c is a function of the Froude number Fr_2 and of the fraction ϕ_0 of the energy flux that is transported by thermal diffusion, in such a way that it becomes larger when ϕ_0 becomes smaller. Now, we perform the usual variable change $y = x\exp(D\tau)$ and so we get:

$$\ddot{y} + [K^2 - D^2 - \beta\Gamma(\tau)]y = 0. \tag{4.16}$$

According ot the Floquet theory (33), the solutions of (4.16) have the general form

$$x(\tau) = P(\tau)e^{\sigma\tau}, \sigma = \frac{\gamma}{\omega}, \tag{4.17}$$

where $P(\tau)$ is a periodic function and γ is the instability growth rate. In addition, these solutions have the general property of translational symmetry:

$$x(\tau + 2\pi) = \chi x(\tau) \text{ or } y(\tau + 2\pi) = e^{2\pi D}y(\tau), \tag{4.18}$$

$$\chi e^{2\pi D} = e^{i2\pi\eta} = e^{\pm im\pi + 2\pi(\sigma + D)}. \tag{4.19}$$

Here, η is the so-called characteristic exponent which in general depends on the quantities $K^2 - D^2$ and β. For the case of marginal stability it turns out that $\sigma = 0$.

4.2.1 The case of symmetric Dirac deltas driving (SD)

We consider here the case of a symmetric driving in which $\beta_1 = \beta_2 = \beta = (\kappa/\varpi^2)(b/g)$ (see fig.4.1). Equation (4.16) is a dimensionless Hill equation which can be easily solved in the regions where $\Gamma(\tau) = 0$. These solutions can be written as:

$$y_1 = c_1 \cos\tau\sqrt{K^2 - D^2} + c_2 \sin\tau\sqrt{K^2 - D^2},\ -\pi < \tau < 0; \tag{4.20}$$

$$y_1 = c_3 \cos\tau\sqrt{K^2 - D^2} + c_4 \sin\tau\sqrt{K^2 - D^2},\ 0 < \tau < \pi, \tag{4.21}$$

By using the periodic condition for the solutions:

$$y_3(\tau + 2\pi) = e^{i2\pi\eta y_1(\tau)}, \tag{4.22}$$

and by integration of equation (4.16):

$$\int_{-\epsilon}^{+\epsilon} d\dot{y} = \int_{-\epsilon}^{+\epsilon} b\Gamma(\tau)y(\tau)d\tau. \tag{4.23}$$

we can state the following matching conditions for the solutions:

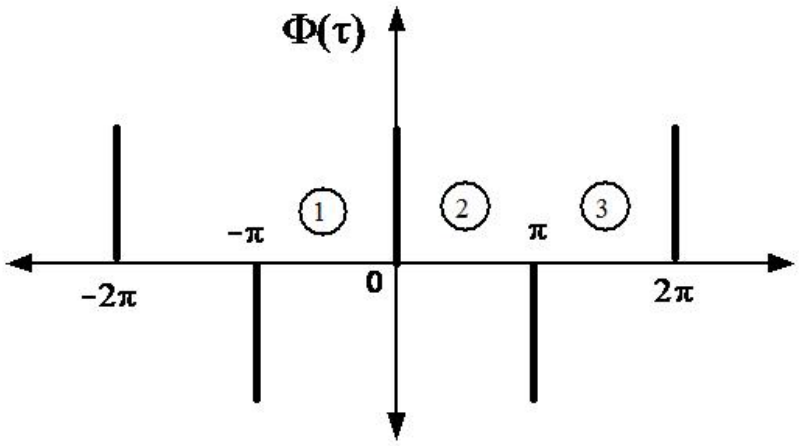

Figure 4.1: Dirac delta waves - Symmetric Dirac delta wave oscillation.

1. $y_1(0) = y_2(0)$;
2. $y_2(\pi) = y_3(\pi) = e^{i2\pi\nu} y_1(-\pi)$;
3. $\dot{y_1}(0) - \dot{y_2}(0) = -\beta_1 y_1(0)$;
4. $\dot{y_2}(0) - \dot{y_3}(0) = \beta_2 y_2(\pi) = \beta_2 e^{i2\pi\nu} y_1(-\pi)$.

which can be converted in equations whose unknowns are the integration constants $c_i (i = 1, 2, 3, 4)$:

1. $c_1 = c_3$;
2. $c_3 \cos\lambda\pi + c_4 \sin\lambda\pi = e^{i2\pi\nu}(c_1 \cos\lambda\pi - c_2 \sin\lambda\pi)$;
3. $c_2 = -\frac{\beta_1}{\lambda} c_3 + c_4$;
4. $-c_3\lambda \sin\lambda\pi + c_4\lambda \sin\lambda\pi - e^{i2\pi\nu}\pi(c_1 \sin\lambda\pi + c_2 \cos\lambda\pi) = \beta e^{i2\pi\nu}(c_1 \cos\lambda\pi - c_2 \sin\lambda\pi)$.

After some algebra, we get the following dispersion relation:

$$\cos 2\pi\nu = \cos 2\pi\lambda - \left(\frac{\beta}{2\lambda}\right)^2 (1 - \cos 2\lambda\pi), \tag{4.24}$$

that is

$$\beta^2 = 4(K^2 - D^2)\frac{\cos 2\pi\sqrt{K^2 - D^2} - \cos 2\pi\eta}{1 - \cos 2\pi\sqrt{K^2 - D^2}}. \tag{4.25}$$

Taking into account (4.19), we have

$$\cos 2\pi\eta = \pm \cosh 2\pi(\sigma + D). \tag{4.26}$$

Then we can also use the expressions (4.13) and (4.15) and rewrite equation (4.25) as

$$\frac{b}{g} = 4\bar{\omega}\left[\left(1 - \frac{K^2}{D^2}\right)\frac{\cosh 2\pi D\sqrt{1 - K^2/D^2} \pm \cosh 2\pi(\sigma + D)}{\cosh 2\pi D\sqrt{1 - K^2/D^2} - 1}\right]^{1/2} \tag{4.27}$$

$$D = \frac{2\kappa}{\varpi},\ \frac{K^2}{D^2} = \frac{(\kappa/\kappa_c)^{2/3} - 1}{4\kappa}, \tag{4.28}$$

where we have put $\cos 2\pi\sqrt{K^2 - D^2} = \cosh 2\pi\sqrt{D^2 - K^2}$. By setting $\sigma = 0$ in equation (4.27), we obtain two curves for b/g as a function of the variables in equation (4.28), namely $b/g)_{\pm} = f(\kappa)$ with κ_c and ϖ as parameters. The solutions with the plus and minus sign denote, respectively, the upper and lower limit of the stability region.
The first thing that can be noticed from equations (4.27) and (4.28) is that the damping term D is essential for making dynamic stabilization possible and in the case it is absent, like in the problem originally considered by Boris (31), only a narrow range of wavenumbers can be stabilized. In fact, setting $D = 0$ equation (4.27) becomes

$$\frac{b}{g} \approx 4\bar{\omega}\left(\frac{\cosh 2\pi K \pm 1}{\cosh 2\pi K - 1}\right)^{1/2}. \tag{4.29}$$

It is easy to see that now the new limits of marginal stability are given by the curves of b/g whose intersection with the axis of the dimensionless wave number are respectively κ_c and the value κ_0 corresponding to the solution of the equation $2\pi K(\kappa_0) = \pi$, that is $(4\kappa_0/\varpi^2)[(\kappa_0/\kappa_c)^{2/3} - 1] = 1$. This means that only the wave numbers which are in the interval between these two values can be stabilized for $b/g << 1$, as in figure 4.2. Moreover, the interval of the stable wave numbers becomes even narrower with larger b/g. This is an analogue result to the one obtained for dynamic stabilization of Newtonian fluids by Piriz et al. (21).

In general, for $D \neq 0$, the upper ("+") and lower ("-") limits are like the ones shown in fig. 4.3 for two typical cases :$\kappa_c = 0.3, \varpi = 0.8$ and $\kappa_c = 1, \varpi = 0.5$.

Apart from the qualitative view shown in the picture, it is interesting to calculate the mathematical behaviour of the two curves. For this purpose, we examine the limits of the (4.27) for $\kappa << 1$ and $\kappa >> 1$,that is $\beta \to 0$ and $\beta \to \infty$ for the (4.25) . In the case of the upper ("+") curve, we have that for $\kappa >> 1$ equation the sines and cosines

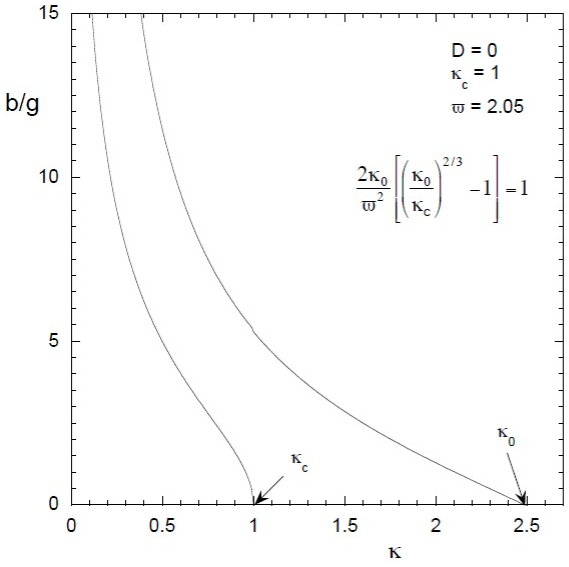

Figure 4.2: Stability region for a zero damping - Dimensionless driving acceleration b/g for marginal stability as a function of the dimensionless wave number κ for the case $D = 0$. The upper and lower limits of the region of stability are shown for $\kappa_c = 1$ and $\varpi = 2.05$.

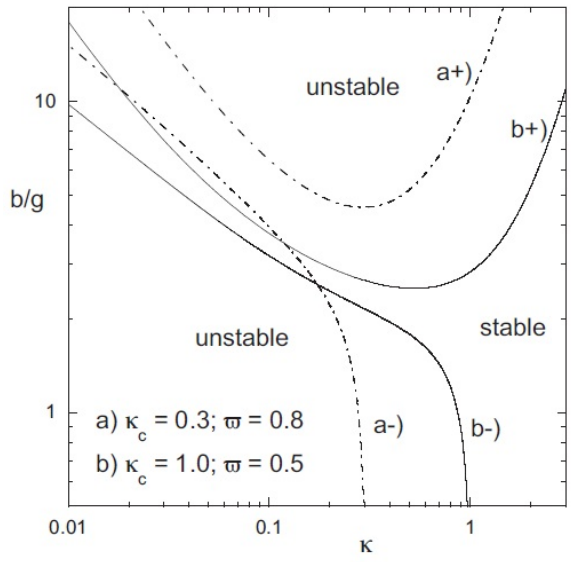

Figure 4.3: Stability region for SD (1) - Dimensionless driving acceleration b/g for marginal stability as a function of the dimensionless wave number κ for $\kappa_c = 0.3, \varpi = 0.8$ and $\kappa_c = 1, \varpi = 0.5$. The upper and lower limits of the region of stability are denoted by the symbols "+" and "-", respectively.

in (4.25) can be transformed into the corresponding hyperbolic functions which in turn become very large, so that the 1 in the denominator becomes negligible . In this limit we also have that

$$\frac{K^2}{D^2} = \frac{(\kappa/\kappa_c)^{2/3} - 1}{4\kappa} \xrightarrow[\kappa\to\infty]{} 0, \tag{4.30}$$

and using the exponential development $\cosh x = (e^x + e^{-x})/2$ we get

$$\frac{b}{g} \approx 4\varpi[1 + e^{(\pi/2\varpi)[(\kappa/\kappa_c)^{2/3}-1]}]^{1/2},\ (\kappa >> 1). \tag{4.31}$$

Equation (4.31) describes the behaviour of the upper curve beyond the minimum, as shown qualitatively in fig. 4.3. The behaviour before the minimum can be found by calculating the limit of (4.27) for $\kappa << 1$. In this case $D^2/K^2 \to 0$ and the Taylor series development for the cosine and hyperbolic cosine can be applied to get

$$\frac{b}{g}\Big)_+ \approx \frac{2}{\pi}\frac{\varpi}{k},\ (\kappa << 1). \tag{4.32}$$

This means that dynamic stabilization is possible only for values of b/g below the minimum of the upper limit, which is the upper limit of stability.
For the lower curve, in the case of $\kappa << 1$, we find that

$$\frac{b}{g}\Big)_- \approx \frac{2\omega}{k},\ (\kappa << 1). \tag{4.33}$$

The limit for the lower curve for the case of $\beta \to \infty$, which in reality corresponds to $\kappa \to \kappa_c$, can be found by means of an analogous derivation to the one developed for (4.31) and reads as

$$\frac{b}{g} \approx 4\varpi[1 - e^{(\pi/2\varpi)[(\kappa/\kappa_c)^{2/3}-1]}]^{1/2},\ (\kappa \to \kappa_c). \tag{4.34}$$

For each wave number κ_m such that $\kappa_m < \kappa_c$, the corresponding intersection on the lower curve determines the minimum value $b/g)_{min}$ that is required in order to dynamically stabilize all the wavenumbers $\kappa \geq \kappa_m$. Such value of b/g is the lower boundary of stability. Clearly, in order to have a region of stability in the parameter space of the problem, it is necessary that $b/g)_{\min} < b/g)_{\max}$. To better represent the situation, we can construct stability charts of b/g as a function of ϖ that provide the stability regions for a given value of the parameter κ_c and for chosen values of the minimum wave number κ_m that we want to stabilize. In order to do that, we take the minimum value of the positive branch of equation (4.27) (with $\sigma = 0$) and represent it as a function of

ϖ for a given κ_c in order to find the upper boundary. For the lower boundary, instead, we set $\kappa = \kappa_m$ in the negative branch of equation (4.27) and again we represent it as a function of ϖ for a given κ_c . For each value of κ_m the intersection between the upper and lower boundary gives us the minimum values of b/g and ϖ that are necessary for dynamic stabilization.
Typical stability charts are shown in figs.4.4-4.6 for three different values of κ_c: $0.3, 1$ and ∞. These figures show the general behaviour: the smaller the minimum value κ_m of the wave numbers that we want to stabilize for a given value of the cut-off wave number κ_c, the larger the relative amplitude b/g and frequency ϖ that are requested for stabilization. In the same manner, the smaller κ_c, the more difficult to reduce κ_m to a given fraction of κ_c, thus requiring higher values of b/g and ϖ. It is important to notice that, as it is shown in fig.4.6 , even for the case $\kappa_c = \infty$, which corresponds to the case $\phi_0 = 0$, or absence of thermal conduction, in equation (4.1), it is still possbile to stabilize large wave numbers, although it turns out to be more difficult to stabilize lower desired wave numbers. This is in contrast with the results obtained for Newtonian fluids in the article (21), where it was found that it is not possible to stabilize the wave numbers which are larger than a given value of κ_m when surface tension (the analogous effect in fluids with respect to thermal conduction in ablated plasmas) is not present. We will see later that such a behaviour of dynamic stabilization of Rayleigh Taylor instability in ablation fronts is exclusive of the Dirac deltas driving and that for more general acceleration modulations it performs in a similar manner as in Newtonian fluids.

Obviously the possibility to stabilize all the wave numbers above a certain κ_m, hopefully as small as possible, is one of the main goals. However, it is also very important to reduce the maximum growth rate of the unstable modes. For this purpose, we calculate the dimensionless growth rate $\gamma(\gamma v_2/g = \sigma\varpi)$ as a function of κ for given values of κ_c and ϖ and for several values of b/g. The instability growth rate can be explicitly obtained from equation (4.27) by solving it for σ:

$$\sigma = \frac{1}{2\pi}\cosh^{-1}\left[\pm\left(1+\frac{q^2}{1-K^2/D^2}\right)\cosh 2\pi D\sqrt{1-K^2/D^2}+\frac{q^2}{1-K^2/D^2}\right]-D, \quad (4.35)$$

where $q = (b/g)(1/4\varpi)$. In principle, just looking at the stability charts one could imagine intuitively that by increasing the value of b/g above the upper boundary, in the region known as the one corresponding to parametric instabilities, the instability

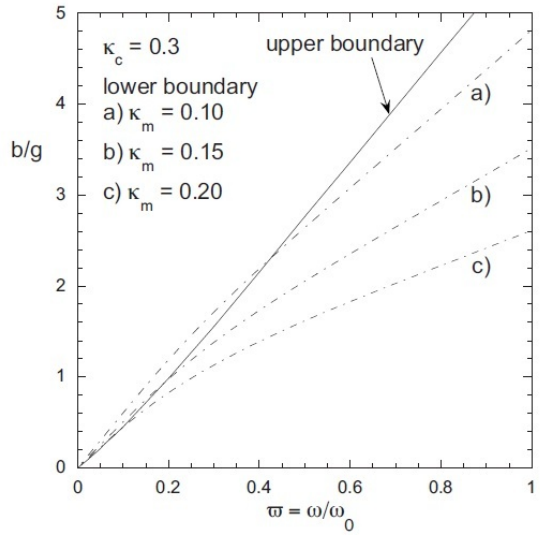

Figure 4.4: Stability chart for SD (1) - Stability region for $\kappa_c = 0.3$. The lower boundary is given for $\kappa_m = 0.10, 0.15$ and 0.20.

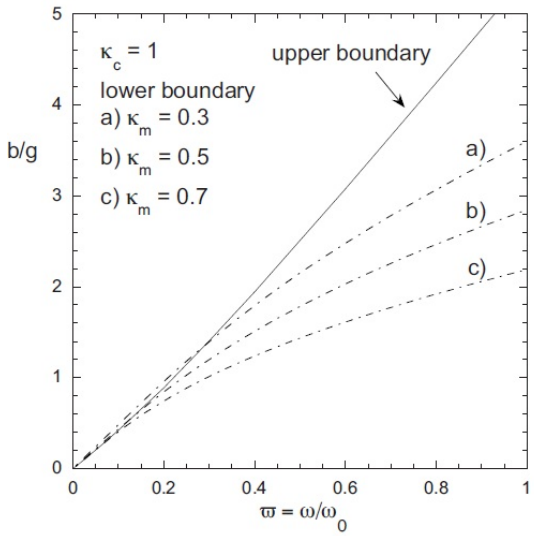

Figure 4.5: Stability chart for SD (2) - Stability region for $\kappa_c = 1$. The lower boundary is given for $\kappa_m = 0.3, 0.5$ and 0.7.

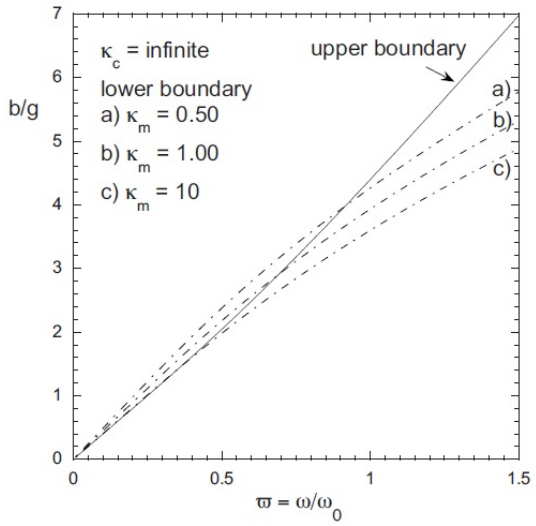

Figure 4.6: Stability chart for SD (3) - Stability region for $\kappa_c = 0.3$. The lower boundary is given for $\kappa_m = 0.50, 1$ and 10.

growth rate could be lower that in the reference case. It is possible to see from the graphs of the growth rate for different b/g that this is not exactly true. In fig. 4.7 we show the instability growth rate for $\varpi = 0.6$, $\kappa_c = 0.3$ and $b/g = 0, 2.4, 4.5$. We observe that, with respect to the refence case of the nonoscillating front ($b/g = 0$), increasing b/g until 2.4 we remain below the upper limit (see fig.4.8) and the dynamic cut-off wave number is reduced to $\kappa_m = 0.15$, while the maximum growthr ate is reduced from $\sigma_{\max} = 0.112$ to $\sigma_{\max} = 0.096$ [curve(b)].When $b/g = 4.5$,we are below the lower limit if $\kappa_m \leq \kappa_{m2}$ and the maximum growth rate in this region results to be further lowered to $\sigma_{\max} = 0.075$; however, for $\kappa_{m3} \leq \kappa_m \leq \kappa_{m4}$, we are again in the region of parametric instabilities and, in such a region, not only the range of unstable wave numbers is wider ($\Delta\kappa_m = \kappa_{m4} - \kappa_{m3}$) but also the maximum growth rate has increased to a value close to the reference case: $\sigma_{\max} = 0.104$. Therefore, the better strategy is to remain inside the stability region defined by the parametric instabilities in the upper boundary and by the minimum wave number κ_m above which we want to stabilize in the lower boundary.

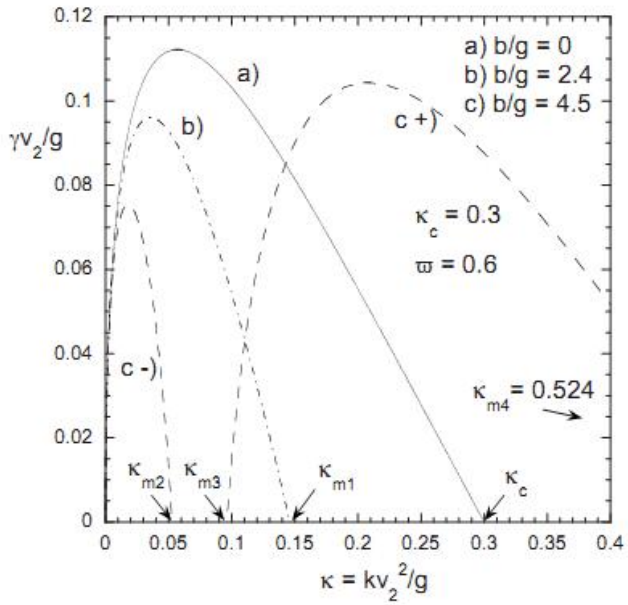

Figure 4.7: Instability growth rates for SD - Instability growth rate for $\kappa_c = 0.3$ and a fixed dimensionless frequency ϖ for different values of the dimensionless driving acceleration b/g.

4.2.2 Compressibility effects

The results shown by stability charts 4.4-4.5 are in agreement with the ones already found for Newtonian fluids in (21) for what concerns the necessity of going at relatively large values of b/g in order to achieve stabilization. To allow the existence of such large oscillations in the unablated material ahead the front we have to consider the presence of compressibility effects in the plasma. This fact has been already noticed by Boris (31))and Betti (34): the ablation pressure itself can push the ablation front but is unabe to pull it, so compressibility effects are the only responsible for the creation of local accelerations b that are considerably larger than the background acceleration g affecting the whole mass of the accelerated shell. In this way, an oscillating cycle that makes dynamic stabilization work is generated.

The details of the process for which large values of b/g can be achieved in an ablation front and the thickness of the region affected by the vibration should be investigated by means of one dimensional numerical simulations. Here we will consider such compressibility effects in a phenomenological manner in order to understand what new

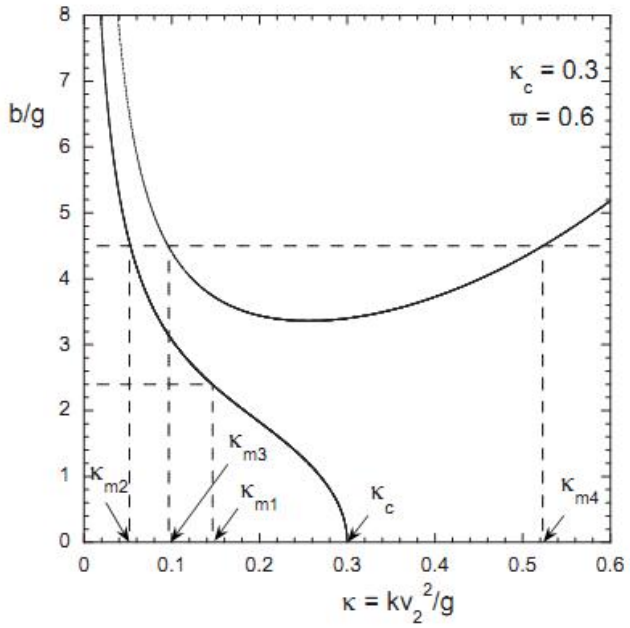

Figure 4.8: Stability region for SD (2) - Upper and lower limits given by dimensionless driving acceleration b/g from equation (4.27) as function of the dimensionless wave number κ for $\kappa_c = 0.3, \varpi = 0.6$. The wave numbers $\kappa_{mi} (i = 1, 2, 3)$ correspon to the cut-off values of fig. (4.7).

constraints they impose on the stabiltiy region.

The first consequence of taking into account compressibility effects is that the minimum wave number $k_m = 2\pi/\lambda_m$ above which the front is dynamically stabilized cannot be freely chosen any more, but will depend on the oscillation frequency ω. In fact the thickness of the shell region affected by the oscillation is equal to the distance that can be covered by the sound waves, that is, if they travel with velocity c_{s2} during an oscillation characteristic time $T = 2\pi/\omega$, we have that

$$\lambda_m \approx \Delta y = c_{s2}T,\ k_m^{-1} \approx c_{s2}\omega^{-1}. \tag{4.36}$$

using the dimensionless variables defined in (4.11), the condition above becomes

$$\kappa_m \approx M_2\varpi \tag{4.37}$$

where $M_2 = v_2/c_{s2}$ is the Mach number in the relatively dense and cold material ahead the ablation front. Equation (4.37) shows that the larger is the frequency ϖ, the larger will be the minimum wave number κ_m, thus suggesting that too large frequencies may not stabilize sufficiently small wave numbers.

On the other hand, the phenomenological calculation for the local acceleration b shows that large frequencies are necessary to produce large local accelerations b. It has been suggested by Betti (32) and confirmed by preliminary one dimensional simulations that when a pressure modulation $\Delta p/p$ is imposed on the front , an average acceleration b is developed on a region of thickness Δy beneath the ablation front that can be estimated by the following expression

$$b \approx \frac{\Delta p}{\rho_2 \Delta y} \Rightarrow \frac{b}{g} \approx \frac{\Delta p}{p}\frac{d}{\Delta y}, \tag{4.38}$$

where $p = \rho_2 g d$ is the ablation pressure, and d is the shell thickness. Introducing dimensionless variables, we get

$$\frac{b}{g} \approx \frac{\Delta p}{p}\frac{\varpi}{M_2}. \tag{4.39}$$

Taking into account that $\Delta p/p < 1$, it turns out that relatively large frequencies $\varpi >> M_2$ are required to produce values of b/g cosiderably larger than unity. The only way to put together the opposite requirements of equations (4.37) and (4.39) is to use the lowest possible frequency that allows us to enter the stability region.

It is necessary to take into account the conditions for κ_m derived fom the compressibility

effects in the stability charts, in order to obtain a more realistic representation of the stability regions. This can be done by simply introducing the expression (4.37) into the negative branch of equation (4.27) for each chosen value of the Mach number M_2. In fig. (4.9) a stabilty chart including compressibility for a typical reference case ($\kappa_c = 0.3$) is shown. One can see that in general, if the Mach number of the dense shell is known, a unique value of the minimum wave number that can be stabilized is determined, as well as the value of b/g and the oscillation frequency that must be used. Here we have chosen some possible values of interest for M_2, that is, $0.04, 0.06.0.10$ and 0.20, then for each value we have calculated the corresponding κ_m ,thus modifying the curves of the lower boundary with respect to the previous graphs, and finally we have taken the most restrictive upper boundary between the "old" boundary and the curve $\Delta p/p = 1$. It is evident that for a sufficiently small Mach number, equation (4.39) does not impose any new constraint on the upper boundary. Moreover, the minimum value of κ_m is rather insensitive to the exact value of M_2 but, instead, it considerably affects the required values of b/g and ϖ.

4.2.3 The case of asymmetric Dirac deltas driving (AD)

So far the simplest case, namely the one of a sequence of symmetric Dirac deltas, has been analyzed to study the effect of the driving modulation on the RTI in the ablation front. However, there are several types of driving modulations including sequences of Dirac deltas and square waves which could be used as well, and that lead to analytical or at least numerically tractable solutions of the equation 4.16. A comparison between these solutions allows us to study the optimization of dynamic stabilization, that is, to determine the best shape of the driving modulation on the basis of the results obtained in terms of the new minimum wave number above which we achieve stabilization and of the new instability growth rate in the region of the parametric instabilities. Therefore the previous analysis has been extended to the other cases, and in this thesis the most significant results will be exposed.

To complete the analysis about driving modulations in the shape of sequences of Dirac deltas, now we will consider an asymmetric driving; the simplest case is the one of a sequence of negative (subtracting from the direction of backgorund gravity) Dirac deltas. Such a kind of modulation results from (4.10) by setting $\beta_1 = -\beta$ and $\beta_2 = 0$. As for the symmetric case, equation (4.16) must be solved when $\Gamma(\tau) = 0$, taking into

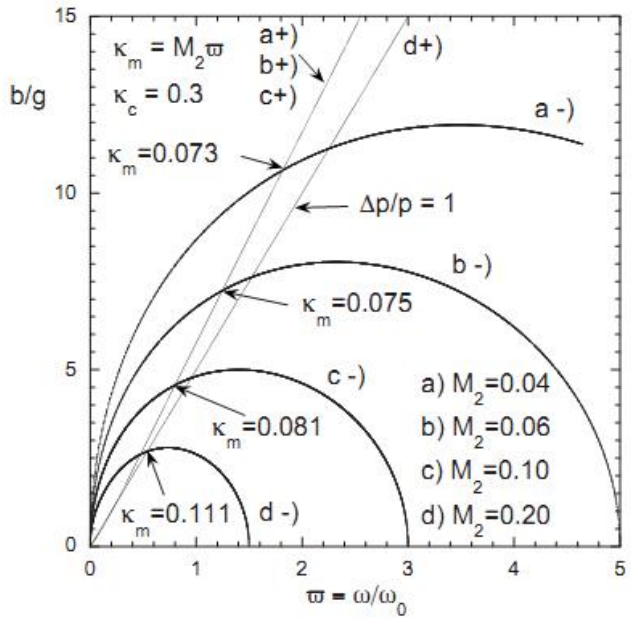

Figure 4.9: Stability chart for SD with compressibility (4) - Stability region for $\kappa_c = 0.3$. The lower boundaries ("-") are given for $\kappa_m = M_2\varpi$ and $M_2 = 0.04, 0.06, 0.10, 0.20$.. The upper boundaries ("+") correspond to the incompressible case of fig. 4.4 for the smallest values of M_2 and to a pressure modulation of $100\%(\Delta p/p = 1)$ for the case $M_2 = 0.20$. (source: Piriz et al, 2011 (35)).

account the conditions imposed by Floquet's theorem; in practice we introduce once again the general solutions (4.20) and (4.21), and impose the boundary conditions:

1. $y_1(0) = y_2(0)$;
2. $y_2(\pi) = y_3(\pi) = e^{i2\pi\nu} y_1(-\pi)$;
3. $\dot{y_1}(0) - \dot{y_2}(0) = -\beta_1 y_1(0)$;
4. $\dot{y_2}(0) - \dot{y_3}(0) = \beta_2 y_2(\pi) = 0$,

which yield the following conditions for the integration constants c_i:

1. $c_1 = c_3$;
2. $c_3 \cos\lambda\pi + c_4 \sin\lambda\pi = e^{i2\pi\nu}(c_1 \cos\lambda\pi - c_2 \sin\lambda\pi)$;
3. $c_2 = -\frac{\beta_1}{\lambda} c_3 + c_4$;
4. $-c_3\lambda \sin\lambda\pi + c_4\lambda \sin\lambda\pi - e^{i2\pi\nu}\pi(c_1 \sin\lambda\pi + c_2 \cos\lambda\pi) = 0$.

Solving this system of equations and performing some straighforward algebra, we get the following dispersion relation:

$$\beta = \sqrt{K^2 - D^2}\frac{\cos 2\pi\sqrt{K^2 - D^2} - \cos 2\pi\eta}{\sin 2\pi\sqrt{K^2 - D^2}} \tag{4.40}$$

Remembering the condition (4.26) and introducing the dimensionless variables already defined in (4.11), the dispersion relation becomes

$$\frac{b}{g} = 4\varpi\sqrt{1 - \frac{K^2}{D^2}}\frac{\cosh 2\pi D\sqrt{1 - K^2/D^2} \pm \cosh 2\pi(\sigma + D)}{\sinh 2\pi D\sqrt{1 - K^2/D^2}} \tag{4.41}$$

$$D = \frac{2\kappa}{\varpi},\ \frac{K^2}{D^2} = \frac{(\kappa/\kappa_c)^{2/3} - 1}{4\kappa}. \tag{4.42}$$

As in the case of symmetric Dirac deltas, the limits of marginal stability are given by the solutions of equation (4.41 when $\sigma = 0$. In fig. 4.10 these limits are represented for the same particular cases already chosen in the previous case, that is for $\kappa_c = 0.3, \varpi = 0.8$ and $\kappa_c = 1, \varpi = 0.5$. There are some differences in the limits with respect to the symmetric case.

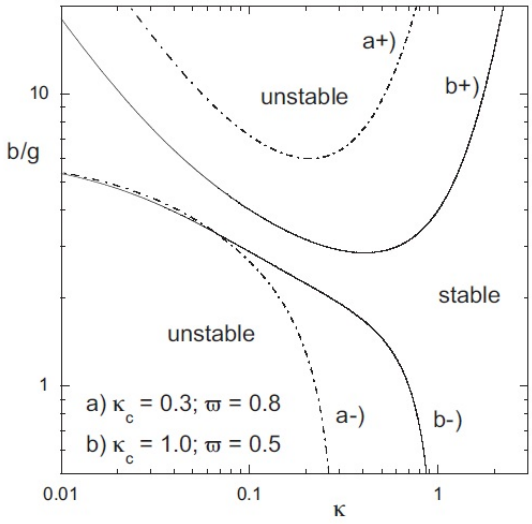

Figure 4.10: Stability region for AD (1) - Dimensionless driving acceleration b/g for marginal stability as a function of the dimensionless wave number κ for $\kappa_c = 0.3, \varpi = 0.8$ and $\kappa_c = 1, \varpi = 0.5$, in the case of an asymmetric Dirac delta modulation (source: Piriz et al, 2011 (35)).

In the limit for $\beta \to 0$ ($\kappa << 1$) of the (4.40), we have that $D^2/K^2 \to 0$ and we can use the Taylor developments for the sine and the cosine, thus getting:

$$\left.\frac{b}{g}\right)_+ \approx 2\frac{\varpi}{\sqrt{k}},\ (\kappa << 1). \tag{4.43}$$

which is the same as (4.32). To calculate the lower limit in the case $\kappa << 1$, we transform as before the sine and cosine into the corresponding hyperbolic functions and we use their Taylor developments, thus getting

$$\left.\frac{b}{g}\right)_- \to 2\pi\ (\kappa << 1). \tag{4.44}$$

In order to find the limit for $\beta \to \infty(\kappa >>)1$ of (4.40) for both the upper and lower limit , we perform again the usual tranformations of trigonometric functions into the corresponding hyperbolic ones and use the exponential development for the hyperbolic sines and cosines; we have that

$$\left.\frac{b}{g}\right)_\pm \approx 4\varpi[1 \pm e^{(\pi/2\varpi)[(\kappa/\kappa_c)^{2/3}-1]}],\ (\kappa >> 1). \tag{4.45}$$

We can notice that both the upper and lower limits for the asymmetric driving grow exponentially in a somehow stronger way with respect to the symmetric case. These

differences cause the minimum value of the upper limit to be higher in the asymmetric case than in the symmetric case, whereas the lower limit for the asymmetric case seems to be restricted to the condition $b/g \leq 2\pi$). In principle this behaviour can be interpreted as the possibility of dinamically stabilizing all the perturbation wave numbers provided that the driving acceleration is large enough to set the upper limit of the region of stability above 2π. Actually, such an hypothesis does not take into account the effects of the compressibility, which cannot be neglected at all beacuse they are essential to produce valeus of $b/g > 1$. Therefore, in reality we can only stabilize values of the wavenumbers larger than κ_m,where the latter depends on the Mach number of the shell. As in the previous case, we draw the stability charts for the same two values of interest of the cut-off wave number as in figg.4.4-4.5 , namely $\kappa_c = 0.3, 0.1$ (figg.4.11-4.12), in order to make a direct comparison.

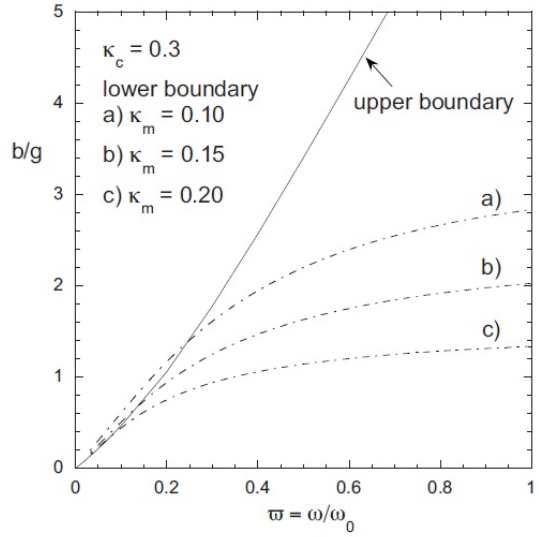

Figure 4.11: Stability chart for AD (1) - Stability region in the case of an asymmetric driving, for $\kappa_c = 0.3$. The lower boundary is given for $\kappa_m = 0.1, 0.15$ and 0.20. (source: Piriz et al, 2011 (35)).

It can be noticed that in the asymmetric case we can achieve a wider stability region with relatively lower values of ϖ and b/g. In particular, in fig. 4.11 it can be seen that, for $\kappa_c = 1$ and assuming that compressibility effects are not present, for $b/g \geq 2\pi$ all the wave numbers could be stabilized. Moreover, the dynamic cut-off wave number is reduced with respect to the symmetric case.

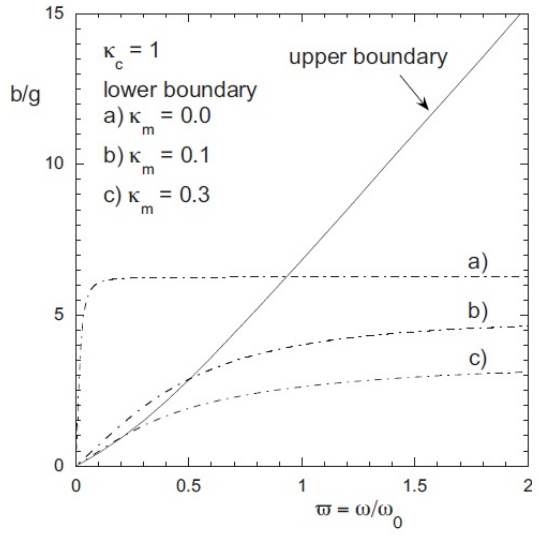

Figure 4.12: Stability chart for AD (2) - Stability region in the case of an asymmetric driving, for $\kappa_c = 1$. The lower boundary is given for $\kappa_m = 0.05, 0.1$ and 0.3. (source: Piriz et al, 2011 (35)).

To complete the comparison between the two cases we analyze the behaviour of the growth rate for different values of the dimensionless driving acceleration, for given values of κ_c and ϖ . The equation for the growth rate can be derived from the dispersion relation (4.41) by calculating $\sigma(\gamma v_2/g = \sigma\omega)$ a s a function of the other variables:

$$\sigma = \frac{1}{2\pi}\cosh^{-1}\left[\pm\left(\cosh 2\pi D\sqrt{K^2-D^2} + \frac{q}{\sqrt{1-K^2/D^2}}\sinh 2\pi D\sqrt{K^2-D^2}\right)\right] - D. \tag{4.46}$$

In figg.4.13-4.14 we can see respectively the graphs of the different growth rates for each value of b/g and of the corresponding regions of stability for the asymmetric case, for the same choice of the parameters as in figg.4.7-4.8 for the symmetric driving. A direct comparison shows that the asymmetry leads to a reduction of the growth rate. This advantage seems to be maintained even when we take into account the compressibility effects. The stability chart for asymmetric driving in the presence of compressibility effects is shown in fig. 4.15, for the same values of κ_c and of the Mach number as in fig. 4.9. The graphs show that in the asymmetric case it is possible to get lower values of the minimum wave number κ_m with relatively lower values of b/g and ϖ for each given value of M_2.

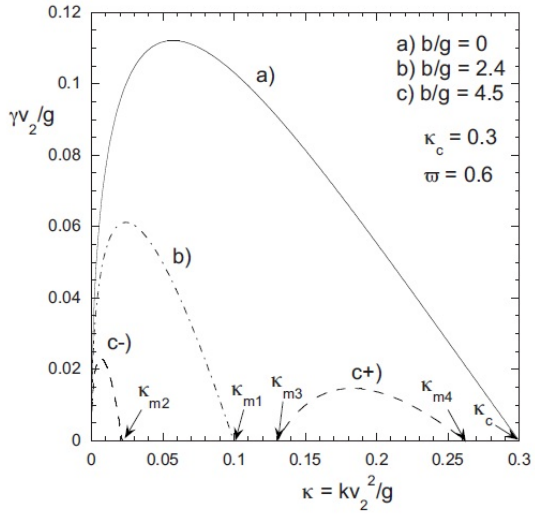

Figure 4.13: Instability growth rates for AD - Instability growth rate for $\kappa_c = 0.3$ and a fixed dimensionless frequency ϖ for different values of the dimensionless driving acceleration b/g, in the case of an asymmetric driving (source: Piriz et al, 2011 (35)).

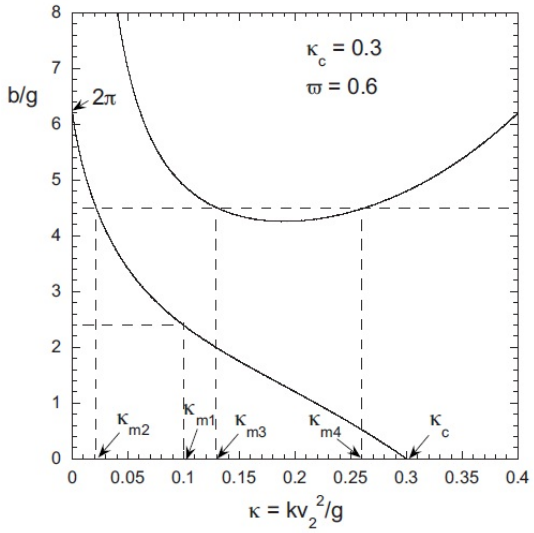

Figure 4.14: Stability region for AD (2) - Upper and lower limits given by dimensionless driving acceleration b/g from equation (4.27) as function of the dimensionless wave number κ for $\kappa_c = 0.3, \varpi = 0.6$, in the case of an asymmetric Dirac delta driving. The wave numbers $\kappa_{mi} (i = 1, 2, 3)$ correspond to the cut-off values of fig. (4.13). (source: Piriz et al, 2011 (35)).

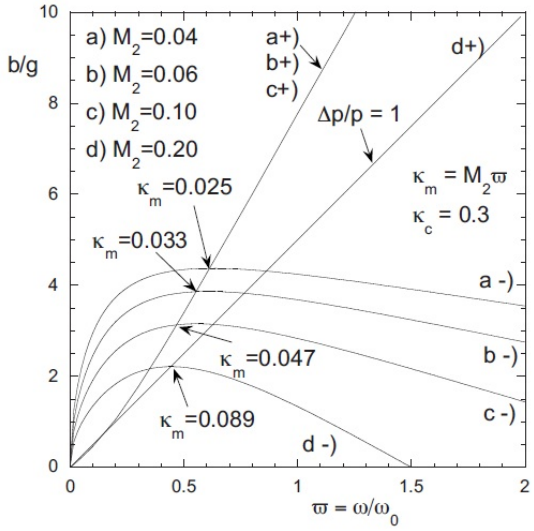

Figure 4.15: Stability chart for AD with compressibility (3) - Stability region for $\kappa_c = 0.3$ in the case of asymmetric driving. The lower boundaries ("-") are given for $\kappa_m = M_2\varpi$ and $M_2 = 0.04, 0.06, 0.10, 0.20$.. The upper boundaries ("+") correspond to the incompressible case of fig. 4.4 for the smallest values of M_2 and to a pressure modulation of $100\%(\Delta p/p = 1)$ for the case $M_2 = 0.20$. (source: Piriz et al, 2011 (35)).

Although the results for asymmetric driving are more satisfactory than the ones for the symmetric case, such an asymmetric driving consisting of negative Dirac deltas is not of practical interest by itself. In fact such an asymmetric modulation would lead to a continuous decompression of the shell region of thickness $\Delta y \approx c_{s2}\varpi$, thus causing a translation fo the unstable interface to the position $y \sim -k_m^{-1}$ instead of a stabilization. Actually, any type of driving should maintain the density average value ρ_2 of the dense layer ahead the front in such a way that at the end of each oscillation cycle, the interface should go back to its equilibrium position. This is not the case of a driving whose asymmetry is only in one direction with respect to the background gravity. Therefore, the study of a modulation of negative Dirac deltas can serve only as a basis for determining the results given by the following asymmetric modulation:

$$\Gamma(\tau) = \frac{1}{2\pi} - \delta(\tau). \tag{4.47}$$

Such a modulation represents a constant positive acceleration (adding to the background acceleration g) applied during all periods, followed by a negative pusle acceleration at the end of the period in such a way that the average acceleration is null.

Actually, it is a positive square wave plus a negative Dirac delta in the same period, in such a way that the total sum of the areas below the two pulses is zero. This way the average shell density is preserved. It can be verified that, by simply replacing g with $g' = g + b/2\pi$ the dispersion relation (4.41) is recovered. However, it is more useful to derive the treatment of this kind of modulation from the general formula for a sequence of square waves, as it will be shown in the next chapter.

5

Vibration waveform effect on dynamic stabilization of Rayleigh-Taylor instability in an ablation front

5.1 Introduction

In this chapter we will study dynamic stabilization of ablative RTI with a similar approach as in the previous one, but we will use as a driving modulation a more general waveform, in order to get some insight about the optimization process of the dynamic stabilization of RTI in an ablation front. This will allow us to state a general comparison between the performances of different waveforms in terms of the reduction of the natural cut-off wave number and of the maximum growth rate of the RTI.

5.2 Dynamic stabilization of Rayleigh Taylor instability in an ablation fronts by means of square waves.

In this section we consider a more general type of driving for the dynamic stabilization of ablative RTI consisting in a two-step or square wave modulation of the front acceleration which may better represent experimentally accessible drivings. This kind of waveform can still be treated analytically and allows for considering asymmetries in

the acceleration amplitudes and in the duration of each half-period. This is an advantage because, as we have seen in the previous chapter, a certain type of asymmetric driving (preserving the average shell density) seems to give better results for dynamic stabilization.

We start again from the equation (4.1) and in the Hill equation (4.9) we set

$$\beta\Gamma(\tau) = \begin{cases} +\beta_c & \text{if } 2m\pi \leq \tau \leq 2m\pi + c \\ -\beta_d & \text{if } 2m\pi + c \leq \tau \leq 2(m+1)\pi \end{cases}, \tag{5.1}$$

where $c + d = 2\pi$, K and D are the same as in (4.5)-(4.6) and

$$\beta_c = \frac{kb_c}{\omega^2};\ \beta_d = \frac{kb_d}{\omega^2}. \tag{5.2}$$

Moreover, the relation $b_c c = b_d d$ is valid so that the total sum of the area below the

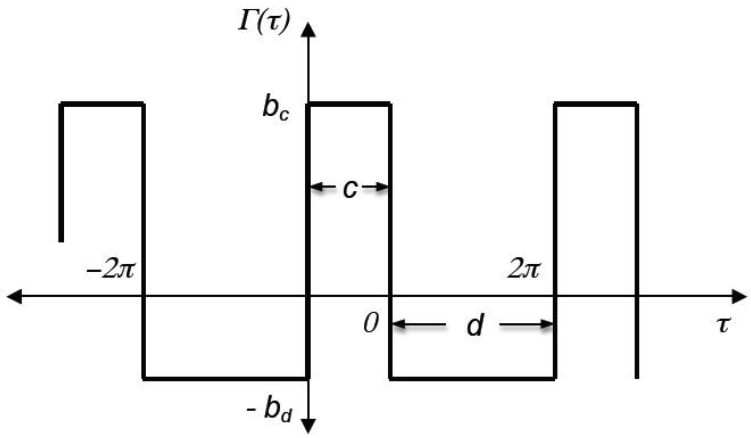

Figure 5.1: Square waves - General square wave oscillation.

square waves in a period is zero and the average acceleration of the front is $< G(t) >$=g (see fig. 5.1).

As in the case of Dirac deltas, we introduce the dimensionless variables (4.11) and solve the dimensionless Hill equation (4.16) in the regions where $\Gamma(\tau) = 0$ by adopting the general form (4.17 and using the consequences of the Floquet theorem (4.18)-(4.19).

For a general driving of the form (5.1) the solutions can be written as

$$y_1 = c_1 \cos \lambda_c \tau + c_2 \sin \lambda_c \tau, \tag{5.3}$$

$$y_2 = c_3 \cos \lambda_d \tau + c_4 \sin \lambda_d \tau, \tag{5.4}$$

$$y_3 = c_1' \cos \lambda_c \tau + c_2' \sin \lambda_c \tau. \tag{5.5}$$

$$\tag{5.6}$$

Here $\lambda_c^2 = D^2 - K^2 + \beta_c, \lambda_d^2 = D^2 - K^2 - \beta_d$.
Then we impose the matching conditions for the solution $y(t)$ and its derivative $\dot{y}(t)$ at $\tau = 2m\pi$ and $\tau = 2m\pi + c$, taking into account the properties of translational symmetry expressed in (4.18):

1. $y_1(0) = y_2(0)$;
2. $\dot{y_1}(0) = \dot{y_2}(0)$
3. $y_2(c) = y_3(c) = e^{i2\pi\nu} y_1(-d)$;
4. $\dot{y_2}(c) = \dot{y_3}(c) = e^{i2\pi\nu} \dot{y_1}(-d)$.

The corresponding equations for the integration constants are

1. $c_1 = c_3$;
2. $c_2 = \frac{c_4 \lambda_d}{\lambda_c}$;
3. $c_3 \cos \lambda_d c + c_4 \sin \lambda_d c = e^{i2\pi\nu}(c_1 \cos \lambda_c d - c_2 \sin \lambda_1 d)$;
4. $-c_3 \lambda_d \sin \lambda_d c + c_4 \lambda_d \cos \lambda_d c = e^{i2\pi\nu}(c_3 \lambda_c \sin \lambda_c d + c_2 \lambda_c \cos \lambda_c d$.

After some algebra, and taking into account the substitution (4.26) we get the following dispersion relation:

$$\cosh(\lambda_c c)\cosh(\lambda_d d) + \frac{\lambda_c^2 + \lambda_d^2}{2\lambda_c \lambda_d} \sinh(\lambda_c c)\sinh(\lambda_d d) = \cosh[2\pi(\sigma + D)]. \tag{5.7}$$

It can be noticed that this dispersion relation is the same as the resulting for the Schrodinger equation when the Kronig-Penney potential, consisting in rectangular sections, is considered, due to the mathematical analogies between the two problems. From equation (5.7) it is possible to extract an explicit expression for the dimensionless growth rate σ as a function of κ for given values of the front parameter κ_c and

of the modulation parameters b_d/g (or b_c/g) and ϖ, for any type of square wave (5.1) characterized by the parameters c and b_d (or b_c and d). In absence of modulation we have $b_c = b_d = 0$ and substituting these values into equation (5.7) one immediately recovers the growth rate for ablative RTI

$$\sigma = \sqrt{D^2 - K^2} - D. \tag{5.8}$$

As we have already seen that the relevant differencies for dynamic stabilization are between symmetric and asymmetric modulations, we will develop our analysis of the dispersion relation (5.7) for these two cases.

5.2.1 The case of a symmetric square waves driving

For a perfectly symmetric square wave (SSW) we have $c = d = \pi$ and $b_c = b_d \equiv b$. By substituting these values and putting $\sigma = 0$ in the equation (5.7) we get the expressions for the positive and negative branches determining the upper and lower limits of stability in the form of an implicit function b/g of the dimensionless wave number κ. Differently to the case of the sequence of Dirac deltas studied in the previous chapter, here both branches result to be multivalued functions of κ with infinite solutions. In particular for each values of the parameters κ_c, ϖ we obtain a graph in which the first curve from the bottom is the lowest solution of the negative branch, and then we see a set of infinite closed regions of stability limited by lobed curves as it is shown in fig. 5.2.These lobes determine the upper limit of the stability region: for each single case, this upper limit is given by the first lobe on the right of the lower limit, with respect to its position on the x-axis, that is above the lower curve in this region. Due to the implicit character of equation (5.7), the solutions must be found numerically by mean of a simple iteration process. Nevertheless, some limits useful for the discussion of the results can be obtained analytically.

For relatively large values of ϖ the upper limit, determined as described above, is given by the first lobe from the bottom (in red colour in the graphs (a) and (c) of fig.5.2). For this lowest lobe, we get the following asymptotic behaviour of the modulation amplitudes $\frac{b_c}{g}\Big)_+$ and $\frac{b_d}{g}\Big)_+$ for $\kappa << 1$:

$$\frac{b_d}{g}\Big)_+ = \frac{b_c}{g}\Big)_+ \frac{c}{d} \approx 2\sqrt{\frac{2}{cd^3}}\frac{\varpi^2}{\kappa}\left[\sqrt{1 + \frac{(d-c)^2}{2d^2c^3}} - \frac{d-c}{\sqrt{2d^2c^3}}\right] \quad (\kappa << 1). \tag{5.9}$$

For the rest of the higher lobes, we find that they also go as $1/\kappa$ for $\kappa << 1$:

$$\frac{b_d}{g}\Big)_{\pm} = \frac{b_c}{g}\Big)_{\pm}\frac{c}{d} \approx f_{\pm}(d/c, b_d/g)\frac{\varpi^2}{\kappa d} \quad (\kappa << 1), \tag{5.10}$$

where $f_{\pm}(d/c, b_d/g)$ is a multivalued function of b_d/g that for $\kappa << 1$ takes only discrete values. As the dimensionless frequency ϖ decreases, the number of lobes of the upper limit increases and they compact on an envelope curve which can be obtained from equation (5.7) by taking the limit $\varpi << 1$ (see graph (b) in fig.5.2)

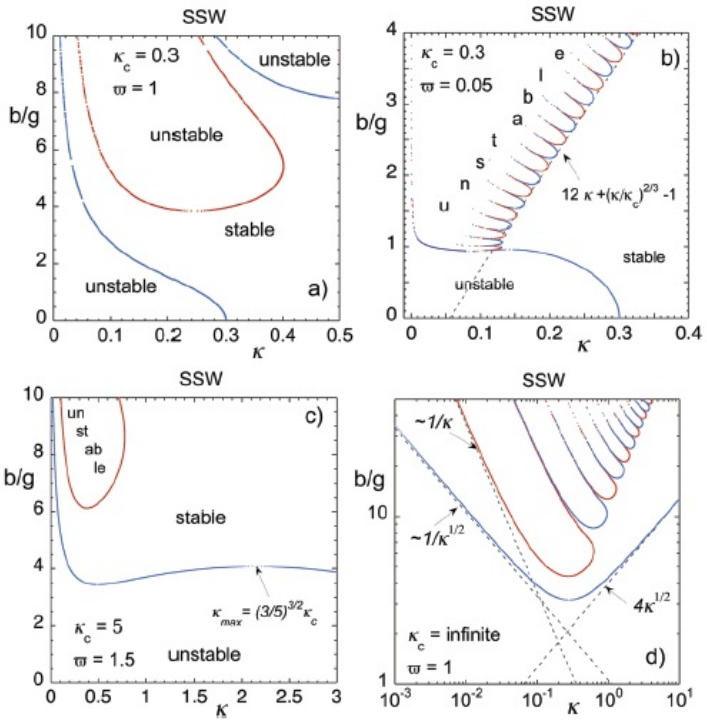

Figure 5.2: Stability region for SSW (1) - Dimensionless driving accelerations b/g for marginal stability as a function of the dimensionless wave number κ for a driving consisting of symmetric square waves and for: (a) $\kappa_c = 0.3$ and $\varpi = 1$; (b) $\kappa_c = 0.3$ and $\varpi = 0.05$; (c) $\kappa_c = 5$ and $\varpi = 1.5$; and (d) $\kappa_c = \infty$ and $\varpi = 1$. Red and blue curves correspond to the positive and negative branches of equation (5.7), respectively.

$$\frac{b_d}{g}\Big)_{\pm} = \frac{b_c}{g}\Big)_{\pm}\frac{c}{d} \approx \left[4\left[\frac{4\pi^2}{c^2} - 1\right)\kappa + \left(\frac{\kappa}{\kappa_c}\right)^{2/3} - 1\right]\frac{c}{d} \quad (\varpi << 1). \tag{5.11}$$

Unfortunately, this limit yields the rather unphysical result that perturbation wave numbers smaller than κ_c can still be stabilized when $\varpi << 1$ and this is due to the

assumptions of linear stability and incompressibility that underlie equation (4.1). In fact, in the dispersion relation (5.7) we have automatically considered stable all the periodic solutions with a bounded average value on a period even when, physically, the maximum amplitude would be large enough to make the instability enter in the non-linear regime. Such an information is not present in the model and this is the reason for the unphysical feature of the limit 5.11). From a practical point of view, this feature is irrelevant, because it will be shown later that actually this limit is never achieved when compressibility effects are included.

In the same manner as before, we can get the asymptotic behavior of the lower limit $b_d/g)_-$ [or $b_c/g)_-$] for small and large values of κ from equation . For $\kappa << 1$ we get:

$$\frac{b_d}{g}\Big)_- = \frac{b_c}{g}\Big)_- \frac{c}{d} \approx 2\pi\sqrt{2}cd^3\frac{\varpi}{\sqrt{\kappa}} \quad (\kappa << 1). \tag{5.12}$$

Instead, the limit for $\kappa << 1$ or $\kappa \to \kappa_c$ reads as

$$\frac{b_d}{g}\Big)_- = \frac{b_c}{g}\Big)_- \frac{c}{d} \approx 4\sqrt{\frac{\kappa[1-\kappa/\kappa_c]^{2/3}}{1+(\omega/2\pi\kappa)[(d/c-1)^2-1]}\frac{c}{d}}. \tag{5.13}$$

From (5.13) we find that there is a maximum for the lower limit for the largest values of κ, given by

$$\kappa_{\max} \approx \left(\frac{3}{5}\right)^{3/2}\kappa_c\left[1-\left(\frac{5}{3}\right)^{1/3}\frac{\varpi}{2\pi\kappa_c}\right]^3. \tag{5.14}$$

This maximum can be seen in graphs (b)-(c) of fig. 5.2 . Equation (5.13) yields an important result: for $\kappa_c \to \infty$ the lower limit goes to infinity for large values of κ (see graph (d) in fig.5.2) , that is, in absence of transport by thermal conduction dynamic stabilization results to be impossible since only a restricted range of wave numbers can be stabilized. This behavior is analogous to the one found for Newtonian fluids in absence of surface tension (21), but in contrast with the results previously obtained for Dirac deltas in section 4.2. Actually, the previous conclusions seem to derive from a mere artifact of the Dirac delta function and now we can say, more properly, that in general some minimum fraction of the energy flux driving the ablation process must be transported by thermal conduction in order to make dynamic stabilization possible. This point is of particular relevance for the ion beam driven ablation scenario recently considered by Logan et al. (36). For ablation directly driven by ion beams, most of the energy is transported by classical coulombian collisions, and thermal conduction may

be absent or just be a small fraction of the total energy flux. Nevertheless, numerical simulations show that around one third of the energy flux could be transported by thermal conduction, which, according to our analysis, would be sufficient for making possible dynamic stabilization of an ablation front directly driven by ion beams.
As in subsection 4.2.2, we take into account the compressibility effects by choosing a minimum stable wave number κ_m which is dependent on the dimensionless frequency for a given Mach number (see eq. 4.37). In this case we also have to consider the maximum of the lower limit: if $b(\kappa_m) < b(\kappa_{\max})$, the latter has to be assumed as the true minimum value of b/g required for stability. Once again, the upper boundary is the minimum of the higher curve corresponding to the lobe which is immediately above the lower limit and on the right of it with respect to the x axis. In an analogous way as for Dirac deltas driving, we construct the stability regions for b/g as a function of the dimensionless frequency ϖ , for a given value of the parameter κ_c and chosen values of the minimum wave number κ_m that we want to stabilize. In fig.5.3 we present two typical stability diagrams for $\kappa_c = 0.3$ and $\kappa_c = 5$, for the same values of κ_m: $0.1, 0.15$ and 0.20. In the case of $\kappa_c = 0.3$, the lower boundary is determined essentially by $b(\kappa_m)$, and for the largest values of κ_m (provided that $\kappa_m < \kappa_c$), we have the anomalous finite stability region for $\varpi << 1$ that we have previously discussed in the context of the "unphysical" limit for very small values of ϖ . When $\kappa_c = 5$ such a region is not present since the lower boundary is now fixed by $b(\kappa_{\max})$. It is important to notice that the general qualitative features of the stability regions for symmetric square waves are the same as for the sequence of Dirac deltas analyzed in section 4.2. In fact, also in this case we find that,the smaller the value κ_m of the minimum wave number that we want to stabilize, the larger are the dimensionless driving acceleration b/g and ϖ required for stabilization. However, with the introduction of compressibility effects, as shown in fig.5.4 some quantitative differences become evident.

It can be noticed that, as before, the condition (4.37) affects the lower boundary, whereas the (4.39) affects the values of the upper boundary only for Mach numbers that are larger than the ones considered in fig.5.4 and it may reduce the stability region if M_2 turns out to be too large. Once again, compressibility determines the minimum frequency ϖ and the minimum modulation amplitude b/g that are necessary for the stabilization for a given value of M_2. However, now the minimum value of the dimensionless wave number κ_m above which the perturbation wave numbers are

5. VIBRATION WAVEFORM EFFECT ON DYNAMIC STABILIZATION OF RAYLEIGH-TAYLOR INSTABILITY IN AN ABLATION FRONT

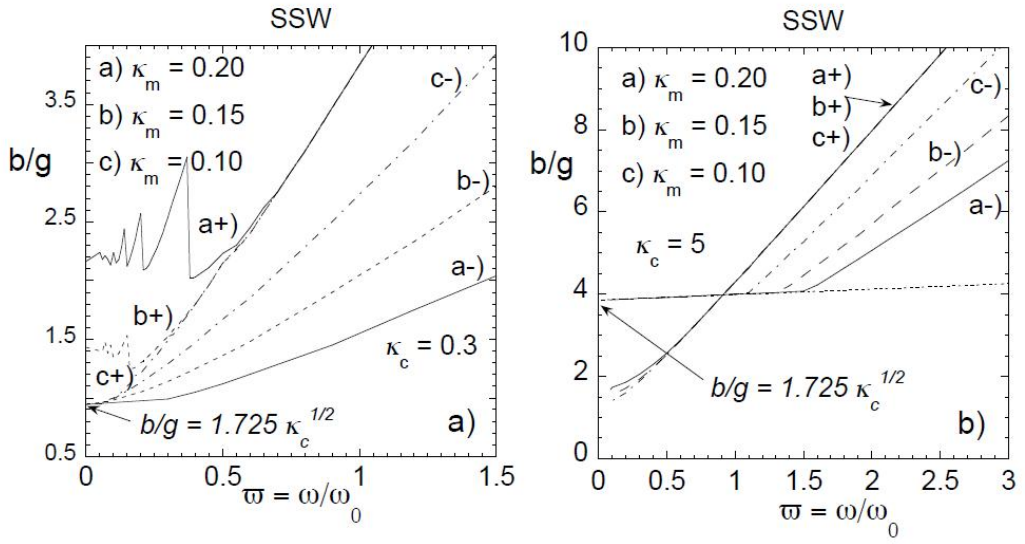

Figure 5.3: Stability region for SSW (2) - Stability region for $\kappa_c = 0.3$ and $\kappa_c = 5$ in the case of a symmetric square wave driving (SSW). In both cases the chosen values of minimum stable wave number are $\kappa_m = 0.10, 0.15.0.20$ (source: Piriz et al, 2011 (37)).

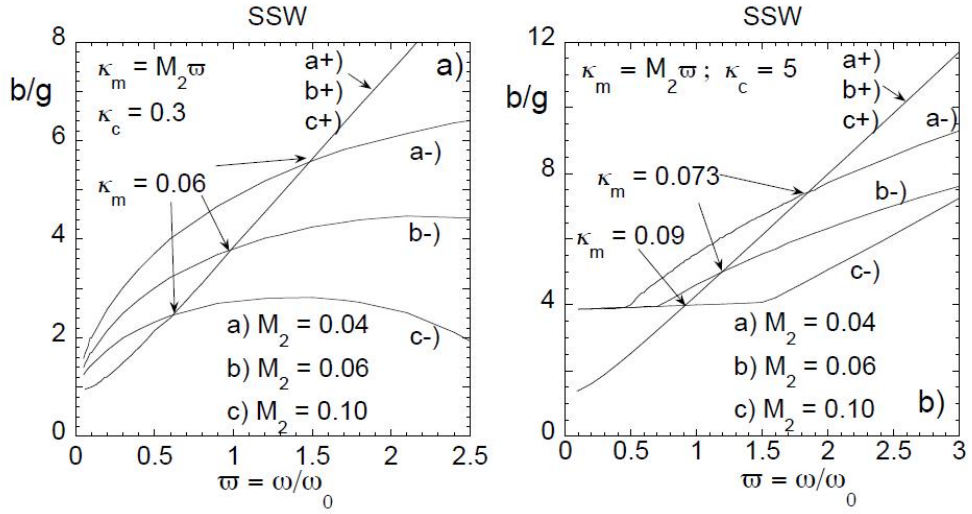

Figure 5.4: Stability chart for SSW with compressibility - Stability charts including compressibility in the case of SSW driving for $\kappa_c = 0.3$ and $\kappa_c = 5$. In both cases the boundaries are given for $\kappa_m = M_2\varpi$ and different values of the Mach number $M_2 = 0.04, 0.06$ and 0.10. s

stabilized results to be weakly dependent of M_2. Moreover, a quick comparison with the case of symmetric Dirac deltas (SD) shows some improvement in the reduction of the cutoff wave number: for SD we obtained $\kappa_m \approx 0.08$ starting from $\kappa_c = 0.3$, whereas with the same initial condition we are able to achieve a minimum stable wave number $\kappa_m \approx 0.06$. In order to complete our analysis of dynamic stabilization and to look for full optimization of the driving waveform, we examine the case of an asymmetric driving involving square waves.

5.2.2 Effects of asymmetries for square wave drivings

The advantages in the reduction of the growth rate with SSW with respect to SDD are not so large to make SSW decisely preferable. Therefore, it is interesting to see what could happen using asymmetric square waves.
Various possibility for an asymmetric square wave modulation have been considered, starting from the general form (5.1) and taking $c \neq d \neq \pi (c + d = \pi)$, provided that it is still valid the condition $b_d d = b_c c$, so that $< G(t) >= g$ and the average density of the shell material is preserved during the oscillation cycle.
It has been verified by performing practical calculations that asymmetries for which $c > d$ perform worse than the corresponding ones with $c < d$. In particular, the example discussed at the end of section 4.2.3 of a perturbation consisting of a positive square wave followed by a negative Dirac delta ($c = 2\pi, d = 0$) yields as its best result a reduction of the cut-off wave number $\kappa_m/\kappa_c = 0.67$ for $\kappa_c = 0.3$, which is a poor result if compared with the correspondent values of 0.25 and 0.2 obtained with SD and SSW, respectively, as it will be shown later when we will get a general view of the best performances for the different drivings. Therefore, here we will consider only situations in which $c < d$ and we will take the particular case $c = \pi/4 (d = 7\pi/4)$ as representative of the general situation. Fig. 5.5 shows the upper and lower limits of stability for the same values of κ_c used for the case of SSW. We can see that the qualitative features as the same as before, and in particular that if $\kappa_c = \infty$ dynamic stabilization is not possible (graph (d)), and that for $\varpi =<< 1$ stable solutions can be obtained (graph (b)).

In order to better appreciate the real performance of ASW, we directly consider the stability charts which include compressibility effects (fig.5.6). Again, we find that the lowest dynamic cut-off wavenumber is not strongly dependent on the values of M_2 and

5. VIBRATION WAVEFORM EFFECT ON DYNAMIC STABILIZATION OF RAYLEIGH-TAYLOR INSTABILITY IN AN ABLATION FRONT

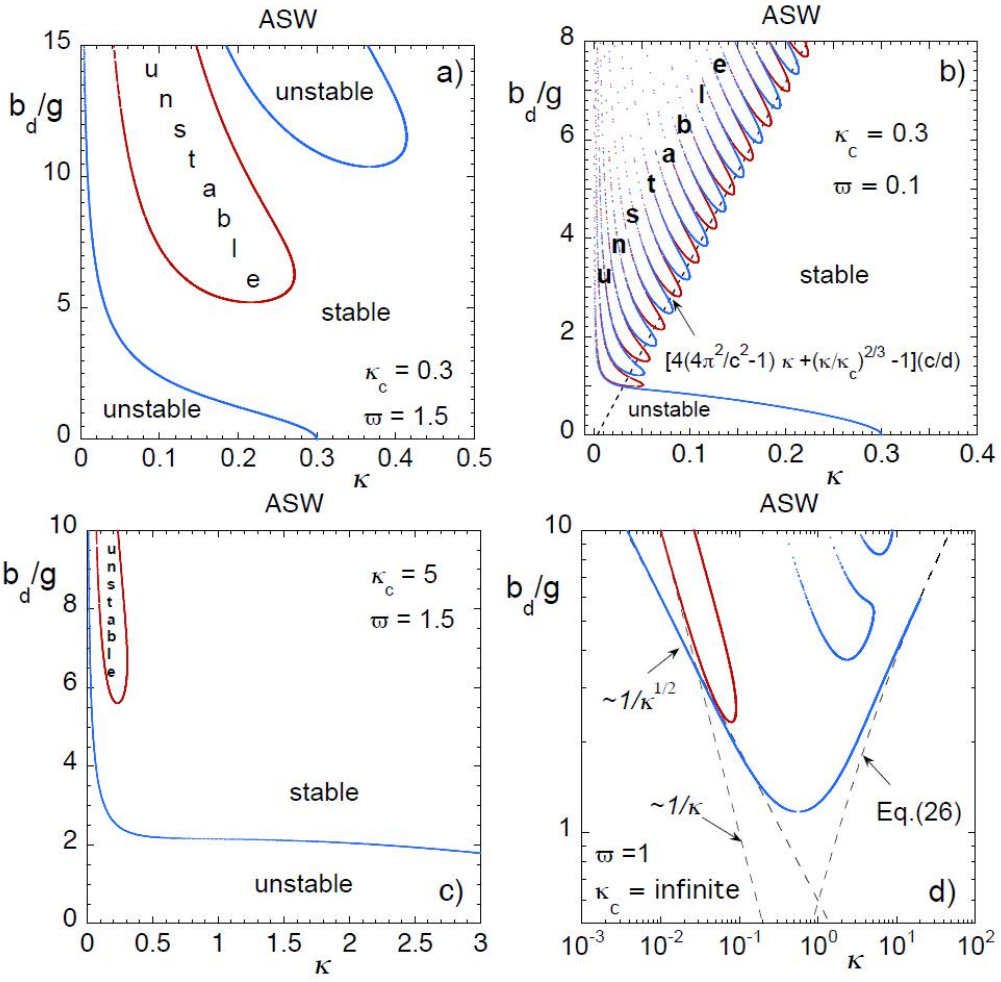

Figure 5.5: Stability region for ASW (1) - Dimensionless acceleration b/g for marginal stability as a function of the dimensionless wave number κ for an asymmetric square wave driving (ASW) and for : (a) $\kappa_c = 0.3$ and $\varpi = 1.5$; (b) $\kappa_c = 0.3$ and $\varpi = 0.1$; (c) $\kappa_c = 5$ and $\varpi = 1.5$; (d) $\kappa_c = 5$ and $\varpi = 1$. Red and blue curves correspond to the positive and negative branches of equation (5.7), respectively.

κ_c and has an approximately constant value $\kappa_m \approx 0.03$. This means that, although some minimum fraction ϕ_0 of the energy flux is required to be transported by thermal conduction in order to assure the possibility of dynamic stabilization, even if the latter is relatively small we have a significant reduction of the natural cut-off wave number. As in the previous cases, smaller values of κ_m are possible, provided that κ_c is smaller , but the smaller is κ_c the harder is to get a further reduction of the fraction κ_m/κ_c.

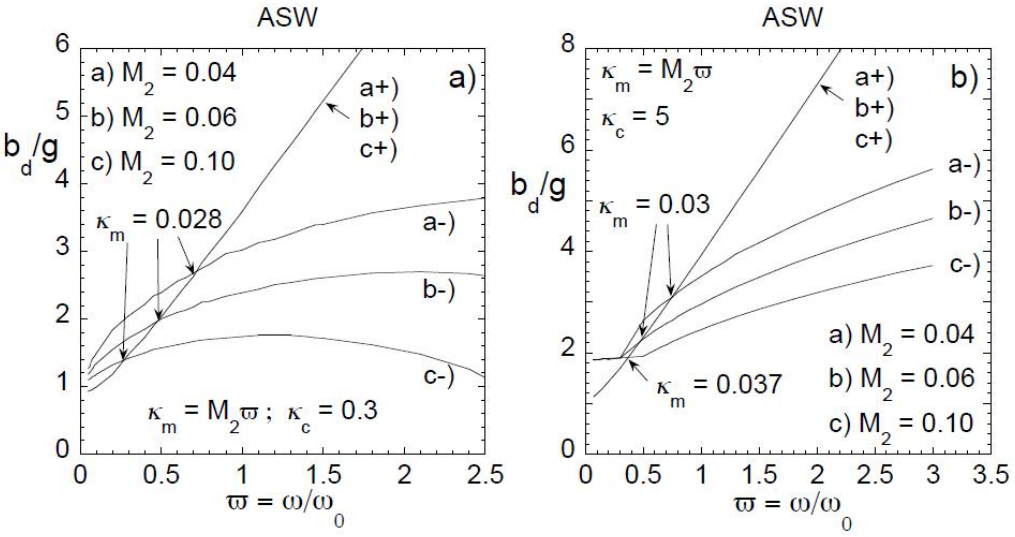

Figure 5.6: Stability chart for ASW with compressibility - Stability charts including compressibility in the case of ASW driving for (a) $\kappa_c = 0.3$ and (b) $\kappa_c = 5$. In both cases the boundaries are given for $\kappa_m = M_2\varpi$ and different values of the Mach number $M_2 = 0.04, 0.06$ and 0.10.s

By performing extensive calculations it has been found that the performance of dynamic stabilization of ASW improves (that is, κ_m is reduced) whn the duration of the positive half periods c is smaller. Therefore, we can get insight on the best performance that can be expcted from dynamic stabilization of an ablation front by considering the extreme case $c = 0$ ($b = 2\pi$) which results in a sequence of positive Dirac deltas followed by negative square waves in the same period.

5.2.3 The case of negative square waves + positive Dirac deltas (SW+D)

The dispersion relation for a sequence of negative square waves followed by positive Dirac deltas (SW+D) can be obtained from equation (5.7) by taking the limit $c \to 0$ and keeping $b_c c = \text{constant} = 2\pi b_d$:

$$\cosh 2\pi\lambda_d + \frac{\pi\beta_d}{\sinh 2\pi\lambda_d} = \mp \cosh[2\pi(\sigma + D)]. \tag{5.15}$$

As in the previous cases, by setting $\sigma = 0$ we get the boundaries of stability, which are represented in fig. 5.7 for the typical cases $\kappa_c = 0.3$ and $\kappa_c = 0\infty$. We can immediately notice that, although the general feautures are similar to the one sof SSW and ASW, the asymptotic behavior of the lower limit of stability for large values of κ is quite different.

In order to see the difference in a quantitative way, we calculate the limit of the lower curve for $\kappa >> 1$ or $\kappa \to \kappa_c$, and we get

$$\left.\frac{b_d}{g}\right)_- \approx \frac{2\varpi}{\pi}\left\{ e^{\frac{\pi}{2\varpi}\left[\frac{b_d}{g} - 1 + \left(\frac{\kappa}{\kappa_c}\right)^{2/3}\right]} - 1 \right\}. \tag{5.16}$$

Then, for any fintie value of κ_c, $b_d/g \to 0$ for $\kappa = \kappa_c$ without having any maximum as the ones observed for the general square waves. In addiction, for $\kappa_c \to \infty$, equation (5.16) shows that a minimum value $\left.\frac{b_d}{g}\right)_{\min}$ is reached. This means that if we involve Dirac deltas in the modulation, dynamic stabilization is possible even in absence of thermal conduction jst like wa have already found for the other Dirac delta drivings. This fact strenghtens our previous conclusion that in realistic situations dynamic stabilization of an ablation front requires that some fraction of the energy flux be transported by thermal conduction and results as the one in graph (c) of fig. 5.7 are only a mere artifact of using Dirac deltas.

The asymptotic behavior of the lower limit for $\kappa << 1$ reads as

$$\left.\frac{b_d}{g}\right)_- \approx \frac{\sqrt{3}}{\pi}\frac{\varpi}{\sqrt{\kappa}} \quad (\kappa << 1), \tag{5.17}$$

which means that for small values of κ it is $\left.\frac{b_d}{g}\right)_- \sim \frac{\varpi}{\sqrt{\kappa}}$, in general agreement with the results obtained for any other type of modulation, including the sinusoidal modulation used in the literature (38). From this we can conclude that the particular kind of modulation only affects the numerical factor of proportionality.

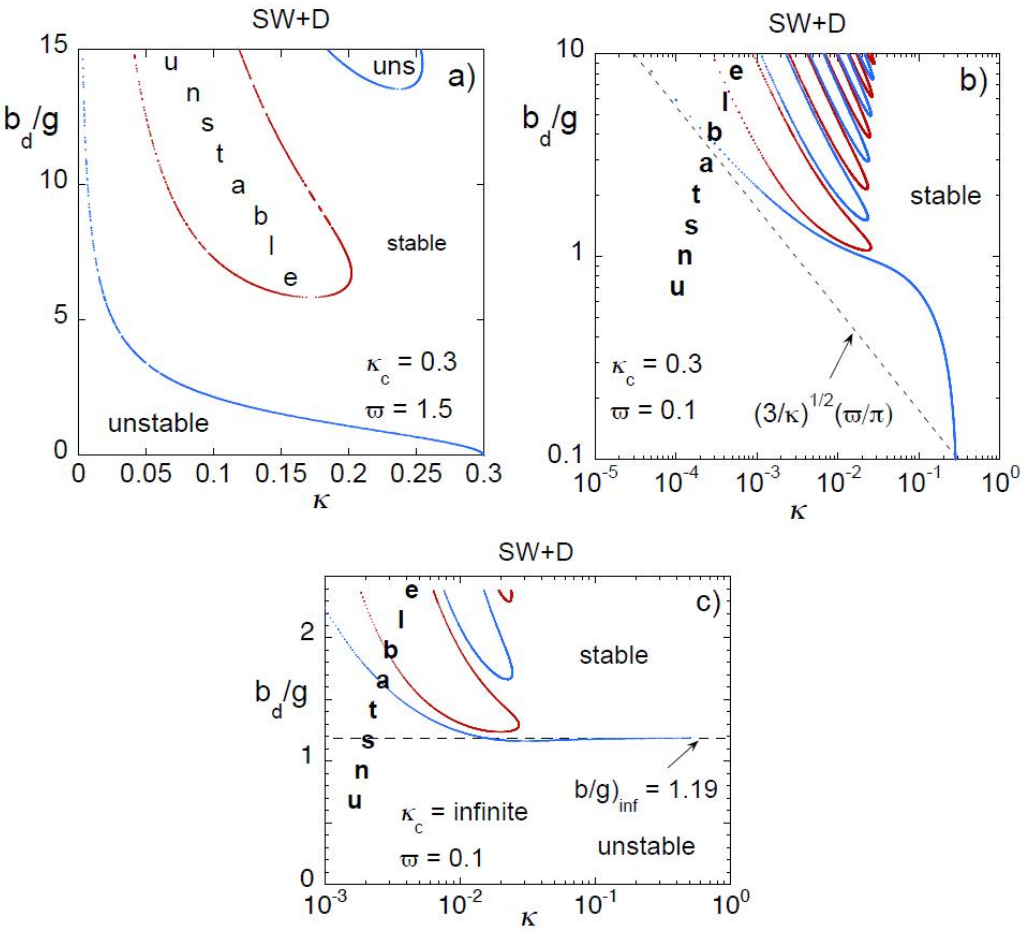

Figure 5.7: Stability region for SW+D - Dimensionless acceleration b/g for marginal stability as a function of the dimensionless wave number κ for a SW+D and for : (a) $\kappa_c = 0.3$ and $\varpi = 1.5$; (b) $\kappa_c = 0.3$ and $\varpi = 0.1$; (c) $\kappa_c = \infty$ and $\varpi = 0.1$. Red and blue curves corrspond to the positive and negative branches of equation (5.15), respectively (source: Piriz et al, 2011 (37)).

Fig.5.8 shows the stability charts for SW+D including already the compressibility effects. We can see that for $\kappa_c \geq 0.3$, it results $\kappa_m \approx 0.015$, which means a reduction of a factor larger than 20 ($\kappa_m/\kappa_c = 0.05$) in the cut-off wave number. Of course, as we have already discussed, such large reduction factors in the dynamic cut-off wave number are not held for progressively low values of κ_c since the resulting value of the dynamic wave number κ_m seems to be strongly dependent on κ_c . For instance, when $\kappa_c = 0.05$, we still get $\kappa_m \approx 0.015$ and the maximum reduction factor that can be obtained for the SW+D modulation is around 3 , which means $\kappa_m/\kappa_c = 0.3$.

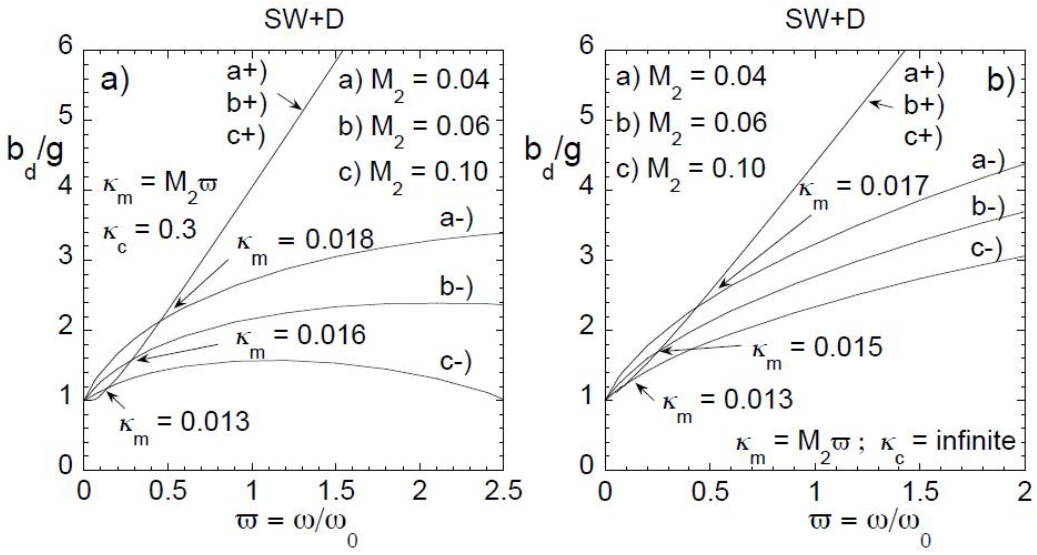

Figure 5.8: Stability chart for SW+D - Stability charts including compressibility in the case of SW+D driving for (a) $\kappa_c = 0.3$ and (b) $\kappa_c = \infty$. In both cases the boundaries are given for $\kappa_m = M_2\varpi$ and different values of the Mach number $M_2 = 0.04, 0.06$ and 0.10.

5.2.4 Growth rate comparison of different driving modulations

In order to get better insight into the differences between the performances obtained with different driving waveforms, we have calculated the best result for the instability growth rate that can be obtained in each case and compared them with the reference case when no modulation is applied. The results for the case of $\kappa_c = 0.3$ are shown in fig.5.9. If we look at curve (e) (SD) and curve (c) (SSW), we can notice that there is a 50% difference between the absolute values of the new minimum wave numbers

obtained with these two drivings, but if we compare this situation with any of the asymmetric cases the reduction of the cut-off is much more strong in the latter. In the same manner if we compare ASW (curve (b)) and SW+D (curve (a)) we notice a smaller difference with respect to a comparison with any of the symmetric curves . This means that there is a significant improvement in the performance if we substitute a symmetric driving with an asymmetric one. In particular, the best result is the one given by SW+D, which resembles the well-know picked-fence pulse proposed by Betti in (39),(40).

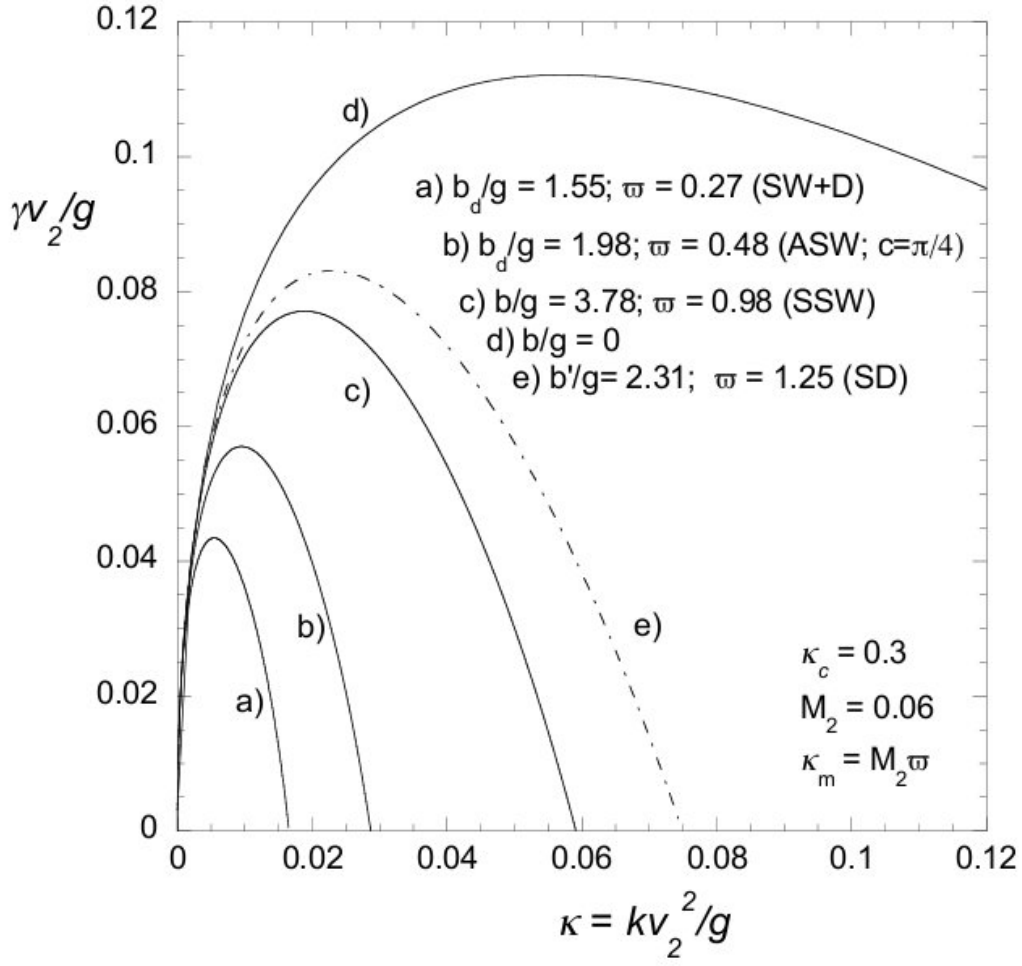

Figure 5.9: Comparison between different types of driving - Instability growth rates with respect to a case in which $\kappa_c = 0.3$ produced by using different types of driving: (a) negative square waves + positive Dirac deltas (SW+D); (b) asymmetric square waves (ASW with $c = \pi/4$); (c) symmetric square waves (SSW); (d) no driving ($b = 0$); and (e) symmetric deltas driving (SD)

6

Discussion and conclusions

In this thesis we have theoretically analyzed the problem of dynamic stabilization of RTI in an ablation front in inertial confinement fusion by means of a superposed periodical vertical vibration. For this purpose, we have first considered the simplest type of acceleration driving, which is the one consisting of sequences of Dirac deltas. Such an approach allows us to capture the essential physics of RTI in an ablation front by using a relatively simple mathematics; in fact it yields explicit analytical solutions for the instability dispersion relation which, in turn, leads to analytical expressions for both the instability growth rate and the boundaries of the region of marginal stability.

We demonstrate that, in general, as in the case of RTI in Newtonian fluids, the presence of damping effects is essential to dynamically stabilize all wave numbers above some minimum κ_m. However, when we use Dirac delta driving we get some stability region also in absence of a finite cut-off wave number in the RTI of the nonoscillating ablation front, that is, when there is no energy flux transported by thermal conduction. This behavior is different from the one observed in Newtonian fluids and it would be of special significance for the case of ablation fronts directly driven by ion beams where the energy transport is nearly completely due to collisional deposition, so that the natural cut-off wave number is very large. Nevertheless, it appears that such a result is a mere artifact of Dirac deltas since it was not retrieved when the study has been extended to other driving waveforms.

We have considered the constraints imposed on the stability region by the compressibility of the fluid layers ahead the front in a phenomenological manner. Such effects preclude the possibility of freely chosing the value of κ_m since it depends on the oscilla-

tion frequency ϖ through a factor of proportionality given by the shell Mach number. At the same time, the dimensionless driving acceleration is also related to ϖ in such a way that relatively large frequencies are necessary to generate large local values of b/g. Therefore, the best strategy is to use the minimum frequency required to reach the stability region and thus the minimum value of κ_m is determined.

In the context of Dirac deltas study, we have also examined the possibility of an asymmetric impulsive driving, and the related results have shown that the conclusions extracted from the symmetric impulsive driving also hold for the asymmetric case. Nonetheless, significant quantitative results are found, indicating that results can be improved by using an appropriate wave form for the acceleration modulation.

Asymmetric impulsive driving itself is not of practical interest for dynamic stabilization since it leads to a continuous decompression of the layer subjected to vibration. However, such results can be easily extended for calculating the growth rate of an equivalent problem in which the interface returns to its initial relative position at the end of each cycle, ensuring that the average value of the density of the vibrated layer is maintained. This modulation is given by a positive delta followed by a negative square wave in the same period. Later, we have found that actually such an option results in a worse performance than symmetric driving, but the comparison between the possible driving waveforms only became complete with the study of square waves.

Then, we have examined the case of a driving modulation consisting both of symmetric and asymmetric square waves. We have found that asymmetries consisting in a short duration and large positive acceleration followed by long duration and small negative acceleration perform better than the opposite case. The best performance corresponds to the limiting case when the positive acceleration is a Dirac delta. Such a kind of drivings resemble the picket fence pulses considered in the literature (39),(40) also for stabilization of RTI in an ablation front but based on a different principle. In fact, picked fence pulses have been proposed for controlling RTI in the ablation front by generating an entropy shaping that drives the layers beneath the front on a higher adiabat. In this way, an increase in the ablation velocity is produced that improves the front stability. Such effects, of course, are not included in our analysis of the dynamic stabilization but they could be certainly be present in a realistic situation providing a further mechanism of stabilization.

In addition, analysis of dynamic stabilization by means of square waves has proved that

in a realistic situation some minimum fraction of the energy flux that drives the ablation process must be transported by thermal conduction in order to make possible dynamic stabilization of the ablative RTI. Such a requirement could be of concern in the case of ablation directly driven by ion beams, for which beam energy is mainly trasported by Coulombian collisions. However, numerical simulations showed that some fraction $\phi_0 \simeq 0.3$ is transported by thermal conduction, making possible the dynamic stabilization of RTI also for ICF directly driven by ion beams (36). This means that dynamic stabilization in an ablation front behaves in a similar manner as for Newtonian fluids for which some minimum surface tension, besides of the viscosity, is required. These analogies suggest the possibility to use Newtonian fluids for surrogate experiments that may help to understand the physics of dynamic stabilization in a much simpler experimental framework.

Now we will extract from our analysis an example to illlustrate the design of an hypothetical experiment on dynamic stabilization. Using the typical scheme for the laser-driven pellet compression at NIF, we have the following values for the parameters:

1. laser wavelength: $\lambda_L = 0.35\mu$m
2. pulse duration: $\tau \simeq 4$ ns
3. radius of the capsule: $R \simeq 0.5$ mm
4. ablation velocity: $v_2 \simeq 10^6$ cm/s
5. background acceleration: $g \simeq 10^{16}$ cm/s^2
6. $I \simeq 9 \times 10^{14}$ W/cm^2.

. Typically, for a steady-state ablative corona, the ablation pressure is given by the following relationship (41):

$$p_2 \simeq 12Mbar(I/10^{14}\mathrm{W/cm^2})^{2/3}(1\mu\mathrm{m}/\lambda_L)^{2/3} \times (A/2Z)^{1/3}. \tag{6.1}$$

With the parameters above defined, equation (6.1) yields $p_2 \simeq 100$ Mbar.
In the context of the NIF scheme, ablation pressure by itself allows for stabilizing all the waveleghts $l \geq l_c = 150 = \kappa_c R$, therefore $k_c \simeq 3000$ cm^{-1} and from (4.11) we get $\kappa_c \simeq 0.3$. Then, assuming, for instance, $M_2 \simeq 0.15$, and if we want to reduce

$\kappa_c = 0.3$ to a minimum value $\kappa_m \leq 0.1$ by using a symmetric square wave, we can take $b/g = 3.5$ and $\varpi = 1$ in order to obtain a working point which is surely inside the region of stability (see fig.6.1).

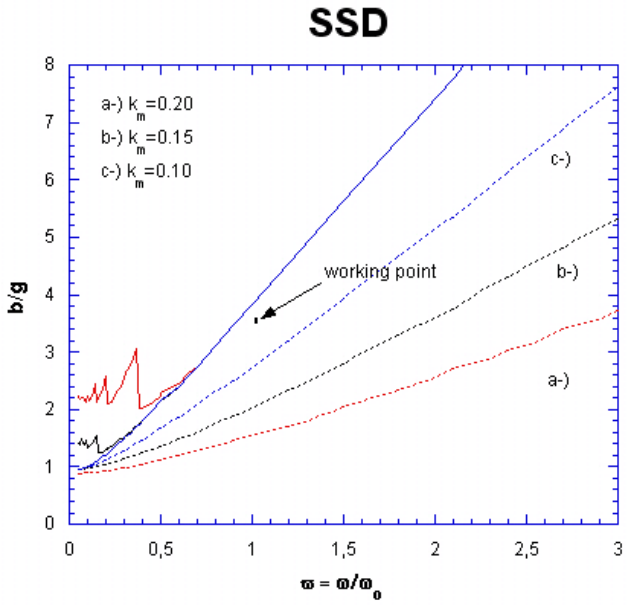

Figure 6.1: - Stability region for SSW driving and the working point chosen for our example: $b/g = 3.5$ and $\varpi = 1$.

On the other side, assuming that equation (4.39), valid for steady state conditions, can still be used for such rapid variations, we have:

$$\frac{\Delta p}{p_2} \simeq 0.5, \tag{6.2}$$

and remembering the (4.11) the frequency is given by

$$\nu = \frac{\varpi g}{2\pi v_2} = 1.6\,\text{GHz}. \tag{6.3}$$

Finally, from equation (6.1) we get

$$1 + \frac{\Delta p}{p_2} = \left(1 + \frac{\Delta I}{I}\right)^{2/3} \tag{6.4}$$

which yields $\Delta I/I = 0.84$. Therefore we need a driving oscillation of 1.6 GHz, with a 84% modulation in intensity.

In the previous example, we have used a phenomenological model for relating the pressure modulation to the required acceleration modulation b/g. Besides, we have assumed some reasonable values of the unknown Mahc number M_2. Furthermore, we have considered that the steady state model linking the laser intensity with the ablation pressure [equation (36)] is still valid for obtaining a relationship between the modulation in the ablation pressure $\Delta p/p$ and the laser intensity $\Delta I/I$. Certainly, a more rigorous approach is beyond the scope of this thesis and it would require numerical simulation in one and two dimensions. After a first step, one dimensional simulations would be necessary to set a precise relationship between the modulation intensity and the acceleration modulation as well as for determining the minimum wave number κ_m that can be stabilized. Finally, integrated 2D simulations would be required for the derailed design of an experiment. In those simulations the evolution of the RTI in the ablation front should be analyzed for one mode perturbations and for a given spectrum of mode perturbations resulting from the best surface finish allowed by the present technology.

It is clear that such a study can be performed by only a reduced group of researchers all around the world, possessing not only the adequate expertise but also the sophisticated tools consisting in the most powerful 1 and 2 D numerical simulations codes allowing for the above mentioned integrated simulations. However, the work presented in this thesis has settled the basis for such a study and will serve as a unique guide for them. Such numerical simulations would be impossible without a previous comprehension of the physical problem as the one we have afforded in this thesis.

Acknowledgements

This research project would not have been possible without the support of many people. The author wants to express her gratitude to her supervisor in Bologna, prof G. Turchetti, who suggested her the theme of research and the collaboration with prof. A. R. Piriz, and then allowed her to self-organize the work. The author's deepest gratitude goes to her supervisor in Spain, prof. A. R. Piriz, who teached her the basics of the physics underlying this research and developed the project with the strength of his innovative ideas. Special thanks to prof. G. Rodriguez Prieto, who provided the necessary guidance in the numerical work, and to the whole plasma physics group at University of Castilla-La Mancha, for useful discussion.

The author wishes to thank the complex systems group of the University of Bologna, and in particular Dr. C. Benedetti and prof. G. Servizi, for fruitful collaboration on the basis of numerics during the first year of PhD. This work, and in particular the travel expenses within the context of the cotutorship between the University of Bologna and the University of Castilla-La Mancha, have been funded by the Italian Ministry of Education and Research and by INFN, Bologna.

The author wishes to express her gratitude and love to her family, for their understanding and patience, through the duration of her studies.

References

[1] S. Glasstone, R.H. Lovberg, and United States Atomic Energy Commission. Office of Technical Information. *Controlled thermonuclear reactions: an introduction to theory and experiment*. Van Nostrand, 1960. 2

[2] S. Pfalzner. *An introduction to inertial confinement fusion*. Series in Plasma Physics. Springer, 2006. 4, 8, 31, 32, 33

[3] K.A. Brueckner and S. Jorna. **Laser-driven fusion**. *Reviews of modern physics*, **46**:325–367, 1974. 11

[4] G. Fraley. **Rayleigh–Taylor stability for a normal shock wave–density discontinuity interaction**. *Physics of Fluids*, **29**:376, 1986. 11

[5] S. Nakai and K. Mima. **Laser driven inertial fusion energy: present and prospective**. *Reports on Progress in Physics*, **67**:321, 2004. 12, 17, 18, 20

[6] J. Meyer-ter Vehn. **On Energy Gain of Fusion Targets: the Model of Kidder and Bodner Improved**. *Nuclear Fusion*, **22**:561, 1982. 19

[7] RE Kidder. **Energy gain of laser-compressed pellets-A simple model calculation**. *Nuclear Fusion*, **16**:405–408, 1976. 19

[8] M. Tabak, J. Hammer, M.E. Glinsky, W.L. Kruer, S.C. Wilks, J. Woodworth, E.M. Campbell, M.D. Perry, and R.J. Mason. **Ignition and high gain with ultrapowerful lasers**. *Physics of Plasmas*, **1**(5):1626–1634, 1994. 19

[9] C. Deutsch, H. Furukawa, K. Mima, M. Murakami, and K. Nishihara. **Interaction physics of the fast ignitor concept**. *Physical review letters*, **77**(12):2483–2486, 1996. 21

[10] C. Yamanaka. *Proc. 5th Int. Conf. Emerging Nuclear Energy Systems, ed. by UV Mollendorf and B. Goeld, World Scientific, Singapore, 125*, 1989. 24

[11] JM Soures, RL McCrory, CP Verdon, A. Babushkin, RE Bahr, TR Boehly, R. Boni, DK Bradley, DL Brown, RS Craxton, et al. **Direct-drive laser-fusion experiments with the OMEGA, 60-beam,¿ 40 kJ, ultraviolet laser system**. *Physics of Plasmas*, **3**:2108, 1996. 24

[12] R. Betti, CD Zhou, KS Anderson, LJ Perkins, W. Theobald, and AA Solodov. **Shock ignition of thermonuclear fuel with high areal density**. *Physical review letters*, **98**(15):155001, 2007. 27

[13] A. R. Piriz, J. Sanz, and L. F. Iba nez. **Rayleigh–Taylor instability of steady ablation fronts: The discontinuity model revisited**. *Physics of Plasmas*, **4**(4):1117–1126, 1997. 35, 53

[14] Lyman Spitzer Jr. *Physics of Fully Ionized Gases: Second Revised Edition*. Dover Publications, July 2006. 38

[15] HJ Kull. **Incompressible description of Rayleigh–Taylor instabilities in laser-ablated plasmas**. *Physics of Fluids B: Plasma Physics*, **1**:170, 1989. 38

[16] AW Trivelpiece and NA Krall. *Principles of plasma physics*. McGraw-Hill, 1973. 40

[17] SA Piriz, AR Piriz, and NA Tahir. **Rayleigh–Taylor instability in ion beam driven ablation fronts**. *Physics of Plasmas*, **16**:082706, 2009. 42, 47, 53, 55, 59, 60

[18] J. Nuckolls, L. Wood, A. Thiessen, and G. Zimmerman. **Laser compression of matter to super-high densities: thermonuclear (CTR) applications**. *Nature*, **239**:139–142, 1972. 45

[19] H. Takabe, K. Mima, L. Montierth, and RL Morse. **Self-consistent growth rate of the Rayleigh–Taylor instability in an ablatively accelerating plasma**. *Physics of Fluids*, **28**:3676, 1985. 46

[20] AR Piriz, OD Cortazar, J.J.L. Cela, and NA Tahir. **The Rayleigh-Taylor instability**. *American journal of physics*, **74**:1095, 2006. 47, 48, 51

[21] AR Piriz, G.R. Prieto, I.M. Díaz, J.J.L. Cela, and NA Tahir. **Dynamic stabilization of Rayleigh-Taylor instability in Newtonian fluids**. *Physical Review E*, **82**(2):026317, 2010. 47, 65, 66, 70, 73, 76, 94

[22] L.D Landau and E.M. Lifshitz. *Fluid mechanics*. Course of theoretical physics. Butterworth-Heinemann, 1987. 51, 53

[23] S.E. Bodner. **Rayleigh-Taylor instability and laser-pellet fusion**. *Physical Review Letters*, **33**(13):761–764, 1974. 55

[24] L. Baker. **Stability of ablation and combustion fronts**. *Physics of Fluids*, **21**:295–297, 1978. 55

[25] L. Baker. **Analytic theory of ablation layer instability**. *Physics of Fluids*, **26**:627, 1983. 55

[26] A. Stephenson. **On induced stability**. *Phil. Mag*, **15**:233–236, 1908. 63

[27] PL Kapitza. **Dynamic stability of a pendulum with an oscillating point of suspension**. *J. Exp. Theor. Phys*, **21**:588–597, 1951. 64

[28] RF Wuerker, H. Shelton, and RV Langmuir. **Electrodynamic containment of charged particles**. *Journal of Applied Physics*, **30**(3):342–349, 1959. 64

[29] G. H. Wolf. **The dynamic stabilization of the Rayleigh-Taylor instability and the corresponding dynamic equilibrium**. *Zeitschrift fr Physik A Hadrons and Nuclei*, **227**:291–300, 1969. 10.1007/BF01397662. 64

[30] F. Troyon and R. Gruber. **Theory of the Dynamic Stabilization of the Rayleigh-Taylor Instability**. *Physics of Fluids*, **14**:2069, 1971. 64

REFERENCES

[31] JP Boris. **Dynamic stabilization of the imploding shell Rayleigh–Taylor instability**. *Comments on Plasma Physics and Controlled Fusion*, **3**(1):1–13, 1977. 65, 70, 76

[32] R. Betti, RL McCrory, and CP Verdon. **Stability analysis of unsteady ablation fronts**. *Physical review letters*, **71**(19):3131–3134, 1993. 65, 78

[33] W. Magnus and S. Winkler. *Hill's equation*. Dover Pubns, 2004. 68

[34] R. Betti, VN Goncharov, RL McCrory, and CP Verdon. **Growth rates of the ablative Rayleigh–Taylor instability in inertial confinement fusion**. *Physics of Plasmas*, **5**:1446, 1998. 76

[35] AR Piriz, L. Di Lucchio, and G.R. Prieto. **Dynamic stabilization of Rayleigh–Taylor instability in an ablation front**. *Physics of Plasmas*, **18**:012702, 2011. 80, 82, 83, 84, 85, 86

[36] B.G. Logan, LJ Perkins, and JJ Barnard. **Direct drive heavy-ion-beam inertial fusion at high coupling efficiency**. *Physics of Plasmas*, **15**:072701, 2008. 94, 107, 109

[37] AR Piriz, L. Di Lucchio, G.R. Prieto, and NA Tahir. **Vibration waveform effects on dynamic stabilization of ablative Rayleigh-Taylor instability**. *Physics of Plasmas*, **18**:082705, 2011. 96, 101

[38] G.H. Wolf. **The dynamic stabilization of the Rayleigh-Taylor instability and the corresponding dynamic equilibrium**. *Zeitschrift f ”ur Physik A Hadrons and Nuclei*, **227**(3):291–300, 1969. 100

[39] TJB Collins, JP Knauer, R. Betti, TR Boehly, JA Delettrez, VN Goncharov, DD Meyerhofer, PW McKenty, S. Skupsky, and RPJ Town. **Reduction of the ablative Rayleigh–Taylor growth rate with Gaussian picket pulses**. *Physics of Plasmas*, **11**:1569, 2004. 103, 106

[40] R. Betti, K. Anderson, J. Knauer, TJB Collins, RL McCrory, PW McKenty, and S. Skupsky. **Theory of laser-induced adiabat shaping in inertial fusion implosions: The relaxation method**. *Physics of plasmas*, **12**:042703, 2005. 103, 106

[41] R. Fabbro, C. Max, and E. Fabre. **Planar laser-driven ablation: Effect of inhibited electron thermal conduction**. *Physics of Fluids*, **28**:1463, 1985. 107